Evaluation of a Large Eddy Simulation's Applicability to a "Worst Case" Fire Scenario

By

Jacqueline Lynné Du Bois

B.S.E. (Princeton University) 1994

A project submitted in partial satisfaction of the

requirements for the degree of

Master of Science, Plan II
In

Engineering-Mechanical Engineering

In the

GRADUATE DIVISION

Of the

UNIVERSITY OF CALIFORNIA, BERKELEY

Research Advisor:

Professor Carlos Fernández-Pello

Fall 1999

ABSTRACT

The applicability of a large eddy simulation to a small scale turbulent flow problem is assessed by comparing modeled results to those recovered from a physical apparatus with the same geometry. The computational domain is that of a rearward facing step with a channel-width to step aspect ratio of 2:1. The code utilized is LES-3d, and focus is placed on measuring the discrepancy between the recovered recirculation zone lengths when initial and boundary conditions of the virtual flow and duct are altered. It is found that the modeled results exceed the experimental by a factor of 2. These preliminary results point to the degree to which the user-specified parameters of upstream boundary conditions, inlet length, flow speed, flow profile, and computational domain resolution characterize and affect the simulated flow behavior. LES-3d's treatment of these crucial parameters is tested by performing additional experiments in a constant cross section straight duct with the same dimensions as the inlet to the previously mentioned rearward facing step. After looking into LES-3d's set of assumptions and means of incorporating the user's simulation preferences, a second set of simulations are executed with what are considered the optimal settings to guarantee the greatest degree of convergence between the experimental and modeled results. Findings indicate almost a 25% improvement in the recirculation zone measurements; however, other flow parameters such as the profile and boundary layer thickness are not maintained.

This report serves as the computational portion of an ongoing study aimed at engineering a bench-scale apparatus to test the effectiveness of non-halogenated fire suppression agents in aircraft engines. The work is performed in cooperation with the

National Institute of Standards and Technology, Gaithersburg, MD and the University of Maryland, College Park, MD.

ACKNOWLEDGEMENTS

This work has demonstrated to me beyond any reasonable doubt that a person can not exist in a vacuum if her intent is to do anything of any importance to anyone -- including herself. A great many people have assisted me with this project and for that I am truly grateful. Initially, I would like to thank Professor Carlos Fernández-Pello for his support especially during the few moments of uncertainty in which I contemplated turning my back on 6 years of advanced education in mechanical engineering and combustion science. I wish to thank him for putting me in contact with Professor José L. Torero and permitting me to write my thesis at the University of Maryland at College Park. To Dr. José Torero, I also owe a great deal of thanks, specifically for agreeing to supervise me. I am grateful for his provisioning a friendly working environment and for his gentle but relentless "encouragement" to understand the inner workings of my project. I would also like to thank department chairman Dr. Steven Spivak for welcoming me into the Fire Protection Engineering Department at the University of Maryland and for giving me a coffee mug to call my own.

This work was supported by the National Institute of Standards and Technology under grant No. 70NANB8H0043. I am thankful for the assistance of Dr. William Grosshandler, Michael Selepack, and Michelle Donnelly with experimental work I executed at the NIST headquarters in Gaithersburg, MD. I would also like to recognize Kevin McGrattan for his computer support with the LES-3d/IFS code and thank him for responding to my questions and offering valuable suggestions as to how to better apply the code to my application.

I thank Beverly Roberts for introducing me to wind tunnel project, the Maryland graduate routine, and the Fire Engineering and Thermal Sciences Laboratory (FETS lab). I am grateful to have had a partner on the project those first few months. I would like to acknowledge Grunde Jomaas', Alvaro Sifuentes', Yann and Benoit's contributions to the experimental piece of the project. I would like to thank the many other people that were, in various ways, involved in this project: Shivani, Noah, Alex, Sam, Phil, Thomas le bruin, Thomas le blond, my parents, my housemates, my friends, Ina, and H.P.

In addition, I would like to thank Cindy Gilbert, Sylvia Keane, Patricia Giddings, and Charity Oliver for the administrative work they performed to coordinate my joint tenure between the University of Maryland and the University of California. Lastly, I owe a great many thanks to Jeffrey Z. Manchester, the accountant at my previous place of employment, who more or less dared me to make the necessary calls to investigate whether I could complete my Master's degree at Berkeley while in residence in Virginia.

Thank you all for assisting me with this enormous project.

Evaluation of a Large Eddy Simulation's Applicability to a "Worst Case" Fire Scenario

By

Jacqueline Lynné Du Bois

B.S.E. (Princeton University) 1994

A project submitted in partial satisfaction of the

requirements for the degree of

Master of Science, Plan II
In

Engineering-Mechanical Engineering

In the

GRADUATE DIVISION

Of the

UNIVERSITY OF CALIFORNIA, BERKELEY

Research Advisor:

Professor Carlos Fernández-Pello

Fall 1999

TABLE OF CONTENTS

LIST OF FIGURES

CHAPTER 1

INTRODUCTION

Behind an enclosed duct with a rearward-facing step a recirculating flow is established. If a fire takes hold there, as is the case in the analogous geometry of aircraft engines, the probability is small that a suppression agent injected at the mouth of the duct would be sufficiently entrained into the reaction zone to alter the oxidation process and quench the flames. It is most likely that the agent would pass over the fire with the bulk of the flow. To date Halons, brominated chlorofluorocarbons, have been used to expeditiously extinguish fires in aircraft engines which have a geometry that can be reduced to that of a rearward-facing step. The bromide molecules that are entrained in the recirculation zone react with the free radicals released after ignition of the fuel source. This reaction inhibits the combustion, subsequently regenerates additional bromide atoms, thus propagating the fire suppressing reaction. However, the environmentally dangerous ozone depleting nature of this class of agents has required their phasing out. An international treaty, the Montreal Protocol, banned Halons 1 January, 1994 and has outlined a phase out schedule for them [1,2]. Production has had to decline drastically. As a result, it has become necessary to develop not only alternative fire suppression materials, but also a means of determining their effectiveness. The National Institute of Science and Technology (NIST) is currently working to establish such a protocol that will measure the effectiveness of alternative flame retardants' capacity to put out fires within the limited space of aircraft engines. The basic premise of their research is to institute the worst case scenario of a firmly anchored diffusion flame behind a rearward

facing step in a wind tunnel equipped with vessels that can be triggered to inject measured quantities of an agent into the air flow stream.

Flame suppression can be related to the Damkohler number $Da=\tau_{res}/\tau_{chemical}$. Fires with larger values of Da are more difficult to extinguish than those with smaller values. Therefore, flow past a rearward facing step should serve as a worst case scenario to study both the effectiveness of different suppression agents, and the critical flow patterns that govern flow entrainment in the reaction zone. Here, Da is maximized as a result of the long residence times of the circulating fluid trapped behind the step. If one can generate a numerical model that produces flow data that parallels fluid movement through an actual testing facility, simulations could yield valuable information. The computer generated results could illuminate characteristics for and the required trajectory of suppression agents in order that they interact with the reaction zone. Lastly, the information could be used to make improvements on the design of the testing facility without undergoing the costly process of trial-and-error structure modifications.

Before one can begin to assess reactive flow dynamics and extinction, an understanding of not only the hot but also the cold flow patterns established behind the step is essential. The literature features a broad spectrum of research on this particular geometry spanning a broad range of experimental and computational approaches.

LITERATURE REVIEW

Experimental Studies of the Backward Facing Step

The experimental dynamics of flow past a rearward-facing step has been studied extensively. From swept angle configurations [3] to vertical and 90 degree angle set ups [4], many have studied the structural features of the recirculation. Bradshaw and Wong's [5] pioneering work features a thorough assessment of flow dynamics behind a number of obstacles from steps to fences with a particular emphasis on the flow downstream of the rearward facing step. Experimenting with low speed two dimensional flows, their work looked into the complicated physical mechanisms that govern the slow non-monotonic return of the detached shear layer behind the step to its original boundary layer state downstream.

Shih and Ho [6] began to investigate when the aspect ratio of the flow channel was too small to justify analysis of the step flow as a two dimensional problem. They found that a 10:1 channel width to step height was sufficient to minimize the emphasis of three-dimensional effects. Employing laser doppler anemometry, they define the point of shear layer reattachment as the point where the surface velocity is zero. Reducing the aspect ratio, they found an asymmetrical zero-velocity spanwise profile develops behind the step. In essence, vortical structures shed at the step deform backwards and downwards at the centerplane of the apparatus redirecting vorticity into the transverse and streamwise directions [6].

Using a step configuration with low frequency downstream forcing, Browand [7] conducted experiments that illustrated that downstream of the step, an incompressible laminar flow gives rise to non-linear instabilities in the shear layer which multiply, transferring energy from a single frequency to a broad spectrum of frequencies. This is a clear sign of transition from laminar to turbulent flow conditions. He concluded that the

frequencies excited along with their harmonics were evidence of strong secondary instabilities within the separated shear layer.

Rohmat et al. [8] introduced a porous plate burner behind the step to study the behavior of turbulent diffusion flames anchored there. The authors were mainly interested in identifying experimental techniques to examine fluid and fire dynamics when turbulence is induced upstream. This work is innovative in so far as most experimentation with stabilized flames has focused on jet or spray diffusion flames behind baffles where laminar to turbulent transitions, flame length, lift, and extinction are studied. In replacing the fuel spray as the fuel delivery system, the spray port size is eliminated as a factor affecting turbulence observed in the channel. Using direct and Schlieren photography in conjunction with thermocouple probes, Rohmat et al. conclude that inducing turbulence at the step excites a greater degree of turbulence in the flow downstream compared to when it is induced upstream. In their data analysis, the authors are also able to show that turbulent energy is concentrated at low frequencies of the energy spectrum. Likewise, density differences between both the fuel and air at the plate burner and the flame heat release into the surrounding flow strongly contribute to the vortical structures that appear at the step.

Honji [4] investigated the initial transient dynamics of incompressible flow past a downstream-facing right-angled step. Focusing on the starting flow permitted him to draw out the fine structure of time-dependent recirculation behind the step for flows where the Reynolds numbers were less than 500. Within the initial range of $Re \leq 120$, he found a stationary recirculation is established, as Re increases to 140 and subsequently 200, secondary vortices appear immediately behind the step along with the main

recirculating bubble of fluid. Above 200, the secondary vortices are no longer stable and are convected downstream.

Tsou et al. [9] also looked at the starting dynamics of the flow structure and the heat transfer by studying an incompressible flow with Mach Number = 0.3 and Re = 38,000 based on the step height. Demonstrated experimentally with hot wire anemometry and heat flux gages, Tsou et al. measured an increase in the reattachment length at the initiation of the flow. At transition, a maximum value was observed. Finally, the characteristic length settled back to a steady-state value when turbulence was achieved approximately 10 ms into the experiment. Realizing a dearth of experimentation on transient heat transfer effects at start-up, the authors also investigated changes in heat flux across the recirculation zone into the free stream above the step. They did this by choking the flow downstream of the step and forcing an expansion wave through the inlet into the testing section. The effect was to cause the free stream temperature to drop approximately 16-18 °C below that of the wall. Temperature changes were miniscule indicating that the wall temperature was essentially constant. The heat flux patterns, however, demonstrated particular time-dependent profiles which clearly indicated the transition from laminar flow with a rapid increase in heat flux in the first 5ms, an abrupt jump in the value at transition, followed by a constant valued steady-state heat flux measurement as turbulence prevailed. This effect was observed in the free stream but not the recirculation zone

Westphal and Johnston [10] like Shih and Ho also focus their work on identifying the appropriate point of reattachment of a turbulent flow past a backward facing step when a number of different initial upstream conditions are implemented. They identify

the reattachment length as the point where the local skin friction along the floor of the channel downstream of the step averages zero. Perturbing the upstream conditions, they found that the reattachment length increases as the boundary layer thickness is increased. According to their results there is a moderate increase in reattachment length when the test section is angled below the inlet. Their configuration features a joint that permits the test section orientation to be altered relative to the inlet. Streamwise vortices added to the separating boundary layer caused the reattachment length to decrease. Using the recirculation length as a scaling parameter, Westphal and Johnston were able to collapse their coefficient of friction, turbulent velocity, mean velocity, and the coefficient of pressure data to the same curve, thus pointing to the recirculation zone length as a universal parameter of the system.

Armaly et al. [11], like those previously mentioned, focused on low speed flows past rearward facing steps with Reynolds numbers within the range of 70 to 8000. This was done to gain some insight on the alternative dynamics taking place when transition or turbulent flows (in contrast to laminar flows) were coincident at the inlet. These used a strongly two-dimensional channel duct configuration, choosing an aspect ratio of 36:1 with a ½ meter test section. They focused on the reattachment length as the flow parameter that would give the most information about how entrainment behind the step changes. Within the laminar regime, the characteristic reattachment length rises almost linearly with velocity. Through transition, the reattachment length decreases sharply at first and then drops gently. Finally, within the turbulent regime the recirculation length evens off in a plateau to attain a constant value. Armaly et al. complement this study with a grid-based numerical assessment that incorporates a finite-differencing scheme to

solve stationary mass and momentum equations incorporating nonslip boundary conditions. The software employed, called TEACH supplies initial guesses for the velocity and pressure fields and iterates to find a converged solution. The simulation could only be applied to the laminar regime where Re < 400 where it did correctly predict the recirculation details. The problem of not being able to specify enough computational points to resolve the highly turbulent areas behind the step arose at higher Reynolds numbers.

Computational Papers

Ghoniem and Sethian [12] also resorted to a computational means of studying the structure of the recirculating flow behind the step. The Reynolds numbers of the flows studied were 50, 125, 500, and 5000. They were looking into the predictive nature of a particular computational method called the random vortex method which incorporates a "random walk" routine to simulate diffusion. The computational algorithm used here is grid free and self-adaptive, automatically concentrating computational elements where large velocity gradients occur. "Random walk" excites the natural instabilities of the flow without inhibiting their growth. Analysis of the results shows that the recirculation length grows rapidly and then decreases hitting a plateau by Re=5000. Others already mentioned have showed these result trends. The authors show that the random vortex method has the additional capacity of quantifying the distinct eddy shedding patterns as the Reynolds number is altered. Earlier, such a computational method that could address

vortical multi-dimensionality did not exist. The code utilized was a modified version of MIMOC [13].

Instead of trying to match the recirculation lengths, Amano and Goel [14] focus primarily on reproducing the turbulent Reynolds stresses with their third order closure theoretical model of turbulence behind the rearward facing step. The authors point out that the additional physical structures introduced behind the step as a result of the separation of the shear layer require an in depth investigation and balancing of all the terms of the governing equations that may be contributing to the transfers and dissipation of energy. They focus specifically the third-order stresses. Reynolds stresses of the form $-\rho\overline{u_i u_k}$ appear when the instantaneous velocity terms and stresses are written as a convolution of a mean and fluctuating term, and the Navier-Stokes equations are then written in terms of the variable averages. The overbar here designates averaged turbulent velocity terms. This term is an expression of the viscous stresses acting in the fluid and it is comprised of two unknowns, the averaged velocities, which must be expressed as a function of the mean velocity in order to close the set of equations required for the problem. Solving the conservation equations for these convected quantities introduces additional third order terms of the form $\overline{u_i u_j u_k}$ which also need to be solved or matched against experimental data [15]. Shown previously, the second order closure model was found to be an improvement over algebraic schemes applied to the step [16]. With the third-order model, the results are good. The simulated Reynolds stresses, mean velocity, turbulent energy, dissipation rate and triple-velocity products agree with experiments. However, near the wall, the authors report that the method could be improved by

incorporating a routine that takes into account the more laminar viscous flow effects that are set up there [14].

Kwon and Pletcher's [17,18] numerical modeling scheme for the closed-channel backward facing step configuration assumes that the downstream flow domain can be broken up into a central inviscid region bounded by viscous regions along the duct ceiling and floor. This viscous-inviscid interaction procedure is intended to decrease the computational time associated with grid systems and to minimize the truncation errors that arise when higher order differential terms are suppressed (a result of finite-differencing). The entire domain is taken as two-dimensional. Kwon and Pletcher define the viscous region as incompressible and steady; the inviscid region as irrotational and incompressible. The continuity and momentum equations are solved in terms of the stream function at the upper and lower bounds of both viscous zones. The equations are solved inversely using velocity data from experiments to determine the pressure gradients across the domain. Two non-linear spatial functions based on the locally measured velocity are prescribed as the displacement surfaces along which velocities computed at either side should equal one another as the surface is approached. The displacement surface functions are iterated by a fraction of the local velocity and a relaxation factor until convergence is achieved. The authors found that the recovered coefficient of pressure distributions and velocity profiles agreed very well with experiments except in the region very close to the step. The turbulent shear stresses and kinetic energy were also over predicted there, but showed very good agreement with experimental results elsewhere.

Thangam and Speziale [19] review the frequently used K-ε model as applied to the backward facing step with the intent of pointing out misleading information in the literature pertaining to its use specifically those initial reports of the computational model underpredicting reattachment lengths by 25%[20]. K-ε is a grid based model and refers to a pair of equations solved across each unit of the grid overlying the turbulent eddy-seeded flows. The K-equation refers to the kinetic energy expression for the flow; the ε-equation is a mapping of the K equation into ε space by making use of the substitution

$$\nu_T = C_\mu \frac{K^2}{\varepsilon}$$

where ν_T is the turbulent kinematic viscosity and C_μ a constant determined either empirically or theoretically. ε essentially refers to the characteristic scale of the flow based on the presence of the eddies in the flow [21]. Upon compiling the results of their own assessment using a Re=13,200 flow based on the overall channel height, Thangam and Speziale [19] find that with appropriate resolution of the flow domain – essentially where grid independence is attained -- reattachment underprediction can be reduced to 12%. Across the domain, mean velocities, velocity profiles, turbulence intensity, and turbulent shear stresses are in good agreement with experimental results except in the vicinity of the reattachment point. Incorporating an anisotropic eddy viscosity improves agreement between the modeled and experimental recirculation length results to 3%. The improvement is due to the fact that the Reynolds stresses rarely share the same alignment and directionality as the large eddies present. The reattachment point predictions improve; however, the deviation between velocity profiles – specifically those in the

separation and reattachment regimes -- is slightly greater. However, if the re-normalization group (RNG) method is coordinated into the K-ε model, the reattachment lengths are underestimated by 57%. The RNG method is similar to the standard K-ε model except the constants are determined differently. The authors attribute this divergence from the experimental results as attributable to the fact that one of the constants of the flow studied takes on an inappropriate value which necessarily skews the results.

Le et al. [22] use direct numerical simulations (DNS) to model the passage of turbulent flow over a backward-facing step. This method solves the Navier-Stokes equations directly without employing correlations to model the viscosity terms. The step height based Reynolds number of the flow was 5100, the aspect ratio of their wind tunnel was 20:1. The reattachment length was measured within 3% of the experimental results; however, the peak negative skin friction coefficient recovered from the simulation took on a value three times greater than that measured experimentally. The authors point out that within the recovery region downstream of the reattachment point, low Reynolds number effects are poorly modeled with a DNS approach. Nonetheless, turbulent stresses measured throughout the region and the vortex shedding periodicity are properly expressed with this computational modeling routine.

Neto et al. [23] pursue the grid based large eddy simulation (LES) of as an alternative modeling scheme for two and three-dimensional conceptualizations of flow past a backward facing step. They incorporate the structure-function subgrid method to capture the smaller scales of motion that are damped out by the standard LES formulation. Typically, LES utilizes a spatial filtering function to define the governing

equations for the large-scale motions. The structure function subgrid model uses both a mixing length which is on the order of the mesh size and an averaged spectral eddy approach based on defining the kinetic energy of the turbulent flow as a spectrum of discrete energy quantum to come up with values for viscosity at the level of the grid cell. Contrary to many other computational fluid dynamicists, the authors do not model the inlet; rather they impose a velocity profile at the step. The results of their simulation depict the billowing vortex traces peculiar to experimental flows. The authors compare their results to a modified direct numerical simulation that incorporates a degree of viscous damping, the standard K-ε model, and large eddy simulations utilizing the subgrid Smagorinsky model for viscosity. The flows measure Reynolds numbers based on the step height of 6000 and 38,000. In these experiments the step height is varied. Comparing both their two- and three-dimensional simulations to experiments, the authors find that the structure-function model behaves much better than any of the other models and better resolve the oscillation and vortex shedding of the flow behind the steps of different sizes.

Ducros et al. [24] modify the structure-function of the afore mentioned research team and investigate the performance of a filtered structure-function for quasi-incompressible flows as the subgrid model for the large eddy simulation. This computational model looks at the spatially growing simulated flow from transition to turbulence as it passes over a flat plate. The authors indicate that the Smagorinsky and straight structure-function viscosity models can not make allowances for the spatial growth and hydraulic jump occurring in the flow. Although a step is not incorporated into the configuration, the shear layer structure has many turbulent vortical features

which appear in separated shear layer flows. The critical plate length dependent Reynolds numbers used here are 338,000 and 1,150,000; the Mach number is 0.5. The plate measures 812*δ in the streamwise direction where δ is the boundary layer thickness. The filtered structure-function utilizes a second-order structure-function to express the kinetic energy spectrum of the flow. The overall effect is to eliminate the large-scale oblique flow perturbations which have been identified as contributing to the original structure-function's overestimation of the eddy viscosity at start-up. Ducros et al. refer to their work as a preliminary study. Qualitatively, the results agree well with experiments; however, friction is underestimated due to the insufficient resolution of the grid used to model the problem.

Fureby and Moller [25] endeavor to simulate a reacting premixed laminar flow past a three dimensional triangular prism that spans a square duct. Their goal is to look into the predictive quality of the large eddy simulation. The authors perform two types of simulations, one with a built in subgrid modeler to resolve the smaller scales of the problem. The other LES simulation operates without the subgrid model: it is assumed that the truncation error of the differential equation solver acts as its own subgrid model of sorts. The challenge Fureby and Moller are taking on is not only that of simulating the combustion of a generic alkane, but also determining the interaction between energy releases resulting from chemical reactions and those incited by temperature, pressure, density, or turbulence gradients across the flow domain. They develop secondary subgrid models to describe the radiation, the combustion by-product mechanisms, and the thermo-chemical motion and apply them to both LES formulations. Comparing their results to experiments, the temperature, mass fraction, and velocity fields all compare

well to experiments. It is revealed that the truncation error is as effective as the formal subgrid modeler for addressing the small-scale energy dissipation effects.

Having found the large eddy simulation to agree well with their earlier experimental efforts [26], Kobayashi and Togashi [27] look not only to improve the simulation by incorporating a gradient diffusion model to address diffusion at the molecular levels of the flow but also to investigate the energy stresses introduced by turbulence. The diffusion gradient subgrid model improves the turbulent energy measurements of the initial LES simulation. The authors also compare K-ε, anisotropic K-ε, and algebraic stress models with the original LES conceptualization on identical grids. Respectively, the reattachment lengths identified for the models are 6.0 times the step height (H), 6.15 H, 6.45 H, and 7.10 H. The actual reattachment length was measured as 7.0 H. Of all the modeling routines investigated, Kobayashi and Togashi conclude that the velocity profiles and Reynolds stresses of the algebraic model compare well with the large eddy simulation eventhough it underpredicts the reattachment length. Likewise, they point out the weakness of the K-ε models to model the Reynolds stresses appropriately.

Only part of the problem is understanding physically what is taking place in the wind tunnel. With the most complete understanding of upstream, downstream, and transient dynamics one then considers incorporating theoretical schemes and numerical algorithms that will best describe these phenomenon. Modeling the parameters of interest, the hope is that the mechanism incorporated does not introduce errors that will ultimately devalue any results generated. The scope of literature referring to analyses of computational methods for the backward facing step detail grid free formulations such as

the random vortex method; and grid based computational methods including direct numerical simulation, large eddy simulations with and without subgrid models, K-ε, inviscid-viscous, and algebraic stress models. The performance of these primary modeling techniques has been well documented. The one area of the literature that appears sparse in comparison is that pertaining to the suppression of obstacle-stabilized flames with halogenated or other fire extinguishing agents. In addition, few documents available to the public review current innovations in and performance statistics of halogen replacements in real fire scenarios.

Papers Noting Reignition Dynamics and Innovations in Non-Halogenated Fire Suppression Technologies

Hamins et al. [28] looked into the flame retarding qualities of CF_3Br, CF_3I, C_2HF_5 (HFC-125) and C_3HF_7 (HFC-227ea) when applied to a baffle stabilized diffusion flames of JP-8 jet fuel injected through a 7.3 cm-i.d. spray burner. The work is performed to gain insight into how these materials might react in the hot confined space of an aircraft engine. The duct is equipped with time release vessels that inject the suppression agents into the inlet air supply stream surrounding the jet spray. With regards to the fire retarding capacity of these materials, Hamins et al. find identify a number of trends as follows:

1) Increased air flow rates minimize the mass of agent required to extinguish the flames;

2) Suppression agent concentrations approach the free stream concentrations when injection times are long permitting experimentalists an opportunity to calculate critical concentration thresholds as a function of the mixing or entrainment time;

3) As the temperature of the gases around the flame increase from 15-350 °C the mass of agent required to extinguish the flames increases and the initial performance ranking of the agents changes;

4) The agent concentration required for extinguishment increases when the pressure of the air inflow increases.

Hamins et al. did perform some preliminary experiments with baffle stabilized pool fires and found that the inject times required to suppress the flames were of an order of magnitude greater than those required for the spray burner. The authors attribute this difference to the change in duct area blockage when the baffle shape is altered.

Lemon et al.[29] wrote a proposal for fabrication of a non-halogenated suppression agent that can combat the phenomenon of reignition in aircraft engines by adhering to hot surfaces and cooling the metal below the autoignition temperature of the jet fuel. Experiments were conducted in an aircraft engine mock up using JP-8 fuel and a suppression agent in pellet form. The material was applied to the metal; the duration of time that it hindered ignition of the fuel in the hot environment was recorded. The authors indicate that it would be advantageous if the fabricated substance was of a nature

wherein its vapors could participate in quenching of the flame zone when the material is introduced upstream. Lemon et al. conclude that a solid component comprised of several elements would work best. They recommend the mixing of fast and slow extinguishing materials bound in a copolymer which could be broken into pellets and mixed in a suspension of easily atomized liquefied halon gas (also known as thixogel).

Joulain and Torero[30] and Yang and Grosshandler[31] have looked into the use of solid propellant gas generators (SPGGs) as an alternative to halons as fire suppression agents for aircraft engines. Like the thixogelled pellets, SPGGs are small in size and have a long storage and service life. Yet, they are neither ozone depleting nor do they contribute to the global warming problem. SPGGs are introduced to the reaction zone by virtue of gas generators containing the pellet propellants. An igniter inside the generators initiates combustion of the tablets which rapidly react releasing gaseous and particulate combustion by-products. Before release to the reaction zone, the by-products pass through a filter which cools the gases and traps the particulates. The predominant gas-phase combustion product is nitrogen which would makes it an appropriate fire prevention tool. The solid propellant gas generators are the principle mechanism behind automobile airbags[31].

Finally, Roberts[32] designed and built a bench scale facility to assist Joulain and Torero with their investigation of the technology's fire suppression capacity. The apparatus is a simple ramjet mock up featuring a rearward-facing step of variable height enclosed in a small scale wind tunnel. The effect of the step is not only to recreate the recirculation patterns that occur in jet engines, but also to stabilize the flames of a porous plate burner situated just behind it. Typical air flow speeds range between 1 – 5

m/s. To date, the wind tunnel is still in a state of development, fire suppressing materials have not yet been introduced into the configuration.

OBJECT OF THE CURRENT WORK

The objective of this report is to investigate the process required to numerically model the induced recirculating flow into which the solid propellants would be released. A large eddy computational fluid dynamics model with subgrid Smagorinsky viscosity model is applied to the wind tunnel constructed by Roberts and housed at the University of Maryland Fire Engineering and Thermal Sciences Laboratory. The numerical modeling aspect of this project began by simulating the computational domain and altering parameters in order to see the effect of these variables on the structure of the recirculation zone. The code utilized for this task was authored at NIST and is referred to as LES-3d. The goal of this work is to evaluate and compare virtual flow patterns with those occurring in the real test facility. The variables modified included flow velocity, surface slip boundary conditions, inlet length, flow profile, and temperature.

Results from an initial investigation led to a more in depth study of the code's function. With the knowledge gained from careful review of the results, the factors relating to the code sensitivity, flow profile, and the simulated wind-tunnel geometry are coordinated to give the most correct set of results possible at this time. The hope is that the results generated here follow trends seen in actual experiments. Likewise, depending on the outcome, efforts will be made to determine whether the numerical results can be scaled to predict outcomes of the flow of the test facility.

The work presented here is performed in conjunction with the National Institute of Standards and Technology.

CHAPTER 2

PRELIMINARY CODE VALIDATION

The first stage of the study began with the intent of using the code as an end-user in the field would. Without scrutinizing the code's operation or basis of assumptions, the aim was to look at the output of flow patterns that are generated by changing flow speeds, flow profiles, surface roughness, and inlet conditions. LES-3d requires the user to define the computational domain walls as a series of adjacent constant cross-section rectangles. Obstacles, rectilinear prisms, are distributed within the domain to give it a form reminiscent of the physical structure one is trying to reproduce. The coordinates of the walls and the obstacles are set by the user in an input file. LES-3d reads the input file and imposes a rectilinear three dimensional grid onto the simulated structure. The Navier-Stokes equations, modified for low Mach number flows are then iterated across each grid space to generate the data relating to temporal and spatial variations in flow properties.

Here, the rectangular planes of the computational domain's exterior walls form an open-ended prism with the dimensions of the test section portion of the University of Maryland wind tunnel. The prism dimensions are 0.9m long x 0.09m wide x 0.09m+H high where H is the height of the rearward facing step. Mass enters through a 0.09m x 0.09m vent, travels the length of the prism and exits through the 0.09m x 0.09+H m vent at the opposite end shown in Figure 1. A preliminary validation of the code was conducted before running the formal simulations. Setting the step height to zero, a constant cross section duct was modeled. Specifying a fully developed parabolic flow

profile, initial simulations were executed to determine whether boundary conditions were preserved. Y- and z- velocities vanished across the domain for a 1 m/s flow travelling the length of the duct. Likewise, centerline velocities decayed as predicted at the walls indicating the persistence of the boundary conditions. Profiles generated from velocity sampling routines indicated that the flow was also symmetric about the y- and z- axes. These measurements were made by placing virtual flow probing devices called "thermocouples" in a cross formation down the length of the duct. Previous editions of the code were unable to generate these results. The January 1998 edition of the code with its changes increased the likelihood that the LES-3d code could be used to accurately assess small-scale closed flow field dynamics. The code has been revised since then. Nonetheless, to maintain continuity of results, all simulations refer to the January edition of the code unless otherwise stated.

THE EFFECT OF COMPUTATIONAL DOMAIN DESIGN ON RECIRCULATION LENGTH

The first experiments address flow profile options and test section inlet length. The objective is to determine the extent to which conditions upstream affect the structure of the average recirculation zone established behind the step. The inlet to the virtual test section is added by extending the computational domain backwards and introducing an obstacle. The length of the test section portion of the duct after the step remains 0.9m in length. The back face of the obstacle forms the step as illustrated in Figure 1. The initial

step height is 0.057m. The recirculation zone is denoted by Le for "eddy length". This term, when normalized by the step height, is referred to by the symbol Xr.

To continue, parabolic and top-hat profiles were applied to flows moving down the duct. These are two of the three preset velocity profiles that can be specified in the input file to be interpreted by LES-3d. The third is atmospheric and is inappropriate for internal flow scenarios such as the one described here. Using the former profiles helped determine the degree of variation possible in the measured recirculation zone lengths. Table 1 features a spectrum of the various tests performed. Here the reference velocity specified at the vent entrance is set to yield equivalent flow conditions for the two different profiles. To clarify, the nature of the flow profile was assessed such that the user-specified centerline velocity of each profile would correspond to the same flux of mass and momentum down the duct. Detailed in a later section of this report, this corresponded to a 1 m/s inlet velocity for top hat profiles and 1.5m/s for parabolic ones.

Table 1: Effect of Entrance Length of Recirculation Zone Length

Velocity Profile	Slip Condition	Inlet Length [m]	Le[cm], Xr	U supplied [m/s]	Centerline Inlet Velocity [m/s]	Grid Spacing
Top Hat *Step1l.data*	Partial Slip	0	40, 7.0	1	1	60,6,12
Top Hat *Step1c.data*	Partial Slip	-0.25	45, 7.9	1	1.08	117,9,18
Top Hat *Step1gL.data*	Partial Slip	-0.9	43, 7.5	1	1.13	234,9,18
Parabolic *Step1a1.data*	Partial Slip	0	40, 7.0	1.5	1.5	60,6,12
Parabolic *Step1f.data*	Partial Slip	-0.25	32, 5.6	1.5	1.3	117,9,18
Parabolic *Step1gL5.data*	Partial Slip	-0.9	37, 6.5	1.5	1.3	234,9,18

With velocity sensitive thermocouples along the centerline of the inlet and across the face of the exit, the average velocities at these points were obtained over a 60s sampling time. The dimension L_e is measured by generating additional data files, slice files, that can be converted into time-averaged pictures of the flow as it moves through the computational field. The eddy length, a characteristic of the flow, is defined where flow streamlines terminate in a stagnation point along the floor of the test section. Upstream of this point, flow recirculates behind the step. Flow downstream of this point exits the wind tunnel.

Permitting the flow to develop between x=-0.25m and x=-0.9m, results in a change in the size of the average recirculation zone which is not a direct function of the developing distance. The recirculation zones for these simulations with accompanying streamlines are depicted in Figures 2 and 3. The developing lengths of -0.25m and -0.9m were selected such that the first measured 4 times the step height [26], and the second was equal in length to the test section. It has been demonstrated by Armaly et. al [11] that an inlet equal in length to the test section should provide a sufficient developing distance for the flow. The grid spacing was set arbitrarily on the basis of preliminary simulations. The aspect ratio of the individual cells was held constant as additional length was added to the inlet. One should not be overly concerned with the grid spacing at this point. The objective here is to identify variations in the structure of the recirculation zone with changes in upstream conditions.

Focusing on the top hat conditions first, the centerline inlet velocity does increase directly with the length of the inlet reaching a maximum speed of 1.13 m/s (x=-0.9m). Where the flow is prohibited from developing, the recirculation zone of the underdeveloped flow takes on the structure of a very tight spiral. As the flow is

introduced into the computational domain through an inlet, the recirculation zone decreases in height and the core of the zone appears to be displaced downstream as shown in Figure 2b. The length of the region is greater than that in the previous case, therefore one can presume that the volume of the entrained fluid is maintained between the two scenarios. In Figure 2c, the recirculation zone decreases slightly, but retains the flatter structure of the previous test case. The core of the vortex anchored behind the step resumes the position it occupied in the initial case. This indicates that the stability of the region is a function of inlet length. To generate reliable simulations, it is necessary to identify the conditions which would generate steady-state conditions upstream of the step.

In Figure 3 where parabolic profiles have been preset, the flows adopt fuller more elliptical recirculation zones than the top hats. This is attributable to the fact that the faster moving central core of the parabolic flow, because of its excess momentum, does not "sense" the drop into the test section until slightly later. The slower moving peripheral flow fills the space behind the step creating an adverse pressure region that draws the bulk of the flow into the characteristic recirculating pattern. L_e is greatest in the first case where the flow is prohibited from developing. Shown in Figure 3b, with the additional length added to the test section inlet, the core of the vortex is displaced backwards closer to the step indicating a greater degree of stability. L_e decreases slightly because the profile has had a chance to fill out and develop as a result of the nascent boundary layer growth encouraged through the inlet. As shown in Figure 3c, the recirculating flow is not pressed against the floor of the duct to as great an extent as in either of the previous cases. This suggests that as the entry length is increased, the

volumetric contribution of flow sucked backwards into the recirculating region becomes comparable to that moving downward as a result of the sudden change in geometry. This holds true for the top hat flows, also.

THE EFFECT OF UPSTREAM SURFACE BOUNDARY CONDITIONS ON RECIRCULATION LENGTH

In Table 2, the effect of surface roughness, specifically the surface slip boundary condition along the walls of the computational domain, was examined. The LES-3d code contains three slip condition provisions: nonslip, free slip, and partial slip. The nonslip condition assigns velocity values along the wall grid cells that force the velocity at the solid-fluid interface to equal zero. In so doing, a boundary layer is permitted to develop across the computational cell on the flow side of the interface. In the case of a top hat flow, the free slip condition assumes that the flow against the wall moves with the same velocity as the central region of the flow. The flow gradient at the wall is forced to take on a zero value. One can study the movement of a fluid within a flow continuum when this condition is specified. The partial slip condition is a marriage of the previous two conditions. The flow against the wall is permitted to move at half the velocity of the central region of the flow according to a protocol that forces the wall velocity to take on that value. Here, only partial slip and nonslip flow scenarios were studied. Flows were subjected to a developing distance of -0.9m, the length of the test section. Flow speeds were limited to 1.0 m/s and 1.5 m/s for the top hat and parabolic flow simulations

respectively. Variations in eddy length are used to qualify the effect of the upstream slip condition on the reattachment dynamics taking place downstream.

Table 2: Effects of Surface Boundary Conditions on Recirculation Zone Length

Velocity Profile	Slip Condition	Inlet Length [m]	Le [cm]	U supplied [m/s]	Centerline Inlet Velocity [m/s]	Grid Spacing
Top Hat *Step1gL.data*	Partial Slip	-0.9	43	1	1.13	234,9,18
Top Hat *Step1gL2.data*	Nonslip	-0.9	41	1	1.3	234,9,18
Parabolic *Step1gL5.data*	Partial Slip	-0.9	37	1.5	1.3	234,9,18
Parabolic *Step1gL4.data*	Nonslip	-0.9	37	1.5	1.32	234,9,18

The recirculation zone structure is graphically represented in Figures 2c, 2d and Figures 3c, and 3d. What is gained from these results, is that the flows travel faster and develop sooner when passing over nonslip surfaces compared to those designated as partial slip. It is important to note that the slip condition is applied to the step only; the rest of the domain is comprised of partial slip walls and surfaces. In the case of the top hat flow, the fluid passing over the nonslip step acquires a velocity at the test section that is 13% faster than that of the flow over the partial slip step. The extended inlet allows the flow to develop from the flat pre-set top hat profile prior to entering the test section. The nonslip boundary condition requires that the centerline velocity accelerate to compensate for the fluid friction effects slowing the flow along the step. Likewise, the dynamics taking place at the step surface occasion the flow to curl downward into a vortex sooner, at 41 cm verses 43 cm in the partial slip case. There is very little difference between the nonslip and partial slip parabolic flow scenarios. This indicates that within the range of

$$U_{duct\ exit} = 1.1182\ U_{supplied} + 0.036.$$

The velocity in LES-3d's input file is set in order to generate a fully developed velocity profile with a centerline speed equal to that measured at the duct exit of the actual apparatus.

With the velocity relationship established, the next step is to determine dependence of recirculation zone length and stability on the flow Reynolds number. The step height was held at 0.057 m. Flow speeds slower than 0.1 m/s are within the regime where numerical fluctuations generate instabilities in the data which are of the same order of magnitude as the flow velocity -- approximately 0.05 m/s. The experimental apparatus is limited to flow speeds less than 5 m/s. Therefore the velocities tested in the following experiments ranged from 0.105 m/s to 4.5 m/s. Re varies from 400 - 17,125. One can obtain a sense of how the velocity of the flow varies with height above the duct floor and position downstream of the step by reviewing Figure 4. A map of the thermocouples used to generate these figures is included in Figure 5.

In Figure 6, eddy length has been normalized by the step height and plotted to demonstrate the variation that takes place as a function of the flow speed. The curve rises and then falls steadily to a plateau. The form of this curve is expected on the grounds of experimental research performed by others who have investigated flow dynamics behind rearward facing steps [11,30]. Extrapolating from the physical apparatus to the numerical model, the curve depicted here is a graphical representation of the fundamental characteristics of the computational flow domain. One expects the

distribution of data points will coincided exactly for identical experimental set-ups. Thus for comparison purposes, the experimental assessment of eddy variation has been included.

L_e is measured experimentally by photographing the evaporation of a bead of oil suspended on a hot wire just upstream of the step. The wire is placed across the width of the test section inlet 3mm before the step and 1 mm above the inlet floor. A bead of solder oil is placed on the wire. When heated the bead smokes; the flux of air past it produces the smoke trace. The wire is positioned such that the smoke follows the flow streamlines nearest the wall. The smoke traces are photographed with a CCD camera. Fluctuations and mixing in the flow make it necessary to implement an image averaging process to determine the length of the recirculation zone [32].

A sequence of 25 images is captured by means of the EPIX XCAP software. The images are digitized to gray levels and treated individually. A threshold value is established that provides an adequate representation of the smoke traces. The threshold value is kept constant for an entire set of the images. The images are then binarized assigning "1" to any gray higher than the threshold and "0" to any gray level below the reference value. Thus, below the threshold all hues of gray are treated as black; above it, all hues of gray are considered white. After all 25 images have been modified to black and white, the entire sequence is then combined to create one total average of all the images. This produces an averaged gray area. By identifying the locus of the maximum intensity the borderline of the average recirculation zone and subsequently Xr can be determined [33].

Nonetheless, the vertex of the parabola occurs in the neighborhood of Re = 8000 where experimental values of Xr stretch to a maximum of 4.5. At larger values, Xr falls slightly and then reaches an unsteady transition where Xr grows rapidly beyond Re = 12,000. The numerical simulation outputs a peak value of 8.2 in proximity of the maximum experimental value. The vertices of the two parabolas overlap indicating at least one degree of similarity between the two sets of experiments. However, the model predicts values of the recirculation length that are nearly two times that of the experimental values. The disparity indicates that the model is not the exact representation of the experimental flow field which it was presumed to be. (A more vigorous introspective approach is required to determine both domain design and algorithmic factors that may be contributing to the discrepancies.)

It is possible, however, that the code has been programmed to provide more accurate results when incompressible conditions have not been forced. LES-3d is a software that has been designed specifically to simulate fire scenarios although it can also be applied to cold flows. By introducing a thermal heat source into the simulation, density is permitted to vary spatial and temporally across the domain with respect to the position of the heat source. A heating element was introduced into the model in the form of a virtual hot plate. The hot plate was placed just behind the step exactly as it appears in the physical wind tunnel. The dimensions of the virtual plate correspond to those of the actual device which measures 0.12 m long x 0.09 m wide and takes up the entire floor of the test section. The hot plate was coded in the input file as an infinite thermal heat source whose temperature does not change during the duration of the simulations. Two temperatures, 300 °C and 600 °C were examined. The data from these tests appears in

Figure 7 along with the experimental results. Thermal contour plots of the computational domain show that the bulk flow does not become hotter than 20 °C at the end of the recirculation zone. Therefore, the Reynolds number is plotted according to viscosity values measured at 20 °C. The effect of the temperature on the flow properties was studied experimentally by Roberts [32]. Sample contour and vector plots are included in Figure 8. It is interesting to note that as the plate temperature increases, the buoyant forces become strong enough to displace the recirculating flow off the floor of the duct. Yet, the form of the recirculation zone is not compromised as thermal energy is pumped into the spiraling fluid

The modeled results show that the parabolic curves peak at slightly higher Reynolds numbers as the temperature at the foot of the step increases from 15 °C to 600 °C. Both the 300 °C and 600 °C curves possess the same peak values of Xr. As the temperature of the simulation increases, the agreement between the experimental and numerical results improves. The numerical results for the 300 °C and 600 °C tests respectively are only 26% and 22% larger than the maximum experimental values of Xr. This is in contrast to the cold case, where the numerical results exceed the experimental by 46%. These results demonstrate that LES-3d like other computational fluid dynamic codes generate better simulations when the viscosity is maximized. Nevertheless, the investigative process utilized here is geared towards identifying similarities in trends between the physical and virtual flow patterns.

ENTRAINMENT RATES

Before moving on to the more rigorous study of the formulation of the LES-3d code geared towards identifying the source of discrepancies between the experimental and modeled flows, we wish to use the results collected to get a sense of the amount of flow that is entrained behind the step. Entrainment like Xr is also a function of the flow speed. This parameter is calculated by generating time averaged pictures of the flow profile behind the step along the length of the duct. U-velocity sensitive thermocouples were placed according to the scheme mentioned above and illustrated in Figure 5. Each column of thermocouples is positioned 7.6 cm downstream of one another with the exception of the thermocouples denoted by asterisks (*) which are 3.8 cm from the previous thermocouple. The vertical position of each probing device is selected to correspond to inlet and step features. For example, Row 1 thermocouples refer to the center of the inlet; Row 3 thermocouples correspond to the half-height of the step. Plotting the velocity data of each column of thermocouples as a function of their vertical position yields profiles such as those in Figure9.

To come up with entrainment rates, the portion of the profile on the negative side of the x-axis was integrated using the trapezoidal method of integration. This portion of the graphic refers to the backward moving flow that is drawn into the recirculation zone. The area corresponds to $\int_0^{y_o} \rho u \, dy$ which has the units of [kg/ms]. This value is multiplied by the width of the duct to arrive at units of [kg/s]. Here, y_o is the height where u=0 m/s. Profiles for three of the velocities showcased are included in this analysis. Figure 10 is the compilation of results from the 0.88 m/s, 2.65 m/s, and 3.99 m/s simulations. Since the flow is highly three dimensional, the entrainment values are slightly underestimated as can be deduced from the analysis of Shih and Ho[6].

Entrainment is another fundamental characteristic of the flow domain. There is a point along the duct where flow entrainment either downstream or upstream of it is necessarily smaller. Here the entrainment maxima occur 0.15m from the step for the two slower speeds and at 0.229 m for the faster flow. The plot also illustrates that the mass entrained increases as the flow rate increases. This is expected since faster speeds imply greater volumetric flow rates: a greater quantity of fluid will necessarily be set into circulation behind the step. When the flow speed is 0.88 m/s the mass entrained is 1.40×10^{-4} kg/s and increases to a maximum of 5.14×10^{-4} kg/s for the faster 3.99 m/s flow. The results displayed are significant because for a diffusion flame to be sustained behind the step, the oxidizer and fuel concentrations must be such that the flame stays anchored to the duct floor. The two dashed lines on the plot refer to the quantities of air required to maintain stoichiometric combustion with propane injected at 6 cm^3/s and 16 cm^3/s. The simulated entrainment values fall between the range of the two stoichiometric thresholds indicating that in theory a fuel rich environment occurs inside the test section. Indeed, this would be a worst case scenario for addressing reignition. In a lean environment a flame has a tendency to lifts off and adhere to the top edge of the step. This type of flame can be easily blown off by increasing the air flow speed through the duct. The objective of the experimental tests is to generate a robust and persistent flame that is anchored behind the step. For this to be the case, sufficient air is necessary to attain a flammable mixture. What this numerical data implies is that the burner to be built into the physical device must be positioned slightly downstream such that the air flow available to the flame is sufficient to realize the proposed worst case scenario.

STABILITY ASSESSMENT

Mentionned earilier, the stability of the flow behind the step has been brought into question. A view of the smoke seeded experimental flow illustrates that the flow pulses, retreating from time to time back to the step and then bursting away from it several centimeters. Neither the average recirculation zone nor the entrainment rate provide any evaluation of the stability of the flow, therefore an analysis of the time dependent velocity is conducted to identify whether the phenomenon of vortex shedding may be operative here.

The velocity measuring thermocouples used to generate the downstream flow profiles recorded velocity fluctuations over the total sampling time. Time dependent velocity measurements are presented in Figure 4 for 3 different positions along the duct. Figure 4a shows the velocity evolution at the inlet. The top trace shows the velocity at the centerline, the perturbations along the average value are notable. The thermocouples below the step measure zero velocities as expected. A cross section at a distance smaller than Xr is shown on Figure 4b. Again strong fluctuations of the velocity around the mean value can be observed. The velocity measurements inside the recirculation zone are characterized by negative values and mean velocity values much smaller than those of the main flow. Beyond the recirculation zone the fluctuations decrease in magnitude and there is a total absense of negative velocities as depicted in Figure 4c. The absense of negative values and the homogeneity of the flow seem to imply an absense of vortex shedding.

It is assumed that the recirculation zone would be demarcated by the position where one duct-floor thermocouple measures a negative velocity and its downstream neighbor measures a positive velocity. Pulsing therefore should be traceable by watching where this negative-to-positive phenomenon occurs and noting whether it sweeps back and forth across the computational domain. The LES-3d code was set to take instantaneous measurements of velocity along the duct floor and produce a data file of the speeds recorded at each thermocouple as a function of time. Figure 11 was produced by tracing *where* the transitions take place.

Review of the graphic illustrates that the transition point seems to oscillate about 6.68 in a fairly random pattern. Within one thermocouple width, this downstream duct position is the same as the time averaged value of Xr=7.8 presented in Figure 6 as the length dimension of the large eddy. There is not an obvious natural frequency here, thus one can disregard the existence of periodic vortex shedding. Nonetheless, for exactness, a Fourier transform of the velocity trace just outside the recirculation zone and at the exit of the duct indicate major peaks between 7 and 8 Hz, respectively. However, they are situated within the noise of the transform plot. Vortex shedding would be characterized by a striking identifiable feature that stands in strong relief against the noise present. The absense of that type of spectra suggests that the low frequency peaks are representative of the large scale motion of the flow. They may also be attributable to oscillations in the numerical solution of the problem. The dearth of distinct higher harmonics indicates that the recirculation zone is indeed stable indicating that the flow in the wind tunnel is indeed the resilient worst case scenario it was intended to be.

INITIAL CONCLUSIONS

In this initial section, without rigorously assessing the working of the code and its basis of assumptions, the effects of domain design including inlet length and upstream surface boundary conditions were investigated by looking at variations in the length of the recirculation region. For each simulation, the mass flux passing through the virtual configurations was held constant, independent of the flow profile specified by the user. Regarding the surface slip boundary conditions, the flows developed faster core speeds and reattached sooner when passing over nonslip steps as compared to partial slip surfaces. Simulated parabolic flows are less sensitive than top hats to the step's surface roughness, but the trend in the centerline velocity is repeated. Inlet lengths altered the recirculation zone lengths in a non-uniform pattern again pointing to the fact that upstream flow dynamics in the simulated domain, as in the real apparatus, have the capacity to significantly alter the fundamental character of the eddy established behind the step [10]. Stability as evidenced by the presence or absense of a large-eddy shedding frequency was also addressed. Necessarily averaged out of the images generated by Tecplot, the instantaneous velocity traces of the output data also failed to reveal a vortex shedding pattern leading one to conclude that the flow is stable. Low frequency peaks recovered on the Fourier transform plot of the velocity are attributable to the large scale motions of the flow. The sporadic pulsing of the recirculation zone in the University of Maryland wind tunnel is significantly random and sporadic to indeed justify the simulated results.

The assessment of the effect of temperature in conjunction with Reynolds number on the recirculation zone length began to shed some light on the code's performance. Plots of Reynolds number vs. reattachment length were overestimated by LES-3d, but to a lesser degree when a heat source was introduced into the domain design. This suggests that viscosity may be forced to adhere to a particular value when an isothermal flow domain is specified. When heat is introduced to the system, a condition within the code is released and spatially, values of viscosity are allowed to vary with the enthalpy addition of the hot plate and possibly the adverse pressure gradient across the recirculation zone. Without incorporating a different viscosity to temperature correlation into the code, little can be done to consider this point further. Many of the conditions investigated can be intuited with basic analysis of the governing equations. The code's capacity to reproduced most of these basic but subtle phenomenon entice one to continue querying its modeling capacity.

This introductory portion of the report illustrates that the LES-3d program is capable of reproducing the larger flow trends observed experimentally. Graphical reproductions of the data illustrate that the maxima of fundamental characteristics such as variation in recirculation zone length peak within the vicinity of one another eventhough the amplitudes differ by almost 50%. It has also been demonstrated that modeling the computational domain with planes and volumetric prisms with dimensions equal to those occuring in the physical apparatus is not enough to guarantee that the numerical predictions will exactly mirror the experimental flow data output. As a result, it is necessary to come up with a means of assessing the manner in which the code establishes upstream flow conditions and subsequently coordinates them to generate a flow that best

matches the experimental flow. One can not merely guesstimate an entry length on the basis of others' CFD research. Rather, beyond a reasonable doubt, grounds must be established that indicate a fully developed flow with minimal transient effects is set upstream of the step.

It has been shown here that it is helpful to make use of a velocity correlation to maintain a consistency in the flow velocities applied to both the experimental and virtual devices. If additional tests can be generated to improve the relationship between the experimental and numerical flow patterns, the usefulness of the simulations will become noteably greater. As it stands now, Figure 12 illustrates that depending on the definition of the computational domain, the value of Xr for the 1 m/s cold flow can be anywhere between 1 ½ to two times greater than the experimentally measured value. The next chapter is geared towards identifying factors that may be inhibiting convergence of the experimental and simulated results.

CHAPTER 3

HOW LES-3D WORKS

The LES-3d code is a very flexible software that permits the user to specify a number of conditions about a flow and the structure of its computational domain. The code reads an input file written by the user that defines the spatial boundaries of the flow domain, the location and shape of any physical obstacles within the domain, and many of the initial conditions including boundary conditions, temperature, fluid density, heat fluxes and volume fluxes. Within this input file, the user also sets the amount of time the flow is to be simulated, the position of virtual probing devices, and the calculation optimizing parameter -- namely the grid size -- to be used to resolve the flow field. The code uses a Lagrangian approach to calculate the evolution of flow parameters including viscosity, velocity, heat release rates, momentum, pressure, species concentrations, temperature, and density. The motion and properties of the fluid are calculated in time and space with the Navier-Stokes governing equations referenced to an initial user-specified configuration.

Developed by NIST, the LES-3d code was designed to provide engineers with a modeling tool that could sufficiently resolve the open-air and enclosed industrial fire phenomena studied in the field. The intent was to develop a software that did not require access to mainframes. The researchers at NIST created a software that generates reasonable engineering solutions on desktop workstations. LES-3d accomplishes this goal by discretizing the governing equations against a three dimensional rectilinear grid which covers the simulated flow domain. The choice of a rectilinear grid was made

because it can be modified to fit the design of most fire and flow scenarios. The discretization is facilitated by using finite difference approximations of flow variables between grid cell.

APPROXIMATING FLOW PROPERTIES USING FINITE DIFFERENCE

Flow variables are defined as continuous over time and space. The spatial domain (L) is divided into uniformly spaced grid cells according to the number of cells (N) prescribed by the user in the input file. The time span is fixed by the user.

The standard Taylor expansions [34] of a two dimensional variable such as velocity is approximated by

$$u(x,t+\delta t) = u(x,t) + \delta t \frac{\partial u}{\partial t}(x,t) + \frac{\delta t^2}{2}\frac{\partial^2 u}{\partial t^2}(x,t) + Higher\ order\ terms(\delta t^3)$$

to tabulate changes in time at a fixed location, and

$$u(x+\delta x,t) = u(x,t) + \delta x \frac{\partial u}{\partial x}(x,t) + \frac{\delta x^2}{2}\frac{\partial^2 u}{\partial x^2}(x,t) + Higher\ order\ terms\ (\delta x^3)\ .$$

to assess the function's value at a new position in the flow at a fixed time.

When the domain is discretized , it is broken up into N cells each of length δx (= L/N) and n evenly distributed time intervals of δt seconds. The velocity term with regard to the n th time step at the Nth grid cell is expressed as $u_N^n = u(i\delta x, n\delta t)$ where i corresponds to values of δx in the positive x direction. Therefore, the above Taylor series expansions can be rewritten as

$$u_N^{n+1} = u_N^n + \delta t\left(\frac{\partial u}{\partial t}\right)_N^n + \frac{\delta t^2}{2}\left(\frac{\partial^2 u}{\partial t^2}\right)_N^n + H.O.T.(\delta t^3)$$

for an incremental change in time at a fixed position, and

$$u_{N+1}^n = u_N^n + \delta x\left(\frac{\partial u}{\partial x}\right)_N^n + \frac{\delta x^2}{2}\left(\frac{\partial^2 u}{\partial x^2}\right)_N^n + H.O.T.(\delta x^3)$$

for an incremental change in position at a fixed time [34]. According to this scheme, vector quantities are evaluated at the centers of neighboring cells; scalar quantities, at the edges. Derivatives of these quantities are approximated by first solving and replacing them back in the above series expansions. For example,

$$\left.\frac{\partial u}{\partial t}\right)_N^n = \frac{u_N^{n+1} - u_N^n}{\delta t} + H.O.T.(\delta t)$$

$$\left.\frac{\partial u}{\partial x}\right)_N^n = \frac{u_{N+1}^n - u_{N-1}^n}{2\delta x} + H.O.T.(\delta x^2)$$

$$\left.\frac{\partial^2 u}{\partial x^2}\right)_N^n = \frac{2}{\delta x^2}\left(u_{N+1}^n - u_N^n - \delta x\left(\frac{u_{N+1}^n - u_{N-1}^n}{2\delta x}\right)\right) + H.O.T.(\delta x^3) = \frac{2}{\delta x^2}\left(\frac{u_{N+1}^n + u_{N-1}^n}{2} - u_N^n\right) + H.O.T.(\delta x^3)$$
$$= \frac{u_{N+1}^n - 2u_N^n + u_{N-1}^n}{2\delta x^2} + H.O.T.(\delta x^3)$$

The value of a given flow parameter is checked against a self-correcting scheme that limits the size of each subsequent time step by the CFL condition where $\delta t < \min(\delta x/u, \delta y/v, \delta z/w)$ (Courant, Friedrichs, Lewy, 1928). This bounds the equations solved and prevents excessive oscillations of the functions describing each unknown variable. This method of discretizing the equations, and the selection of a rectilinear grid enhance the processing capacity of most desktop machines, making the LES-3d code the powerful and flexible software it is.

ASSUMPTIONS UTILIZED IN THE LES-3D FORMULATION

A number of assumptions are introduced that further optimize the processing capacity the workstation as it solves equations of the above mentioned form. The standard conservation equations of mass, species, momentum, and energy for a mixture of ideal gases are as follows [35,36]

$$\frac{\partial \rho}{\partial t} + \nabla \bullet \rho \underset{\rightarrow}{u} = 0 \qquad \text{Conservation of Mass}$$

$$\frac{\partial}{\partial t}(\rho Y_i) + \nabla \bullet \rho Y_i \underset{\rightarrow}{u} = \nabla \bullet \rho D \nabla Y_i + \dot{W}_i''' \qquad \text{Conservation of Species}$$

$$\rho\left(\frac{\partial \underset{\rightarrow}{u}}{\partial t} + (\underset{\rightarrow}{u} \bullet \nabla)\ \underset{\rightarrow}{u}\right) + \nabla p = \underset{\rightarrow}{f} + \nabla \bullet \tau \qquad \text{Momentum Conservation}$$

$$\frac{\partial}{\partial t}(\rho h) + \nabla \bullet \rho h \underrightarrow{u} - \frac{Dp}{Dt} = \dot{q}''' + \nabla \bullet k \nabla T + \nabla \bullet \sum_i h_i \rho D \nabla Y_i \qquad \text{Energy Conservation}$$

Here, $\dot{W}_i'''$ refers to the production rate of the ith gaseous species per unit volume; $\dot{q}'''$ is the rate of heat release per unit volume. In the momentum equation, $\underrightarrow{f}$ constitutes the buoyancy and external body forces acting on the fluid. τ is the viscous stress tensor whose components are derived from the constitutive equations

$$\tau_{ij} = \mu\left(\frac{\partial u_i}{\partial x_j} + \frac{\partial u_j}{\partial x_i} - \delta_{ij}\frac{2}{3}\frac{\partial u_k}{\partial x_k}\right)$$

where δ_{ij} is the Kronecker delta.

The main assumption here is that the flow speeds of the simulated phenomenon are much slower than the speed of sound. This filters out multiple pressure wave reflections, yet allows for variations in temperature and density subject to the limitation that the Mach number is 0.3 or less [35]. Implied is the notion that the convective transport time scale dominates. Limits on the time-step size, therefore, are governed by convective processes and the spatial resolution of the grid, only. The governing equations become elliptical in nature when this assumption is applied. This form for the partial differential equations "is consistent with low speed, thermal convective processes" and lends itself to the discretization process which is important to enhance the processing speed [36].

The second assumption is that pressure can be decomposed into background and perturbation terms such that

$$p(\underset{\sim}{x},t) = p_o(t) + \hat{p}(\underset{\sim}{x},t)$$

In this form, the pressure expression constitutes a thermodynamic equation of state which compliments the three governing equations. Inherent in the background pressure term is a hydrostatic component which is a function of gravitational acceleration, density referenced to ambient conditions, and an altitude above sea-level at t=0. The low Mach number flow assumption in conjunction with the ideal gas law permit a secondary substitution to be made. Background pressure can be expressed in terms of the fluid temperature and density as

$$p_o = \rho \sum_i \left(\frac{Y_i}{M_i} \right) \Re T = \rho T \frac{\Re}{M}$$

where $\Re$ is the universal gas constant and M, the molecular weight of the mixture. With the acoustic waves surpressed, the higher order perturbation terms, differentiated with respect to time, are negligible. In a small scale enclosed system, such as the one studied here, pressure in the momentum equation can be replaced by the above expression for background pressure. This equation links the expression of pressure to not only density, but also enthalphy.

The specific heat at constant pressure is independent of temperature for each gaseous species making up the flow according to another assumption made in the formulation of the LES-3d code. This thermodynamic property is derived on the basis of the internal degrees of freedom of each molecule composing the fluid. γ is equal to the

ratio of specific heats for each species, which is directly related to the degrees of freedom within the molecules. The constant pressure specific heat is expressed in the code as

$$c_{p,i} = \frac{h_i}{T} = \left(\frac{\gamma_i}{\gamma_i - 1}\right)\frac{\Re}{M_i}.$$

Direct substitution into the equation of state yields

$$p_o(t) = \rho T\left(\sum_i \left(\frac{\gamma_i - 1}{\gamma_i}\right) c_{p,i}\right) = \left(\frac{\gamma - 1}{\gamma}\right)\rho h$$

when all gases posess the same number of internal degrees of freedom.

With regard to the momentum equation, the hydrostatic pressure gradient is subtracted off and a quantity H is introduced to make a distinction between two discrete vorticity effects. The first results from misaligned pressure and density gradients. The other consists of effects generated by both the induction of vorticity into the flow, and the application of unbalanced stresses and external forces including buoyancy forces. H is the pressure term relating to perturbations in the flow. By using the vector identity

$$(\underset{\sim}{u} \bullet \nabla)\ \underset{\sim}{u} = \frac{1}{2}\nabla|\underset{\sim}{u}|^2 - \underset{\sim}{u} \times \omega\ ,$$

the momentum equation, divided by density becomes

$$\frac{\partial \underset{\rightarrow}{u}}{\partial t} + \frac{1}{2}\nabla\left|\underset{\rightarrow}{u}\right|^2 - \underset{\rightarrow}{u} \times \omega + \frac{1}{\rho}\nabla\hat{p} = \frac{1}{\rho}\left(\underset{\rightarrow}{f} + \nabla \bullet \tau\right).$$

Incorporating the definition

$$\nabla H \approx \frac{1}{2}\nabla\left|\underset{\rightarrow}{u}\right|^2 + \frac{1}{\rho}\nabla\hat{p}$$

and substituting, the momentum equation takes on the final form [35]

$$\frac{\partial \underset{\rightarrow}{u}}{\partial t} + \nabla H = \underset{\rightarrow}{u} \times \omega + \frac{1}{\rho}\left(\underset{\rightarrow}{f} + \nabla \bullet \tau\right).$$

To continue with the list of modifications to the formulation of the equations for the LES-3d code, sub-grid scale motion is simulated by incorporating the Smagorinsky correlation. This formulation assumes that all macroscopic fluid motions can be accounted for on a microscopic grid-cell level. It is often difficult to prescribe a grid resolution on a workstation that is fine enough to capture the significant mixing processes that contribute to viscosity measurements. Thus, to properly balance the kinetic energy of gross motions with the dissipative effects of viscosity, the latter internal fluid phenomenon is scaled by the Smagorinsky constant. Since viscosity is directly related to vorticity generation, the correlation provides a reasonable approximation for flow turbulence when applied at the sub-grid level. Therefore, instead of defining the dynamic

viscosity in terms of the temperature field, viscosity is expressed according to Smagorinsky's analysis of circulation as [35,37]

$$\mu = \rho(C_s\Delta)^2|S|$$

where C_s is the empirical constant, and the characteristic length scale measured in meters is expressed as $\Delta = (\delta x \delta y \delta z)^{\frac{1}{3}}$. |S|, the deformation tensor, and is defined as

$$|S|^2 = 2\left(\frac{\partial u}{\partial x}\right)^2 + 2\left(\frac{\partial v}{\partial y}\right)^2 + 2\left(\frac{\partial w}{\partial z}\right)^2 + \left(\frac{\partial u}{\partial y} + \frac{\partial v}{\partial x}\right)^2 + \left(\frac{\partial u}{\partial z} + \frac{\partial w}{\partial x}\right)^2 + \left(\frac{\partial v}{\partial z} + \frac{\partial w}{\partial y}\right)^2.$$

This expression of viscosity is factored into the components of the stress tensor in the modified momentum equation which is why μ must be prescribed.

To reduce the computational costs, NIST programmers agreed on a fixed value of 0.21 for Cs after comparing plume dynamics with the correlation [38]. This fixed as opposed to a variable constant was incorporated into the LES3d code. When a direct numerical simulation is called for, flow field viscosity is evaluated according to the ratio of the flow field and background temperatures. Alternatively, dynamic viscosity as factored into the stress tensor components in a DNS simulation becomes

$$\mu = \mu_o\left(\frac{T}{T_o}\right)^{0.75}.$$

A number of allowances must be made for pressure conditions at boundaries through which flow passes. Pressure perturbations at open external boundaries are assumed to be zero. To guarantee continuity of flow at open boundaries, the derivative of the pressure normal to the opening is set equal to and opposite the sum of external forces acting normal to the boundary and the rate of change of the normal component of velocity. The differentiated pressure term is invariable with time. Where walls are solid, the normal component of the velocity at the wall is fixed and does not change in time; indeed its value is zero when the initial flow velocity is zero. The normal of the pressure term in this case is balanced by the normal component of external forces acting on the wall. At boundaries through which flow is infusing, an infinite source is assumed to provide the volume flux: the pressure perturbation term is set to zero. Velocity is initially zero; the user prescribes the tangential component of the flow at inlets. At passive outlets, the total pressure is assumed constant along streamlines. The flow is said to exhaust to an infinite reservoir. Therefore the momentum equation becomes

$$\nabla^2 H = -\frac{\partial(\nabla \bullet \underset{\rightarrow}{u})}{\partial t} - \nabla \bullet F$$

with boundary conditions set by the equation

$$\frac{\partial H}{\partial n} = -F_n - \frac{\partial u_n}{\partial t}$$

where $H = \frac{|\vec{u}|^2}{2}$ for infusing flows, and $H = 0$ for exiting flows [35]. At solid walls, flow material is prohibited from traversing boundaries by balancing the pressure gradient with the normal component of external and buoyant forces acting against the same surface. Finally, the Prandtl and Lewis numbers -- $\Pr = \frac{\mu c_p}{k}$ and $Le = \frac{k}{\rho D c_p}$ -- are held constant at 0.70 and 1 respectively, for each simulated scenario.

The LES-3d modeling code incorporates a discretizing method and seven assumptions which enhance the processing capacity and efficiency of most desk top machines. For this study, all of the simulations were run on a DEC ALPHA AXP computer equipped with a 533 MHz processor, 256 MB RAM, a 2 GB hard drive, and a secondary partitioned drive with a total capacity over 12 GB.

Although a simple one stage combustion based on Arrhenius rates of reaction can be simulated, this study focuses on cold air flows and flows in the presence of hot plates. Sprinkler systems with their subsequent droplet trajectories can also be incorporated into simulations, but again, these features were not used for this investigation.

At this point, it is worth noting some of the specific conventions used in the code to define the geometry of the computational domain, boundary conditions, and the shape to be adopted by velocity profile.

CONVENTIONS OF THE CODE

Immediately following execution of the code, LES3d begins reading and organizing the input file by counting the number of lines the programmer has specified as having a

particular format. These lines belong to NAMELIST groups, some of which appear below with examples pertaining to their use. The tally of counts are used later to add definition to arrays allocated to store information about particular structures in the domain. Some of the arrays are designated for particle positions, grid cells, and obstacles. Others are for species, thermocouples, slice planes, heat and flow sources. LES3d also makes use of arrays to interpolate values and solve the multilevel differential equations.

The specifics of the computational domain are assessed after the initial counting step. Default values for the number of cells making up the simulated space and its physical dimensions are replaced with actual values. The time step and simulation time are also incorporated. These temporal and spatial values are then used to specify the scaling factors which will non-dimensionalize the governing equations and define the position arrays that translate between grid cell spacing and actual coordinate positions.

LES3d has optional animation features which require input from the particle position arrays and are specified after the non-dimensionalization step. Selecting the "particles" option signals the generation of additional output files (tracked by the subprogram part.f) that will trace the motion of individual particles through the computational domain to be later processed by an animation software known as "Smokeview". Similarly, flow property values can be viewed across a series of planes at particular intervals by setting the PLOT3D option. These output files are read by a software PLOT3d and permit the user to get a sense of the development of flow properties in time in contrast to the view offered by slice files. Slice files permit the user to view the evolution of flow properties in space. The data files, once translated by the software Tecplot, depict flow properties

that are time averaged along a plane or line of interest over the entire simulation period. Slice files are formatted much later in the program.

Following the initialization of the animation data files, the number flux of particles desired, the initial particle volume and the coordinates of each grid cell are saved to the appropriate array structures. Next, the miscellaneous flow parameters, dimensionless groups, and local temperatures are set if different from the defaults.

The code uses the tally of molecular species from the &SPEC namelist group to set the position and initial volume information for each type of molecule present. Radiation and combustion parameters are also set if a reaction has been coded into the input file. The LES3d code can not simulate the chemistry of combustion; however, the heat release and the particle diffusion of a flame can be mimicked. Appropriate specification of heat release and diffusion rates can facilitate the generation of reasonable results for most burning field applications. Species are tracked according to whether they are fuel or oxidizer molecules.

DEFINING THE COMPUTATIONAL SPACE AND FLOW INPUT SOURCES

The code works by decomposing the external walls first before assessing the character of cells inside the perimeter of the computational domain. Each volumetric grid cell is made up of six faces which receive I, J, and K values. The number of wall cells is obtained by fixing I at 0 first followed by IBAR+1 (or IBP1) -- the external side of the back face of the domain, and sweeping through all of the J and K values while

incrementing the counting variable NWC[1]. This process is repeated for each plane of the domain. The counting variable's value becomes the reference number IW for the cell. The orientation of each grid cell making up the planes is also recorded. External walls have the classifications IBOX=0 and IVAL=1 and receive the wall velocity value UW(IW)= 0. The cells of solid obstacles are established with orientation, surface condition or material type, and reference numbers the same way the external walls are indexed. The difference is that obstacles are indexed with respect to their &OBST line such that IBOX=N (max N=NB). These cells too receive a velocity of U(IW)=0, a class IVAL=1, and coordinate-position assignments. Thermal identification that presumes a surface has either a heat capacity or a set wall temperature is also read into the vast array for the obstacle cells. Heated walls receive one form of identification; flow sources and external walls receive a different classification.

The critical step of identifying flow sources – vents -- follows. Each &SURF line is parsed for information pertaining to prescribed velocities and velocity profiles. The three permissible velocity profiles are identified as IPROF = 0 for top hats, IPROF = 1 for parabolic flows, and IPROF = 2 for atmospheric profiles. These values are taken into the subroutine CHKVNT that confirms that the surface with the profile specification is indeed a boundary wall containing a vent. Depending on the value of IPROF carried into the subroutine, a profile is applied across the vent area in the direction of flow. Each grid cell is assigned the velocity value appropriate for the prescribed profile. This is readily seen in the atmospheric profile case, reprinted from subroutine CHKVNT [39], where

[1] IBAR, JBAR, and KBAR refer to the total number of grid cells in each of the x,y, and z directions.

UW(IW)= UW(IW)*((Z-Z1)*HGT/Z0) **PLE

Here z is the position coordinate of the current grid cell above the lower bound Z1 of the vent, HGT is the vertical height of the computational domain. Z0 is a reference value, and PLE is the exponent for the atmospheric wind profile which is expressed most commonly as

$$u = u_o\left(\frac{Z}{Z_o}\right)^{ple}.$$

A new velocity value is established at position Z on the basis of the input value specified at Z1. Similar expressions follow for the parabolic case with special attention paid to the orientation of the parabola relative to the vent.

Vents that compose entire walls are demarcated in the input file by "CE" followed by an orientation. EAST and WEST refer to computational domain walls with normals along the positive and negative x axes. NORTH and SOUTH walls have normals along the -y and y axes; TOP and BOTTOM walls have their unit normals pointing in the –z and z directions. The cells making up these walls are read into the vent array and set to receive a particular velocity. If a volume flux has been specified in the input file, its value is divided by the vent area in order to assign a velocity to the vent cells. Vents not comprising an entire surface are assessed by a secondary criteria which checks to make sure they are planar. Next, the type of vent is addressed. All vents have IVAL=0. Passive exhaust vents receive values for IVENT=2 to distinguish them. Symmetry planes have IVENT=3, and forced vents have IVENT=5.

FLOW BOUNDARY CONDITIONS

Of particular interest is how the nonslip, partial-slip, and free-slip boundary conditions are applied to the flow velocity at the surface of each solid wall or obstacle in line of the vent. Slip is considered a sub-grid phenomenon because the slip phenomenon is effected within 1 cell's distance from the solid boundary. Slip boundary conditions are set by the &SURF lines pertaining to the computational domain's walls and the obstacles within it. Within the subroutine VELBC, the boundary condition of each internal- or object- surface is assessed and assigned to a temporary variable BC, BCTOP, BCSID, or BCBOT depending on the type of cell.

Since velocity vectors are evaluated at the centers of neighboring cells, the velocity of cells on either side of a slip plane must be taken into account in order to define a velocity there. The cells just outside the surface are assigned velocities according to the profile prescribed at the vents and their vertical and horizontal position relative to those vents. The nonslip condition infers that fluid sticks to the walls of the duct or exposed surface according to the law of the wall. The velocity along the walls must therefore be fixed at zero and ramp up to the velocity of the flow above it, ultimately reaching the freestream velocity over several grid cells as the result of diffusion and deformation effects inherent in the Navier-Stokes equations. This is achieved by associating a fictitious velocity to the outermost cell of the object as illustrated in the following figure.

Figure 13 shows 4 cells aligned vertically and viewed from one side. This is a simple representation of a 1cell x 1 cell x 4 cell computational domain with a solid body

suspended within it. Each cell has the same I and J values; they are differentiated from one another according to their K values. The middle two cells denoted by (I, J, KB1) and (I, J, KB2) make up the top and bottom cells of the solid body. Cells (I,J, K01) and (I, J, K02) are just below and just above the object. A flow passes over the top of the object with velocity U. The nonslip surfaces are located at the interfaces of the two different cell types.

A fictitious velocity –1*U is assigned to the top cell of the solid body. The dotted line between the two velocity vectors denotes a non-zero gradient that develops across the two cells. Out of geometrical necessity, U=0 at the interface thus satisfying the nonslip requirements. This generates the sub-grid effect wherein the velocity ramps from zero to U within one cell thickness ultimately contributing to the generation of a boundary layer.

Boundary conditions are therefore set by ascertaining the value of the velocity vector which must be added to itself across the solid-open interface to uphold the boundary slip requirements. The length of the fictitious vector is determined by the value of BC*U. Nonslip surfaces have BC=-1, partial slip surfaces have BC=0.5. BC=1 for free slip surfaces. Where the boundary conditions are set to permit free slip, a zero velocity gradient must be established near the wall. To do this, as shown in the picture, the top cell of the solid is assigned a velocity value +1*U equal to that of the flow above it. The vertical gradient line connecting the vectors illustrates the fact that there is no change in the velocity in the x direction.

The length of the fictitious vector equals half of the original U vector in the partial slip example shown. As in the above two cases, by connecting the vectors, a non-zero

gradient and non-zero velocity are assigned to the interface. "Partial" implies that the parameter BC may take on a value between 0 and 1. BC=0.5 is the default value of slip for all exposed walls and surfaces: it permits the generation of a slight boundary layer above the object and has been found to successfully reproduce flow in the region of a wall for many different experimental flow scenarios[35]. If the experimental surface velocity or gradient is known, the user can specify BC to give the desired results. In this example the interface velocity equals 0.75*U.

With regard to the coding of the slip conditions at the interface between the solid and open grid cells of an object, a series of loops are triggered to cycle in such a way that the exposed cells of each solid surface are located. The cells are selected according to the criteria that their neighboring flow-side cells will have the parameter IVAL set equal to zero. Once all the surface cells have been accounted for, a conditional statement is checked. If the cells above the obstacle, are all open, then the U and V velocities below the exposed top surface will be defined as U(I,J,KI2)=BCTOP*U(I,J,K02) and V(I,J,KI2)=BCTOP*V(I,J,K02). KI2 appears in the coding of the subroutine but has the same value as KB2 which appears in the illustration. The surface velocity is then established according to the summing of the vectors above and below the interface. There is no w-velocity defined here as a result of the non-flux condition which prevents the flow of material through a solid object. This, however, leads one to consider whether mass is conserved through the system when either a partial or nonslip surface is present. So long as the grid spacing is very small relative to the height of the computational domain, one can justify that the quantity of kinetic energy redirected upward in the form of a positive w-velocity is small and can be neglected. If this is not the case, it is possible

that LES-3d will underestimate the amount of fluid present, in so far as the volume of fluid in the virtual wall cell is effectively diminished when a negative velocity is imposed within the solid cell adjacent to the fluid.

The means of approaching other obstacle surfaces can be found in the subroutine VEL3D.

Next, the program scans the input file for information relevant to thermal effects, specifically temporal data referring to the amount of time that elapses before a wall or object reaches a preset temperature. Subsequently, thermal boundary conditions are established. This is done in a manner similar to that used to assign the velocity slip boundary conditions.

THERMAL BOUNDARY CONDITIONS

The LES3d modeling scheme makes allowances for adiabatic, isothermal, thermally thin, and thermally thick surfaces. The grid cells of object surfaces and walls receive code identifiers which activate the particular subroutines which perform the temperature updating protocols for each thermal surface type. Thermal gradients are applied across neighboring solid and gaseous grid cells on the basis of the thermal properties of the surface. The default thermal boundary condition is for adiabatic walls across which there are no thermal gradients between them and the fluid flowing past them. BCT, the governing parameter in this case, is set equal to 1. There is a redundancy in the code with regard to adiabatic walls. Surfaces with the local heat parameter QS, and wall temperature TMPW0 both set equal to zero also register as adiabatic. The above

values of these variables trigger the code to apply the adiabatic classification IBCDEF to these solid surface grid cells . Within the temperature fixing subroutine TMPBC of the LES3d program RHO3D.f, the gas cells adjacent to cells with the IBCDEF classification receive a temperature assignments according to the scheme TMP(II,JJ,KK) = BC*TMP(IIG,JJG,KKG). Here wall cell indices end with the letter "G", BC is a short hand expression of the thermal boundary condition BCT, and the local temperature is denoted by TMP.

Isothermal walls are identified as material surfaces by the characteristic parameters MHC = 1 and wall temperature TMPWAL set by the user in the input file. Here, the wall is considered an infinite heat source whose temperature does not diminish on account of heat transfer taking place at its surface. There is an option, however, wherein the user can set the wall to attain its assigned wall temperature after the passage of a certain amount of time. The time delay is factored into the temperature value measured at the wall by means of a scalar operation which takes into account the difference between the current time and the time when the wall is to attain its maximum temperature. With the temperature of the wall established, the energy convected off its surface is required to identify the temperature of the gas adjacent to the wall cell. The LES3d program uses a correlation for the convective heat transfer coefficient based on experimentation of heat transfer across the thermal boundary layer of hot surfaces in the presence of turbulent air flows [40], namely

$$\dot{q}_c'' = h\Delta T = C|\Delta T|^{1/3}\Delta T .$$

Alternatively, in a direct numerical simulation, the convective heat transfer would be expressed in terms of the temperature gradient at the gas-solid interface and the object's thermal conductivity k such that

$$\dot{q}_c'' = -k\frac{\partial T}{\partial t}\bigg|_{n=0}.$$

Where the rectilinear surface is horizontal with normal in either the positive or negative z direction, the heat transfer coefficient for the LES-3d isothermal simulation is given as C_HORIZONTAL = HCH*$|\Delta T|^{1/3}$ or 1.43 $|\Delta T|^{1/3}$. Vertical planes with normals in the x or y direction receive a convective heat transfer coefficient C_VERTICAL = HCV* $|\Delta T|^{1/3}$ or 0.95 $|\Delta T|^{1/3}$. The heat given off by the wall is a function of the difference in temperature DTMP between the maximum wall temperature TMPG and the fraction that may be experienced at the wall surface due to the time delay in heating TMPWAL. Therefore the expression for the heat convected to the surrounding gas cells from a horizontal plate, for example [39], is coded as QCON=HCH*DTMP*ABS(DTMP)**1/3. To recover the temperature of the gas from this expression, the heat convected is scaled by the inverse of the Reynolds and Prandtl numbers and multiplied by the characteristic length of the cell in the direction of the unit normal. In so doing, a characteristic temperature is recovered. This quantity is then subtracted from the wall temperature and the difference is assigned to the gas.

Conductive surfaces require a bit more manipulation to convert the boundary condition into a temperature condition across the solid wall and adjacent gas cells. First the temperature of the solid must be assessed as a function of time in the subroutine

WALCON. Then a temperature must be prescribed to the neighboring gas cells discussed in the previous cases in subroutine TMPBC. Thermally thin materials conduct heat on the basis of their density ρ and specific heat c. Such objects are considered to be of constant temperature throughout their width δ. Heat is transferred from the surface of these objects according to the relationship

$$\rho c \delta \frac{dT}{dt} = \dot{q}_c'' + \dot{q}_r'' - \dot{q}_e''$$

where the heat fluxes are attributed to convection, the radiative losses of burning particles, and thermal radiation [35]. For thermally thin solids, the user specifies the parameter C_DELTA_RHO, the product of the thermal properties of the surface in question. If C_DELTA_RHO (also expressed as CDR) has been specified, LES-3d sets the material heat capacity parameter MHC of the object surface to 2 and the material type to IFLSPR. Since, surfaces of the classification IFLSPR are frequently set to theoretically heat up and ignite during the simulation, this classification also triggers the areas of the program set to predict the dissipation of heat due to the incidence of water on these surfaces delivered by virtual sprinkler systems. As a result, the overall heat capacity of the object is computed as a function of evaporating water droplets on its surface. The surface temperature of thermally thin objects is therefore coded as a function of the heat fluxes through the front and back of the object (QCREF, QCREB), the modified heat capacity of the object CDRPW, and the amount of time that has elapsed. Thus, the wall cells (indexed by IW) with the boundary condition of thermally thin receive temperature assignments of the form

TMPW(1,IW) = TMPW(1,IW) + TTFAC*(QCREF+QCREB)/CDRPW

where the previous wall temperature setting is updated at each new time step of duration TTFAC [39]. After calculating the convection of heat off the thermally thin surface, a characteristic temperature due to convection is identified in the same manner as it was done in the isothermal case. This characteristic temperature is subtracted from the local wall temperature; the difference is prescribed to the gas cells adjacent to the wall.

To apply the thermally thick boundary condition, the user must specify of the thermal diffusivity ALPHA, the thermal conductivity KS, and the object thickness DELTA. When the thermally thick conditions has been specified, the program classifies the surface type as IFLSPR and the material parameter MHC is set equal to 3. The procedure for setting the surface temperatures of the wall derives from time dependent one-dimensional heat conduction calculations into the object where typically [35]

$$\rho c \frac{\partial T}{\partial t} = k \frac{\partial^2 T}{\partial n^2}$$

with the heat fluxes balanced by conduction of heat from the surface along the object face's unit normal

$$-k \left. \frac{\partial T}{\partial n} \right|_{n=0} = \dot{q}_c'' + \dot{q}_r'' - \dot{q}_e''.$$

After checking if a sprinkler has been activated, the wall temperature is established in the WALCON subroutine, as in the previous cases. The convective heat transfer between the solid and the adjacent gas particles is ascertained and a gas temperature is prescribed on the basis of the results.

SPECIES BOUNDARY CONDITIONS

Finally, species boundary conditions can also be prescribed. The no-flux criteria is set the same way the adiabatic temperature and free slip boundary conditions are prescribed. Since species are tallied at the centers of cells, for the no-flux condition to be realized, the concentration gradient must attain a zero value at the gas-wall interface. In order to do this, the wall cells' species count of zero is assigned to the adjacent gas cells. This no-flux criteria is coded as ZED(II,JJ,KK) = ZED(IIG,JJG,KKG) [39]. The species boundary conditions are set within the subroutine ZEDBC of program RHO3D.f.

A second species boundary condition is permitted within the scope of LES-3d's initial condition protocols. Species fractions can be applied to forced flow vents. The user sets the mass fraction MF of the species "N" at the desired vents; this triggers the program to apply the same value to the governing species boundary parameter BCZ which activates the ZEDBC subroutine. Since release rates can be specified for each chemical component present, the concentration of a species mass fraction at the vent is given as a function FZ of the initial concentration and the amount of time that has elapsed since the onset of the particle release. The presence of molecule N at the vent is coded as [39]

ZEDWAL=ZED0(N) + FZ(T,ITAUZ(IW,N),N)*(BCZ(IBC,N)-ZED0(N)).

The concentration of species in the gas at the solid interface is an average of the wall concentration ZED(IIG,JJG,KKG,N) and the forced flow concentration ZEDWAL. Thus at each new time step, the concentration of species adjacent to the solid surface is given as [39]

ZED(II,JJ,KK,N) = 2.*ZEDWAL-ZED(IIG,JJG,KKG,N).

OTHER INPUTS

After all the boundary conditions are set, things such as sprinkler locations, spray trajectories, thermocouple type and position are read into the code after velocity values are defined across the domain. Thermocouples are set to measure particular flow properties at fixed locations. These values are exported by the code to one file denoted by the suffix *.tc . At the termination of the simulation, these files can be opened into a spreadsheet to gage the variation of the parameters over the simulation time and perform any required statistical analysis. Once all of the initial conditions are set and every grid cell has been identified as part of a solid structure or an open space, the massive array structures are read into the computational portions of the program. As mentioned in the previous section, a second order central difference method is used to solve the spatial derivatives, and a predictor-corrector scheme updates the flow variables in time. Vector

CHAPTER 4

SIMPLIFIED DUCT STUDY

In this chapter, the computational domain is reduced to that of a straight duct in order to simplify the flow dynamics to gain better insights into LES-3d's treatment of user specified inputs. The pertinent input parameters identified in chapter 2 are revisited here. Beginning with the velocity profile applied to the flow, domain design as it pertains to the duct length required to establish a steady flow, and grid spacing are evaluated. The performance parameter utilized here is the degree to which the simulated flows generate profiles similar to that occurring in the actual wind tunnel.

INLET FLOW SPECIFICATION

As a result, a number of flow profiles have been preset within the code to simplify the user's task of setting parameters to resemble an experimental set up. The atmospheric profile is applicable to open flows where velocity varies with density and altitude. The top hat and parabolic flows are most often associated with channeled or closed flows. Tests were conducted to determine whether the experimental profile could be achieved using the closed flow top hat and parabolic profiles in the simulated straight duct test section of the University of Maryland wind tunnel. Demonstrating the applicability of top hat or parabolic profiles to the simulation alleviates the need to use numerical curve fits of real velocity data to describe the flow. Likewise, it serves as a means of establishing whether the experimental flow possesses characteristics of a laminar flow, or a post-transition turbulent flow.

Since mass and momentum must be conserved, it follows that an integral of the velocity profile over the inlet area should equal the volume flux leaving the channel. Setting the volume integrals of the different flow profiles equal to the volume flux permits definition of an "equivalent flow condition".

To perform the volume integral, an axisymmetric flow is assumed. As a result, the area traced out as the velocity profile crosses the inlet is assessed instead of the volume. In reality, since the flow moves through a square channel, an error is introduced because the additional fluid flow passing by the duct corners can not be accounted for with this method. This approximation is necessary because it is very difficult to obtain adequate velocity measurements at the corners of the duct. As a result, the experimental velocity is specified as a function of the two dimensional distribution at the plane of symmetry.

Top hat profile

Simulations were run to determine whether the preset profiles would develop through the computational field and take on a shape that more closely resembles the actual profile. Development of the top hat profile was examined in a straight constant cross section duct 0.9 m long x 0.09 m wide x 0.09 m tall. The grid spacing was held fixed at 32 units in the x-, y-, and z- directions for these preliminary tests. The contribution of slip was included in this study by observing differences in development when the fluid was exposed to free slip, partial slip, and nonslip walls. The cases studied are tabulated in Table 4.

flows have underdeveloped profiles. However, it is important to note that the vectors at the boundaries are longer than those of the nonslip case. This indicates how the partial slip effect does not completely inhibit transverse flow motion along the walls. Both the transverse velocity and the flow gradient are non-zero as expected according to the way the slip conditions are programmed in the code. Differences between the two simulations are more readily discerned upon comparing the contour plots.

Within the first 0.36 m of the duct, the straight edges of the partial slip contour plot's color bands suggest that the fluid moves more like a rigid body than a continuously deforming fluid. Since the flow is moving along the walls, the compensation needed to conserve momentum across the flow is not as extreme as in the previous nonslip case. The central core of the flow does not have to accelerate as rapidly to account for the frictional effects attributed to shear and the velocity gradient at the domain walls. Nonetheless, this is a temporary effect. The contours develop a convex shape 0.26 m down the length of the duct as the boundary layer develops and becomes more pronounced. In contrast to the cusp that forms in the nonslip contour plot, a nib appears at 0.64 m denoting the region where the boundary layer has grown to influence fluid dynamics at the center of the duct. The central core reaches a velocity only 25% that of the inlet velocity indicating that the nonslip flow develops more quickly than the partial slip.

In striking contrast to the above two flow simulations, the free slip case shows neither the stage-by-stage streamwise acceleration nor the boundary layer-profile enhancing effect of striation wherein horizontal flow layers of increasing speed are set up across the flow. Shown in Figure 16, the vectors across the flow domain are of uniform

length and orientation. The profile adheres to the top hat structure illustrating that the free slip requirement of $\frac{\partial u}{\partial z} = 0$ is upheld the entire length of the solid-fluid interface.

Regarding the contour plot in Figure 16, an oblong patch appears in the center of the flow as a result of the small scale mixing required to maintain the constant slope at the boundary layer. Some of the fluid at the core of the duct disperses to the wall region resulting in the slightly slower moving central region of the flow. The dark waving lines along the walls mark patches in the flow where the fluid accelerates and decelerates in an periodic fashion to equilibrate itself and maintain the wall velocity gradient after being injected into still air. The color bands differ by 1/200th of the original 1 m/s incident velocity indicating that the mixing is not significant enough of a phenomenon to upset the top hat profile which appears constant in the vector plot. In addition, the oscillations diminish when the flow has travelled 0.84 m and arrives at the open vent. The infinite resevoir at the exit absorbs the duct end pressure effects. One can confidently say that this flow does not develop because the centerline inlet velocity is equal to that at the exit.

Parabolic profile

The parabolic profile is specified in the subroutine CHKVNT of the program init3d.f within the LES-3d code. The equation of the parabola for the rectilinear grid network is

$$U = U_o * PY * PZ$$

layer below it. The profile and surface conditions are such that no further compensation is required of the flow to maintain momentum conservation across the duct.

When the parabolic flow is set to develop over partial slip surfaces, the flow does evolve somewhat. Indistinguishable on the vector plot, the evolution is clearly depicted in the contour plot of Figure 19 by virtue of the steadily decreasing width of the central contour. This central band diminishes to a point at 0.76 m illustrating that the flow slows to make up for the transverse motion along the walls of the domain. The parabolic profile, in essence, flattens and takes on its next evolved state much closer to the end of the duct.

As is the case with the free slip top hat flow, the free slip parabolic flow has little resemblance to the two other parabolic profiles. To maintain the velocity gradient at the walls, the initially parabolic flow disperses fluid to the duct edges. As illustrated in the vector plot of Figure 20, the overall effect of this distribution of fluid is to flatten the profile. Just within the entrance, the profile develops a bulge along the centerline of the duct, which persists, growing until it reaches the mid-length of the duct then shrinking as it approaches the exit. The growth and decline of the bulge follow the growth and decline of the oblong patch along the central region of the contour plot . The patch appears at 0.05 m and diminishes at 0.8 m which suggests that the profile is highly sensitive to the pressure changes that occur when the flow is introduced into an initially still flow or exhausts through an open vent. The centerline velocity declines from 1.5 m/s to 1.03 m/s at the exit indicating that compared to the other parabolic simulations, the free slip parabolic flow undergoes the greatest degree of development.

mm to the half-height of the duct stands in sharp contrast to the arching parabola and possibly has a greater resemblance to the flatter turbulent profile.

For comparison purposes, a theoretical fully developed turbulent profile is included in the figure. The equation for this curve is given by the power-law velocity profile which has been found to give reasonable approximations of turbulent flows. The equation of this fully developed theoretical flow is

$$U = \left(\frac{r}{R}\right)^{\frac{1}{n}}$$

where n=6 and is proportional to the Reynolds number [41]. The equation is given in terms of an axisymmetric flow domain which has been mapped to Cartesian coordinates for comparison purposes. The growth of the experimental boundary layer does not experience the fast and dramatic ramping of the velocity from 2-10 mm as is the case of the theoretical curve which attains 80% of the freestream velocity within 1/8 th the height of the duct. The simulated top hat flows and the experimental profile are all underdeveloped compared to this theoretical curve.

Defining the boundary layer as the region in the flow wherein the flow velocity approaches 99% of the freestream velocity [42], it can be shown that the experimental flow's boundary layer terminates at approximately 27 mm above the duct floor. The same regions in the simulated nonslip and partial slip flows grow to 19 mm. This indicates that the simulations develop slightly slower and have thinner boundary layers than the actual flow. In spite of the difference in growth rates, however, the LES top-hat partial slip curve exhibits the same velocity gradient and velocity values as the

experimental flow profile within its boundary layer. There exists only a slight divergence of the simulated profile between 15 – 30 mm. This divergence is attributed to differences in flow developedness and limitations in the data analysis technique. The data reduction technique prohibits the plotting of a smooth transition between the boundary layer and the freestream of the simulated data. Only discrete locations within the flow can be charted. The similarity between the profiles indicates that the partial slip top hat profile is the most appropriate choice for modeling the experimental flow with pre-set code profiles. Even if one assumes that the experimental flow will continue to develop through the test section of the experimental apparatus, the flexibility inherent in the coding of the slip condition would make it possible for the simulated partial slip flow to develop in tandem with the experimental flow. In this regard, the choice of the partial slip boundary condition over that of the fixed nonslip condition makes the partial slip top hat the better choice of the profiles to represent the experimental flow.

The free slip top hat and parabolic flow profiles, in contrast, would be the least appropriate choices for modeling the experimental flow given the absence of a boundary layer in the top hat case and the presence of an irregular bulge at the half-height of the parabolic profile.

FOCUS ON BOUNDARY CONDITIONS

It has been shown qualitatively, that the surface character assigned to the computational domain walls alters the development of the velocity profile. To get a

the boundary parameter is of a value between those specified for the nonslip and free slip conditions, the flow velocity gradients measured fall between the ranges established for those two surface conditions. At the duct entrance, as shown in the table, the gradient of the flow over partial slip surfaces measures 11 s-1 which is midway between the values of 9 s-1 and 14 s-1 established for the free and nonslip scenarios, respectively. Likewise, at the duct exit, the partial slip gradient measures 55 s-1, a value slightly larger than the average of the 7 s-1 and 79 s-1 gradients computed for the free and nonslip scenarios. The same holds true for the flow with pre-set parabolic profile. At the entrance, the gradients of the parabolic flows for all three slip conditions are within close proximity of one another at the entrance. By the duct exit, the partial slip scenario possesses a wall gradient of 41 s-1 which falls between the values measured for the free and nonslip cases.

As the parabolic flow travels the length of the duct, fluid disperses to the exterior walls such that the wall gradients become less steep -- the opposite is true for the top hat flows. In the nonslip case, the u=0 m/s requirement minimizes this phenomenon. The initial entrance gradient of 51 s-1 diminishes by only 5 s-1 to 46 s-1. In contrast, the parabolic flow travelling over free slip boundaries must continuously deform to maintain that slip condition. Momentum diffuses from the central core to such an extent that the gradual characteristic curve of the profile is lost. The 54 s-1 wall gradient gives way to one of 14 s-1 which compares to the entrance measurements made for the top hat flow gradients. The partial slip gradient at the duct exit falls between the values calculated for the parabolic nonslip and free slip cases, although it maintains a character closer to that of the nonslip flow than the free slip flow.

Regarding the experimental results, the 53 s-1 exit gradient within error is equal to that measured at the exit of the simulated top hat flow travelling over partial slip surfaces. The gradient quantification serves as a means of promoting, again, the top hat partial slip flow scenario as the most appropriate for modeling the real flow in a simulated domain.

DEVELOPING DISTANCE

Up to this point, boundary conditions and a pre-set flow profile have been identified which, when incorporated into the LES-3d mock-up, may give an appropriate representation of flow through the University of Maryland wind tunnel test facility. Although the previous test results are encouraging, there are no code parameters that permit the user to prescribe the developedness of the flow. As a result, the modeled inlet flow will evolve as a laminar flow which is not necessarily the case. By constructing an inlet to the simulated test section, it may be possible to engineer the flow to mimic the natural development of the wind tunnel air prior to its deposition into the sudden expansion. An inlet to the flow may also encourage turbulence, leading to a better prediction of the actual downstream velocities. Limiting factors on the inlet length are both the amount of additional computation time required to calculate the flow through the vestibule, and the constraints on the amount of random access memory available to LES-3d operations on the workstation. In order for the duct addition to be practical, its length must be as short as possible to minimize the computational time.

Flow development, therefore, was studied in long ducts to see whether the degree of developedness of the simulated flow could be altered. In theory, the development parameter entrance length (l_e), is governed by Reynolds number and surface roughness in addition to flow profile. Likewise, it is defined as the expanse of duct required for the developing boundary layers to grow from the duct walls to completely fill the channel [44]. At the point of intersection, the centerline flow velocity reaches a constant value.

It has been shown experimentally that the contribution of Reynolds number to developing distance becomes less pronounced as the Reynolds number becomes more turbulent. For laminar flows with Reynolds numbers less than 3000, the entrance length varies as $\frac{l_e}{D} = 0.06\,\mathrm{Re}$, where D refers to the characteristic height of the domain. For turbulent flows, this same parameter is proportional to $\frac{l_e}{D} = 4.4(\mathrm{Re})^{\frac{1}{6}}$, a fraction of the original Reynolds number [44]. To identify the degree of Reynolds number dependence on the entrance length of the simulated wind tunnel, two velocities were used. Top hat flows of 1 m/s and 5 m/s corresponding to Re=5,900 and 30,000 respectively, were simulated in ducts of 1.2 m, 1.8 m, 2.4 m, and 3.6 m. These flow speeds are representative of those used in the actual wind tunnel.

From the above turbulent entry length correlation, it is expected that the 1 m/s flow should develop over 1.7 m; the faster flow should reach maturity by 2.2 m. Experiments were simulated in partial slip and nonslip ducts in order to assess the contribution of surface roughness to the flow evolution. The study was limited to top hat flows since the similarity of these simulated flows to the experimental one has already been corroborated.

The outcome of these experiments is recorded graphically in Figure 22. Since a non-variable absolute velocity is never reached in these simulations, the developing distance is defined here as the point downstream of the entrance where the streamwise velocity gradient attains a constant zero value and its streamwise derivative becomes constant. Centerline exit velocities are reprinted in Table 7 below. Duct velocities are normalized by dividing out the inlet velocity. Table 8 and Figures 23-26 contain information about the selection of entry length on the basis of the streamwise velocity derivatives.

Table 7: Exit Velocity Values for 1 m/s and 5 m/s Flows through Ducts of Varying Length and Surface Roughness

Re = 5900; Uin = 1 m/s	Partial Slip	Nonslip		Re=30,000; Uin = 5 m/s	Partial Slip	Non Slip
Duct Length	Uexit/Uin	Uexit/Uin		Duct Length	Uexit/Uin	Uexit/Uin
0.9m	1.45	1.97		0.9m	1.20	1.47
1.2m	1.51	2.05		1.2m	1.24	1.43
1.8m	1.61	2.13		1.8m	1.29	1.37
2.4m	1.63	2.14		2.4m	1.25	1.37
3.6m	1.67	2.17		3.6m	1.20	1.38

Table 8: Entry Lengths calculated for 1 m/s and 5 m/s flows on the basis of streamwise flow gradients

		Non Slip	Partial Slip	Theoretical
Re = 5900 Uin = 1 m/s	$\Delta u/\Delta x=0$	1.7 m	2.5 m	1.7 m
	$\frac{\Delta(\Delta u/\Delta x)}{\Delta x} = C$	1.7 m	2.5 m	N.A.

		Non Slip	Partial Slip	Theoretical
Re = 30,000 Uin = 5 m/s	$\Delta u/\Delta x=0$	2.2 m	2.0 m	2.2 m
	$\frac{\Delta(\Delta u/\Delta x)}{\Delta x} = C$	2.4 m	3.0 m	N.A.

In the 1 m/s case, normalized centerline exit velocities increase and then approach a plateau as the duct length is extended from 0.9 m to 3.6 m. The plateau demarcating the developing distance for the Re=5,900 flows occurs around 2 m in both the nonslip and partial slip cases. Figure 24a illustrates that as the flow travels down the partial slip ducts of increasing length, the variation in velocity with position diminishes to a zero gradient at 2.5 m. In the nonslip case shown in Figure 23a, the zero gradient occurs earlier at 1.7 m. These values agree with analysis of the second derivatives of the velocity shown in Figures 24b and 23b.

Returning to Figure 22, just short of the 2.5 m mark, the centerline velocities for the 1 m/s flow through the 2.4 m and the 3.6 m ducts are identical in the nonslip case. There is a slight but noticeable difference between velocities at the same point in the partial slip case. The implication of this is that the flow with partial slip boundary conditions continues to develop slightly beyond the point where the nonslip case becomes fully developed. This discrepancy in conjunction with the streamwise flow gradient data concludes that boundary conditions do impact the developing distance. The nonslip flow leaves the duct faster and matures earlier than the partial slip flow. It is also interesting to note here that the nonslip flow matures at the sight predicted by the turbulent entry length correlation cited above.

We look to see where the second derivative of the velocity in the streamwise direction reaches a constant zero value in response to the results collected from probing of the centerline velocity in the experimental apparatus. Shown in Figure 27, a flow of 1 m/s stays fairly constant and does not exhibit any sort of radical decay. It follows that one would look for the point in the duct where the first derivative equals zero and the

second takes on a constant value, zero in this case. This velocity assessment was made by utilizing a pitot tube and taking 144 pressure measurements at each position along the duct. Nonetheless, since a perfect system can not be simulated, the first and second derivative curves are found to experience a degree of vacillation around the point of convergence as a result of pressure effects at the duct exit. This is especially true in the 5 m/s partial slip case.

The 5 m/s partial slip flow velocities rise and plateau at roughly 2 m. The streamwise gradient of the flow hits the abscissa at this same point, however, it does not attain a fixed zero value after crossing the axis. Rather, it continues to get smaller suggesting that the flow continues to evolve. According to Figure 26, it appears as though the gradient would take on a zero gradient if the inlet were extended beyond 3.6 meters in so far as the curve turns upward at that point. The derivative of the streamwise velocity gradient does not attain a fixed value either. It grows steadily after an initial period of oscillation crossing the x axis at 3 m. The two values do not agree with one another as was the case in the 1 m/s flow scenarios. It is believed that the pressure perturbations are not fully surpressed with this LES configuration and thus are mirrored back into the duct as flow speeds increase. This may be why the anomaly appears for the faster flow.

In the nonslip case, displayed in Figure 25, the first and second derivatives of the streamwise velocity behave as those recorded for the slower flow. The first derivative of the streamwise flow becomes zero at 2.2 meters; the second derivative attains a zero value at 2.4 m -- although as in the partial slip case, it does not stay fixed at zero after crossing the axis and does not agree exactly with the value attained for the first

derivative. The centerline velocities for the nonslip flow rise and fall back to a plateau in the vicinity of the points where the derivatives take on zero values.

The theoretical entry length correlation states that for Re=30,000, the developing distance should be 2.2 m. Again, the theoretical results for this parameter agree with the nonslip values. This indicates that the LES-3d program is simulating the flows as turbulent regardless of the fact that the flow profiles are underdeveloped.

Likewise, one can also state that the velocity values of the partial slip flows are slower than those of the nonslip flows because the shear layer is concentrated closer to the wall. With the velocity strongly decreased next to the wall, the flow begins to accelerate towards the centerline. This leads to a reduction of the local centerline velocity as a result of the mixing of adjacent shear layers. In order to guarantee mass conservation, this viscous effect necessarily slows the movement of fluid packets further downstream resulting in a flow slower than the nonslip flow.

There are some striking peculiarities apparent in these results; primarily, the abnormally large magnitudes of Uexit/Uin for the Re=5,900 flows as seen in Table 7. That the exit velocities of the nonslip flow exceed the inlet velocity by more than a factor of two, suggests the profile of the flow evolves from a top hat to something severely distorted in order for mass to be conserved across the domain. There is no indication of a excessively turbulent or vortex shedding flow depicted in the vector or contour plots for either the 0.9 m or 3.6 m duct flows in Figures 14 and 28. Velocity measurements taken at the duct inlet, the test section length, and the exit of the longest duct are illustrated in Figure 29.

Velocity is plotted against the number of grid cell spacings in Figure 30. Here, the recorded average centerline exit velocities decrease with increasing units. With a grid of 8 units, the average centerline velocity is over 2 m/s, a value already declared as grossly in excess since it implies that mass is not conserved. As the number of units increases to 64, the decline is parabolic. Beyond 80 units, the velocities diminish linearly approaching the original inlet speed of 1 m/s as the grid count increases to 336. A discontinuity in the trend is apparent between 64 and 80 cells. Since, the development of a boundary layer requires the centerline speed accelerate, one can readily dismiss the grid counts that yield the smaller velocities.

Each of these run scenarios has a characteristic velocity profile illustrated in the following contour and vector plots. Beginning with Figure 31, the contour plot features a number of development stages before the boundary layers merge 0.64 m downstream and contribute to an exit velocity of 1.81 m/s. The vector profile illustrates that the top hat begins to give way to a developed profile. The central vectors are much longer than those of the initial top hat. In contrast, Figure 32 with 48 grid cells in the z direction does not reach a stage of full development. Rather, the development is prolonged as depicted by the persisting color bands with strongly concave leading edges. The boundary layer here measures 0.02 m. The vector profile shows a clear evolution from the top hat profile to a turbulent one which takes on a bowed shape by the end of the duct. In Figure 33 severe irregularities begin to appear. At 0.36 m the graphics program translates the velocity data into a contour which is severely distorted as the flow makes a transition to its next stage of development. The gradations in velocity are too small to be discernible from the vector plot. Here, the boundary layer thickness is 0.01 m. Finally in Figure 34,

the flow goes through no stages of development. The profile remains underdeveloped except for the slight suggestion of a boundary layer 0.006 m thick. What is seen in this sequence of figures is the definition of an exceedingly viscous fluid as the number of grid cells increases. The flow goes through fewer stages of transition and takes longer to develop its mature profile.

So what grid size does one select at this point? The count that yields the average of the exit velocity extremes recorded on the plot? The number where the discontinuity appears? There is very little surety to be had in selecting a grid size by guessing. Since the LES-3d code can be run alternatively in a direct numerical simulation mode, the grid size selection experiments were repeated to see if a fixed exit velocity could by identified. It is well understood that large eddy simulations implement a correlation to calculate viscosity. For this reason, many researchers seeking to control viscosity contributions to vorticity have resorted to direct numerical simulations to model flows since viscosity is calculated directly from the flow Reynolds number [22].

For the LES-3d code running in direct numerical simulation mode, Reynolds number is defined as

$$\mathrm{Re} = \frac{\sqrt{gH} \cdot H}{\upsilon}$$

where H is the height of the flow domain, g is gravitational acceleration, and ν is the kinematic viscosity. The LES-3d manual [38] indicates that the minimum number of grid cells in the z direction needed to simulate this flow with a DNS approach is given by

$$KBAR^2 > \frac{U_{in}\,\mathrm{Re}}{3\sqrt{gH}}.$$

According to these definitions, Re=5355 and KBAR must be greater than 45. The assumption behind this correlation is that grid independence is achieved for values of KBAR greater than 45. Simulations were run for grid spacings of 16, 32, 45, 67,and 90 units. The average exit velocities of each run are plotted in Figure 35. Again, the top hat 1 m/s nonslip flow was prescribed for the domain with fixed x- and y- grid spacing.

When the flow problem is specified as a direct numerical simulation, the exit velocities increase linearly with increasing grid cells in the critical z-direction. The expectation was that with KBAR greater than 45, a plateau in exit velocities would be reached. This velocity value would support the criteria for selecting the number of cells appropriate for the flow scenario. And, it would "calibrate" the large eddy formulation of the problem: the grid cell count would be fixed to yield the DNS-established exit velocity. However, grid independence of velocity is never met across the range of units investigated. Grid independence requires that beyond a critical number of z-direction refinements, the average exit velocity recorded must be invariant for all successive grid refinements. Only in this way can a modeler be certain that the grid size selected is of the appropriate sensitivity for the flow condition modeled.

Simulations were not executed for grid cell spacings greater than 90 units, because the formulation disintegrates with continued refinements of the grid. Illustrated in Figure 36, as the grid spacing increases, an anomalous concave color band characterized by two discontinuous velocity spikes appears at the duct exit. The band

and its spikes grow in size as the number of grid cells increases as seen in Figure 37. This type of phenomenon can not be supported in nature, and thus its appearance serves as an illustration of the break down of the equation solver's capacity with this formulation of the flow domain. Figures 38 and 39 show that as the number of grid spaces increases from 16 to 45, it takes a greater expanse of pipe for the flow to develop. In the first graphic, the convex color bands give rise to a nib at 0.58 m. It was stated earlier that this feature is an exaggeration of the changes that take place at a particular stage of the flow development where the boundary layers are "visible" to the central core of the flow. Where the grid count is 45 units as in Figure 38, this nib does not appear; rather, the convex color bands persist. The implication here is that the flow goes through a greater number of stages in which the centerline flow accelerates to accommodate the initial growth the boundary layer. The boundary layer thickness is 0.015 m here. The boundary layer measures 0.03 m in the 16 unit contour plot.

The profiles of the DNS runs with maximum and minimum grid count are shown in Figure 40 along with the "standard" 45 cell run formulation. Each profile indicates a similar degrees of early development. The top hat has begun to give way to establish a profile with a nascent boundary layer. As the grid count increases, the central portion of the flow moves with greater speed. Nonetheless, the standard case is strangely underdeveloped compared to the runs with greater and lesser grid cells. With regard to the initial top hat 1 m/s flow, additional mass flux is generated in proportion to the number of grid cells specified for the run. It is clear that the problem as currently formulated is incorrect since a constant velocity measurement is not secured for the direct numerical simulations. Likewise, it is difficult to accept that the DNS simulations here

may be useful for calibrating the LES simulation. Before abandoning the utility of the DNS simulation, an attempt was made to alter the aspect ratio of the cells such that they would be square rather than rectangular. The grid count of 45 cells in the z direction, was maintained and the number of grid cells in the x direction was increased to 450 and 45 in the y direction. Limitations in the computer capacity of the DEC ALPHA prohibited execution of this simulation. A substitute simulation with 320,32,32 cells was executed. The profile of this run is included in the Figure 40. It is interesting to note that despite the increased number of grid cells, the centerline velocity across the duct exit cross section is only 68% of the last run with (32,16,90) units. The more refined DNS simulation is surprisingly closer in shape and magnitude to the least defined simulation of (32,16,16) units.

Contour and vector plots of the highly refined DNS simulation appear in Figure 41. The degree of detail in the contour plot is striking, one can see how the central region of the top hat flow accelerates dragging adjacent flow with it subsequently motivating the formation of the boundary layers. The wall layers join at 0.8 m. Downstream of this point, the flow is uniform, the maximum centerline flow speed is 1.14 m/s. The vector plot shows a rounding of the edges with a form very similar to the experimental flow.

The idea of increasing the order of magnitude of the x grid cell count to generate square computational volumes was incorporated into LES simulations of the same duct flow. The (320,32,32) grid in addition to courser and finer grids of (240,24,24) and (400,40,40) were utilized. Profiles of these runs are shown along with the courser LES simulations mentioned previously. Figure 42 illustrates a much wider range of development here than in the DNS simulations. An overdeveloped triangular profile

materializes for the 16 unit profile. The mid-range 48 unit formulation yields a profile similar to the DNS curves. The (32,16,336) unit formulation undergoes the smallest degree of development and is almost identical to the original 1 m/s top hat flow introduced into the duct. Curiously, the LES simulations with highly refined grids yield profiles which are much closer to one another in shape and exit velocity, than those with grid cells held fixed in the x and y directions. The overlap with profile (32,16,48) and the nearness of curve (320,32,32) suggest grid independence is achieved for the (400,40,40) simulation: the 1.22 m/s exit velocity of an earlier refinement has been reproduced; and the results from the previous run agree within 0.03 m/s. A look at the contour and vector plots for this grid independent flow shows that the fluid reaches its fully developed state at 0.6 m where the boundary layers merge. The vector diagram depicts a bowed fully develop flow which is very similar to the experimental profile illustrated in Figure 21. These are very encouraging results, however, the validity of the simulation process is called into question given the extensive differences between the DNS and LES contour plots for supposedly the same flow. Without a visual record of experimental flow's development, one can not determine which simulation is the more realistic. The DNS flow illustrates the formation of a cusp in the flow resulting from the nonslip condition along the wall. As the boundary layers approach each other, the cusp is drawn downstream into a cone, the vertex of which depicts the point where the flow become fully developed – 0.8 m downstream. The LES flow with the same grid refinement has a less severe demarcation of the transition to fully developed flow as shown in Figure 43. The central core of the top hat takes on a practically parabolic form almost immediately. This form degenerates as a result of strain at the flow's leading edge. The initial

boundary layers merge at 0.4 m and a fully developed flow with velocity 1.25 m/s occurs 0.5 m from the inlet.

SUMMARY OF FINDINGS

An extensive set of simulations has been run to identify the crucial flow and code-wise parameters governing the behavior of the fluid through the virtual geometry of the rearward facing step. From profile to grid spacing, each parameter has been manipulated to gain insight into which user-specified values yield flow dynamics similar to those observed in the University of Maryland wind tunnel. Likewise, the theory and code conventions were scrutinized to come to terms with the origins of some of the fictitious results recovered during the data analysis process. Each parameter was addressed individually with the hope that the optimal settings for each parameter might constructively interact to generate the most accurate results possible using the January 1998 version of the code.

Focusing on constructing a flow domain that would yield a fully developed flow at the entrance to the test section, it was decided that an entry length to the initial computational domain design was necessary. Coordination of surface boundary conditions and the flow profile suggested that a top hat flow travelling over partial slip surfaces would generate a flow that exhibited the same behavior as the experimental flow in the boundary layer. The development at the boundary has a significant impact on the downstream dynamics of the flow and the recirculation pattern, the critical feature that is being modeled here. Thus, additional simulations were conducted that demonstrated that

the test section inlet would have to be a minimum of 2.5 m to generate a stable fully developed turbulent flow.

Satisfied that these conditions would yield reliable data, the computational factor of grid spacing was addressed. To reiterate, LES-3d solves the Navier-Stokes equations across each cell. Scalar properties are evaluated at the edges of the grid cell, vector quantities at the center. Likewise, boundary conditions are affected within one cells width from the solid-fluid interface. The most important factor regarding cell size; however, is whether grid independence is achieved for the user-defined mesh refinement coded into the input file. It was found that grid cells with nearly a 1:1:1 length-wise aspect ratio elicited better results than rectangular ones. When the grid was refined to 400 x 40 x 40 computational units for a 0.9 m x 0.09 m x 0.09 m duct, grid independence was achieved: velocity outcomes converged with further miniaturization of the cells. Thus the ideal relationship between physical and computational dimensions was defined.

A final simulation was run to see how the individually optimized parameters synergize. The results of the findings are detailed below.

CHAPTER 5

LES-3D OUTCOMES WITH THE SPECIFICATION OF A HIGHLY DEFINED COMPUTATIONAL DOMAIN

With the optimization detailed above, the simulation of two minutes of flow through a wind tunnel with 2.5 m inlet and 0.057 m step required 1511 cells in the z direction, 40 in the y direction, and 65 in z direction. Specifying these conditions on the DEC ALPHA, though, proved impossible given the limits on the virtual memory and disk storage capacity. Likewise, LES-3d does not expect cell counts greater than 3 digits. This factor alone produced multiple memory allocation errors which inevitably led to the program crashing. The finest definable grid which best respected the 1:1:1 aspect ratio for the individual cells measured 800 units in the x direction, 24 units in the y direction, and 34 in the z direction. To compensate for the loss of flow field definition , the values of IBAR, JBAR, and KBAR were chosen to adhere as closely as possible to the $2^l3^m5^n$ scheme which is said to optimize the performance of the code's differential equation Poisson solver [38]. With this formulation, 212 x-direction grid cells are utilized to resolve the flow dynamics in the test section. Simulations were run for 120 seconds. Contour and vector plots of the simulation can be found in Figures 44-46. This test scenario will be referred to as the refined case.

VELOCITY PROFILES

Figure 44 features the time averaged contour plot of the inlet to the test section. With the velocity range divided into 100 discrete intervals, it becomes evident that the flow over the partial slip surfaces achieves its fully developed form at –1.8 m. Velocity measurements are taken at 0.002 m and 0.01 m above the duct floor at the inlet entrance and at the drop into the test section to examine the degree of flow deformation taking place within the inlet. At the entrance of the duct, the wall gradient is 42 s-1. The strain on the flow however increases to 49 s-1 by the end of the inlet. Table 9 contains the results from earlier data analysis of a simulated partial slip duct and the experimental test section, neither of which contains a step.

Table 9: Wall Velocity Gradient Examination for Experimental and Simulated Partial Slip Flows

	Experimental	Partial Slip Duct		Refined Partial Slip Duct with Step	
		Inlet	Exit	Inlet	Exit
Velocity @ 0.01 m [m/s]	0.95	0.98	0.95	0.99	1.11
Velocity @ 0.002 m [m/s]	0.52	0.89	0.51	0.65	0.72
Gradient [s-1]	53	11	55	42	49
(min,max) [s-1]	51,56	9,14	53,58	40,44	46,51
Grid Resolution		(32,32,32)		(800,24,34)	

These results demonstrate that the actual flow experiences a degree of strain that is in greater agreement with that observed in the lesser resolved partial slip duct as opposed to

the refined duct with step. Each grid cell in the refined case is approximately 0.004 m, thus a velocity change of 0.39 m/s is experienced over an expanse of two grid cells just before the test section, yet this is does not compare to the 53 s-1 wall gradient observed experimentally. From the inlet to the test section, the wall gradient is fairly constant in the refined case, increasing only slightly from 42 s-1 to 49 s-1. Thus, it can be said that as the cell size is reduced, the flow loses some of its fluidity. The flow moves like a rigid body in contrast to the pre-set partial slip boundary condition that has already been demonstrated to permit the flow to deform continuously across a courser grid. Figure 45 further illustrates this point. The experimental and theoretical turbulent flow profiles; the profiles of the simulated flows through partial and nonslip constant cross section ducts; and the profile of the simulated flow through the refined partial slip duct with 57 mm step are shown here. Again, it is evident that the refined partial slip profile differs significantly from the experimental. The most striking divergence from the experimental flow is the rapid jump in velocity that occurs within 4 mm of the duct floor. This feature is one of the signatures of a turbulent fully developed flow. Nonetheless, the simulation attains its peak velocity almost immediately and does not possess the gentle slope of the theoretical profile that indicates the merging of the boundary layers at the center of the duct. Paradoxically, this implies that the fully evolved profile of the refined case is strangely underdeveloped. The experimental profile is also underdeveloped, but it has a much rounder form within the vicinity of the wall, and it experiences a greater degree of deformation as it travels the length of the duct. Clearly, the attempt to implement a condition that would permit maximum deformation of the flow has been compromised with the specification of a highly resolved computational domain. It is not worthwhile to

experiment with a nonslip configuration for this simulation. As the grid refinement becomes greater, the slip condition is affected over an even smaller fraction of the flow. It is highly probable that the definition selected for the flow domain in this simulation is approaching the limit where partial and nonslip flows resemble one another. It is quite unfortunate that the partial slip profile that seemed to exactly follow the curve of the experimental profile was arrived at by accident and has not been reproduced with this current rigorously planned simulation.

Figure 46 features contour and vector plots of the test section. The 1.1 m/s flow entering the test section has a very blunt profile in contrast to the flows presented earlier. The 34 cm recirculation zone, however, is smaller than that measured for earlier simulations with the same mass flow specified at the inlet. The structure also differs from those simulations discussed earlier.

Table 10: Comparison of Recirculation Zone Lengths for 1 m/s flows

Velocity Profile	Slip Condition	Inlet Length [m]	Le [cm]	U supplied [m/s]	Centerline Inlet Velocity [m/s]	Grid Spacing
Top Hat *Pt2_1020.data*	Partial Slip	-2.5	34	1	1.11	800,24,34 *refined*
Top Hat *Step1gL2.data*	Nonslip	-0.9	41	1	1.3	234,9,18
Top Hat *Step1gL.data*	Partial Slip	-0.9	43	1	1.13	234,9,18
Top Hat *gL2v_888.data*	Nonslip	-0.9	46	0.89 m/s	1.1 m/s	234,9,18

The recirculation zone core is not anchored behind the step. Rather it is displaced downstream and features a laterally oscillating tightly coiled spiral feature. Only the top hat flow that was prohibited from developing due to the absence of an inlet exhibited the same spiral structure in Figure 2. For comparison purposes, the 1 m/s flow through the

computational domain that served as the template for the analysis of recirculation zone length and Reynolds number dependence is featured in Figure 47.

ENTRAINMENT RATES

Although the recirculation zone length is much closer to that measured experimentally, it is difficult to determine whether this refined case is an improvement over previous simulations when the flow wall gradient and profile are so divergent from the experimental ones. Nonetheless, keeping with the fact that the recirculation zone length and possibly the mass flux behind the step are approaching their true values as the cell size approaches that required for grid independence, the related parameter of entrainment was investigated. Time averaged profiles of the flow at various positions downstream of the step were produced and integrated to determine the amount of mass flux moving backwards through the recirculation zone as illustrated in Figure 48. This data is included in Figure 49 along with the entrainment rates for the 0.89 m/s flow through the nonslip flow domain which served as the template for determining the relationship between recirculation zone length and Reynolds number. A nonslip step was incorporated into the partial slip domain of this earlier assessment. It was believed that a platform over which the flow could evolve quickly would eliminate some of the transient development effects that could perturb the recirculation zone.

The maximum entrainment rate of 3.83×10^{-4} kg/s measured for the refined case occurs in the same place, 0.2 m downstream of the step, as the maximum for the earlier simulation. From this result, it can be concluded qualitatively that in spite of the other

disparities between previous simulations the location of maximum entrainment remains fixed irregardless of the refinement of the grid or the length of the test section inlet. Nonetheless, the magnitudes of the entrainment maxima differ by nearly a factor of three.

Finally, flow stability was assessed with the vehicle of the fast Fourier transform of the velocity traces. In the vector plot, the recirculation zone appears to be oscillating some what. The transform of the velocity, however, does not indicate that the flow pulses with a particular natural frequency. As mentioned earlier, the signature of resonance would be a peak that stands in stark relief against the noise of the signal. The largest peak appears within the noise of the signal at 11 Hz. All this indicates is that the frequency peaks are attributable to the gross large eddy motion of the flow and do not bear witness to higher frequencies of oscillation that would indicate vortex shedding of the turbulent flow. The oscillating feature in the vector plot may be an anomaly occasioned by the time averaging of the velocity trace. Nonetheless, this finding is consistent with earlier stability assessments that similarly predicted a stable flow. Velocity traces and the Fourier transform of the curve are included in Figures 50 and Figure 51, respectively.

ASSESSMENT OF THE REFINED PROFILE

The intent of this portion of the study was to take advantage of the findings of earlier simulations. The optimal settings for user-defined parameters that included flow profile, entry length, grid refinement of the computational domain, and wall boundary conditions were determined by executing small scale experimental simulations on a

simplified version of the wind tunnel to determine the manner in which the modeling routine within LES-3d addressed each parameter. The top hat flow profile exposed to partial slip surfaces was deemed the most appropriate profile for the final simulation because the behavior of the top hat within the vicinity of the wall was the same as that observed for the experimental flow. The upstream boundary layer dynamics play a strong role in governing the form the profile will take downstream of the step. Thus, if the upstream boundary phenomenon could be recreated numerically, the assumption was that the recirculation zone and downstream fluid dynamics would resemble the experimental flow beyond the step. Inherent within this assumption is the belief that the simulated fluid would continue to mimic the natural deformation of the tunnel fluid. Finally, with the computational grid across which the modified Navier-Stokes equations are solved set as close as possible to that required for invariance in the results, it was intended that the compilation of the results would yield the most accurate representation of the closed flow dynamics taking place in the experimental facility.

This final data analysis demonstrated that this was not necessarily the case. Improvements in one area of the simulation did not necessarily occasion an overall improvement in the results produced. Specifically, the grid cell size incorporated to elicit grid independence added an unforeseen stiffness to the flow. With upstream flow dynamics having a pronounced effect on the downstream phenomenon, it is unfortunate that the requirements for a mathematically sound simulation compromised the similarity measured previously between the experimental and simulated flows at the wall. Stability and the location of maximum flow entrainment were not altered with the amendments made to the computational domain.

CONCLUSIONS

The results of the numerical investigation have demonstrated that the configuration of a wind tunnel with rearward facing step is indeed a worst-case scenario wherein the flow pattern behind the step is stable and sufficient to harbor a robust and resilient flame. A numerical analysis of the flow scenario using the software LES-3d revealed the extent to which user-specified initial conditions affect not only the modeled flow's structure, but also one another to complicate the matter of simulating a flow that resembles that which occurs naturally.

Surface slip boundary conditions were found to affect the recovered recirculation length measurements and the rate at which the virtual flow develops through the simulated tunnel. As expected, flows developing over nonslip surfaces matured faster than those travelling over partial or free slip surfaces. This was facilitated within LES-3d by the assignment of a fictitious velocity within the "solid" computational cell of the underlying surface.

The inlet, however, was found to serve as an effective tool to induce the pre-set flow profiles to take on a form similar to the experimental profile. Permitting natural development of the profile also encouraged the development of turbulence which improved the degree of similarity between the modeled and real flows in addition to guaranteeing that a steady flow was entering the test section.

The code-specific parameter of grid resolution was also examined. When grid independence was specified the continuously deforming nature of the simulated fluid was compromised. Grid independence is important because it represents the point wherein

the computational domain has been appropriately resolved to address the critical length scales of motion of the flow problem. The LES-3d guide makes note of a particular correlation required for proper resolution of a DNS scenario which is not intuitive. Yet, only by virtue of trial and error can the appropriate grid sensitivity be verified for the LES simulation. As seen here, the exit velocities measured with the properly scaled DNS do not automatically define the sensitivity appropriate for the LES of the same flow scenario.

The effort put forward here has led to improvements in the design of the experimental structure in so far as where to position the combustion source to guarantee that the airflow to the fuel was maximized. Further study into the manner in which parameters vary as a function of grid resolution -- specifically with regard to the code's calculations of viscosity and vorticity – must be performed before the LES-3d code can be validated and accurately applied by an end-user to a combustion scenario. It is highly probable that the only means to validate the code's experiment-reproducing facility is by executing multiple test simulations to first identify the critical parameters both physical and computational governing the virtual flow. Subsequently, these factors must be optimizing en masse. Parametric improvements discovered, in short, must be incorporated into the next series of optimizing experiments. This type of approach, like the approach described above indicate that the large eddy simulating software can not be blindly applied to a flow problem with the expectation that one will exactly reproduce the experimental flow. The flexibility permitted by this software does, however, permit one to observe the general trends in the flow dynamics independent of the specificity required for a mathematically ideal simulation.

The source code for LES-3d can be accessed from the National Institute of Standards and Technology FTP site, ftp.nist.gov[39].

FIGURES

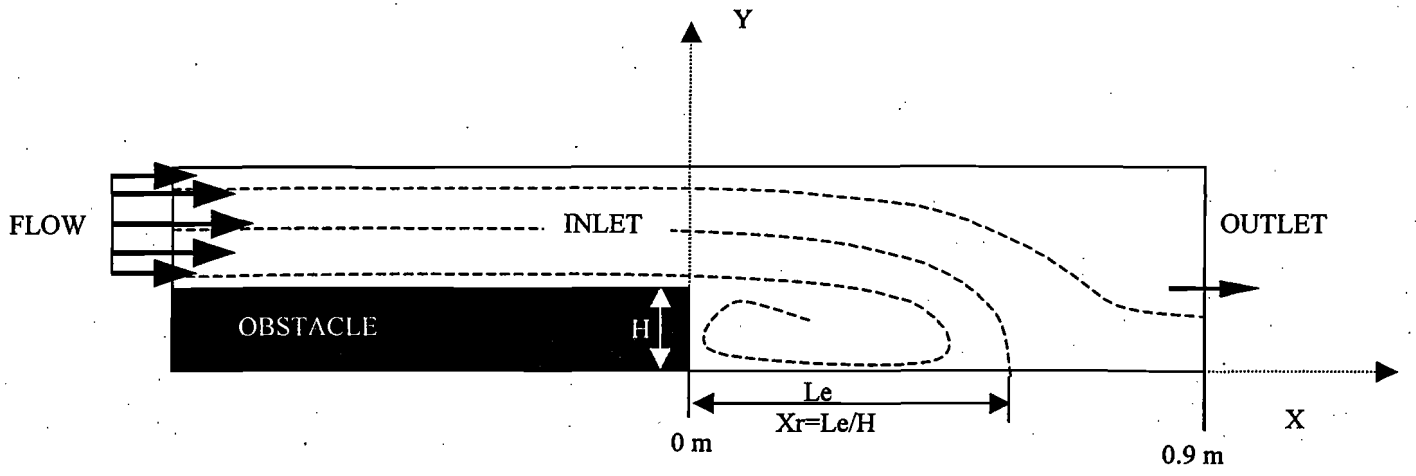

Figure 1: Schematic of the computational domain of the simulated University of Maryland wind tunnel

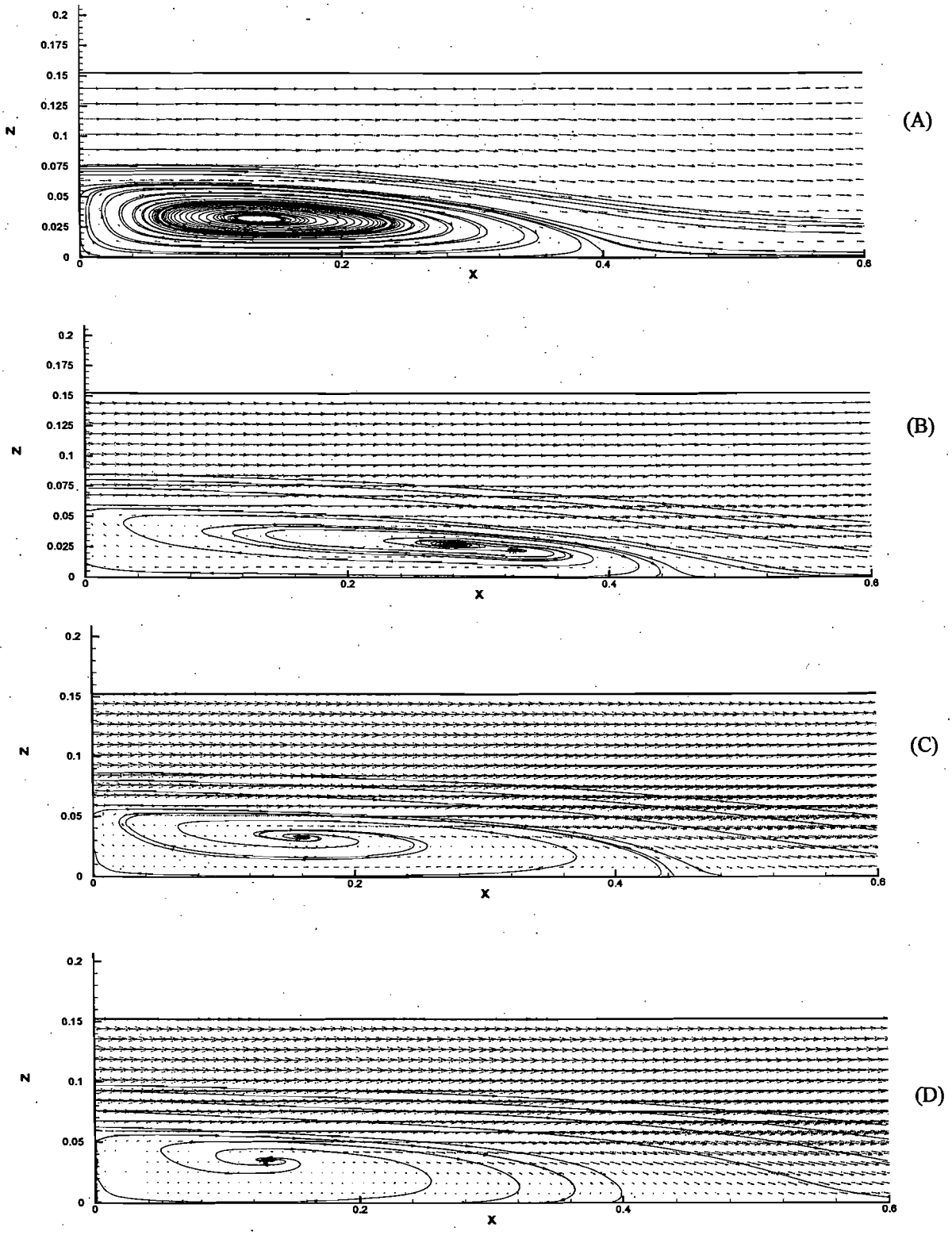

Figure 2: Average recirculation zone streamlines and velocity fields for a characteristic velocity of 1 m/s. For all cases an initial constant velocity Top Hat profile was specified. A) Partial slip boundaries, velocity applied at x=0, B) Partial slip boundaries, velocity applied at x= -0.25m, C) Partial slip boundaries, velocity applied at x=-0.9m, D) Non-slip boundaries, velocity applied to x=-0.9m.

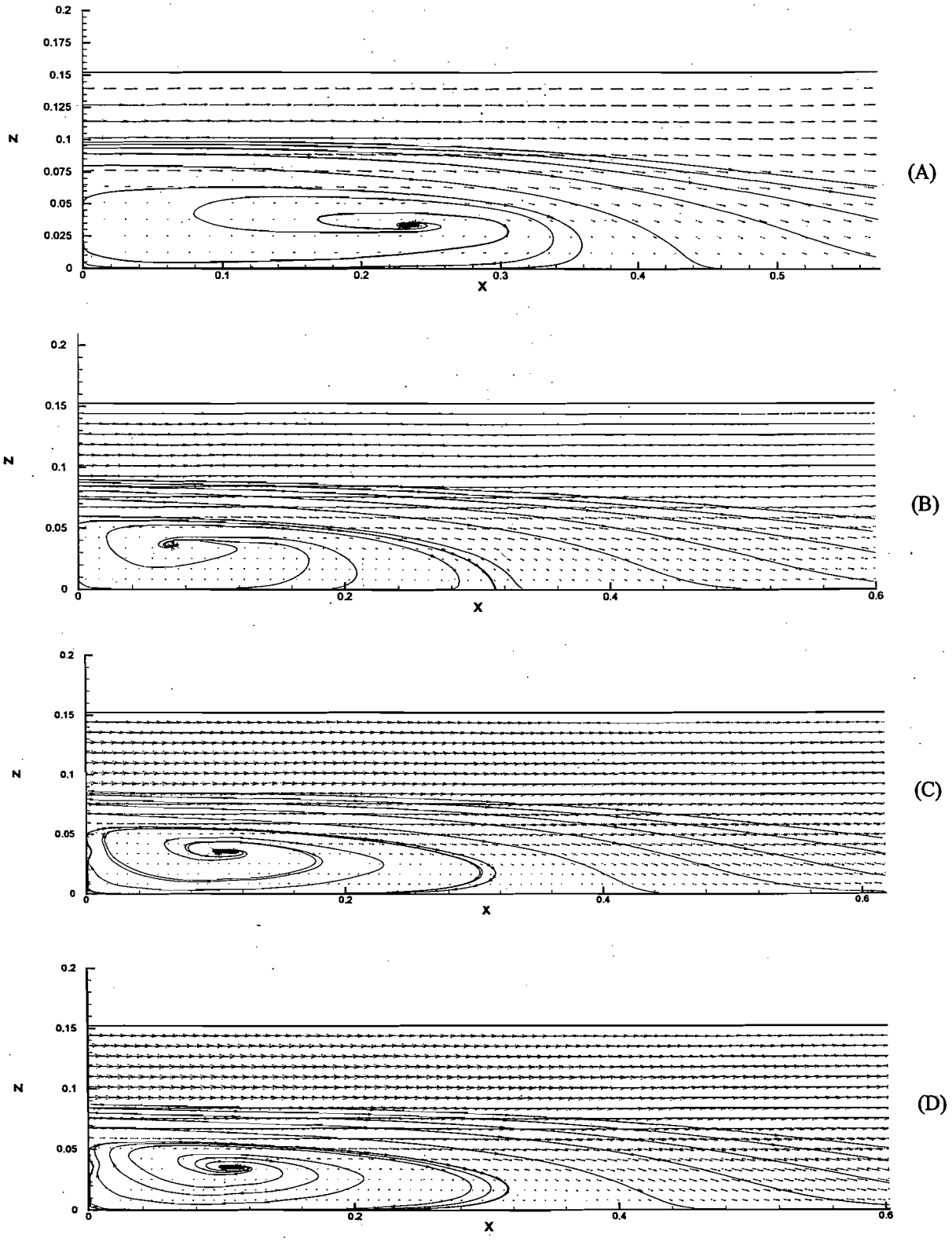

Figure 3: Average recirculation zone streamlines and velocity fields for a characteristic velocity of 1.5 m/s. For all cases an initial parabolic profile was specified. A) Partial slip boundary conditions, velocity applied at x=0, B) Partial slip boundaries, velocity applied at x=-0.25m, C) Partial slip boundaries, velocity applied at x=-0.9m, D) Non-slip boundaries, velocity applied at x=-0.9m.

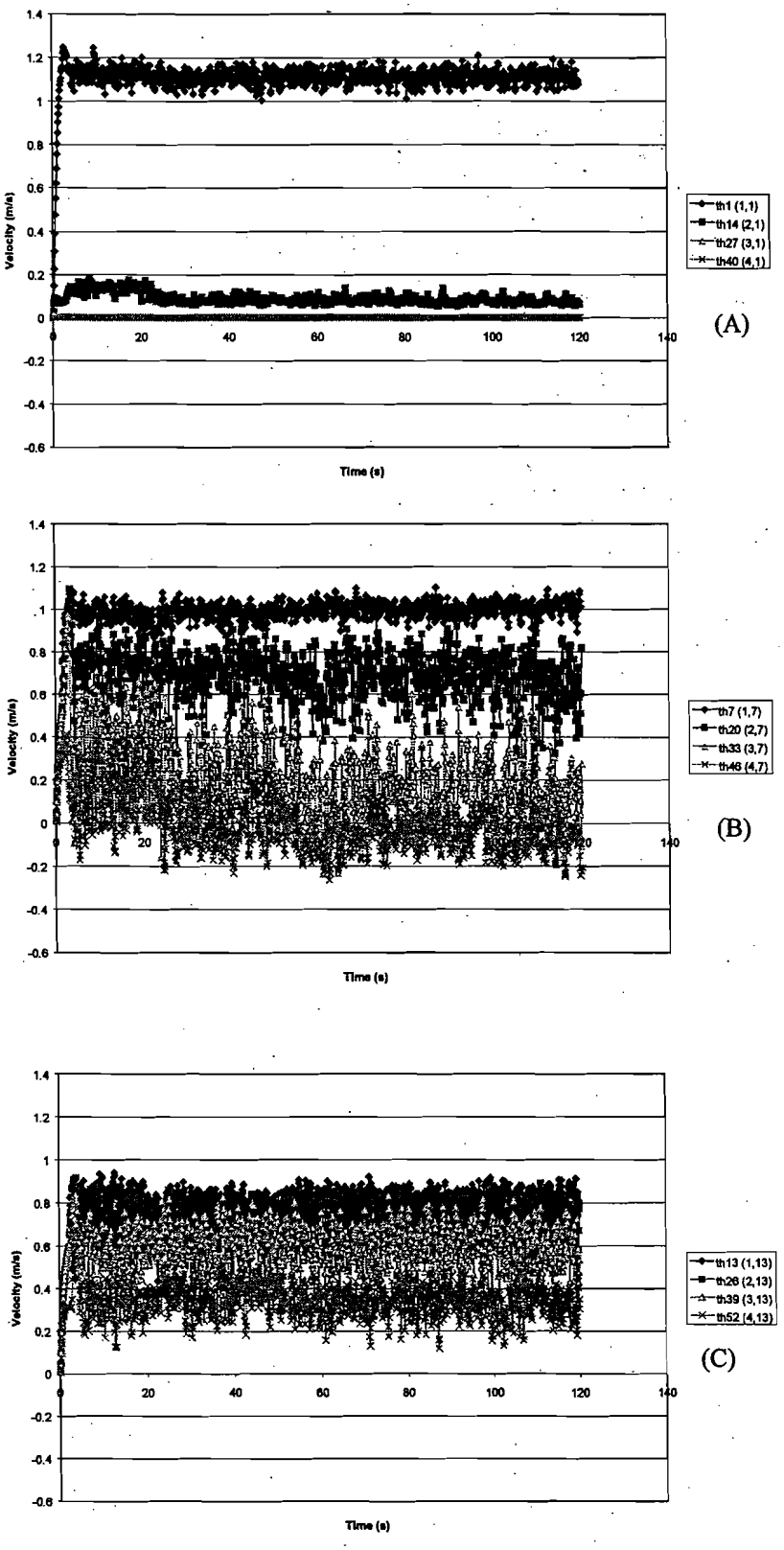

Figure 4: Time evolution of the velocity for 0.89 m/s supplied top hat flow measured at a) x = 0 m, B) x = 0.457 m, and C) x = 0.914 m

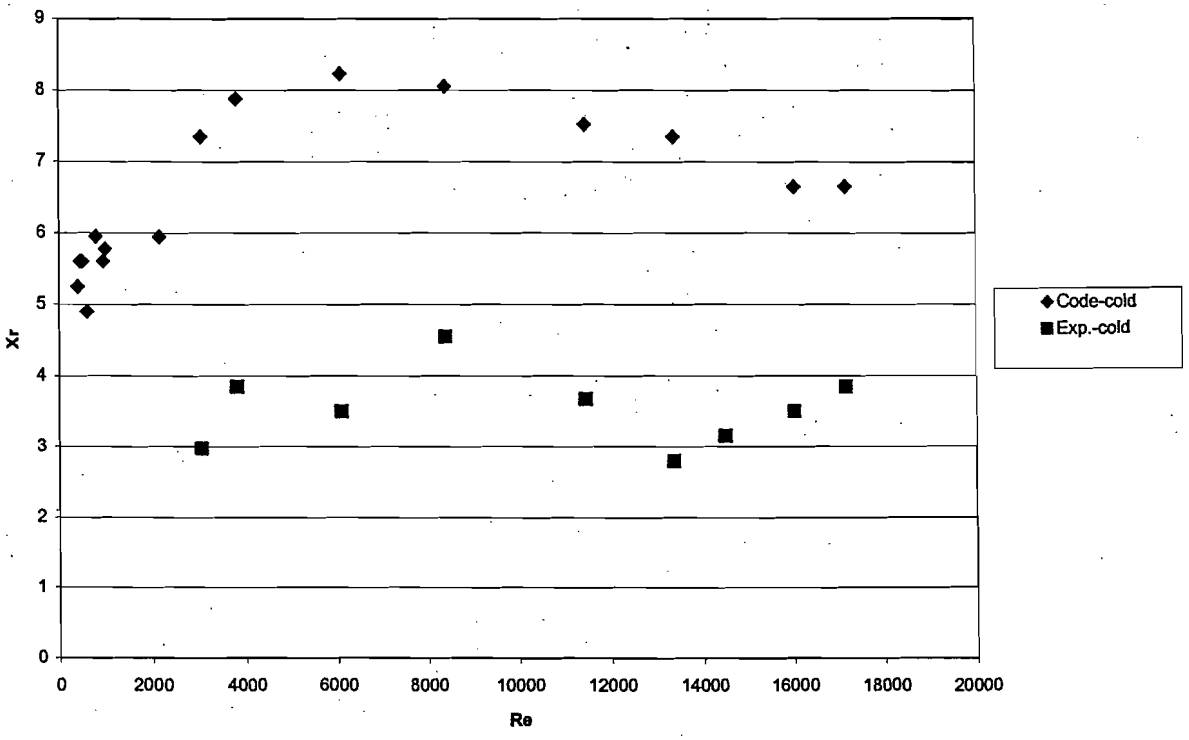

Figure 6: A comparison of recirculation zone lengths vs. Reynolds number for the simulated (Code) and experimental configurations. Cold flow.

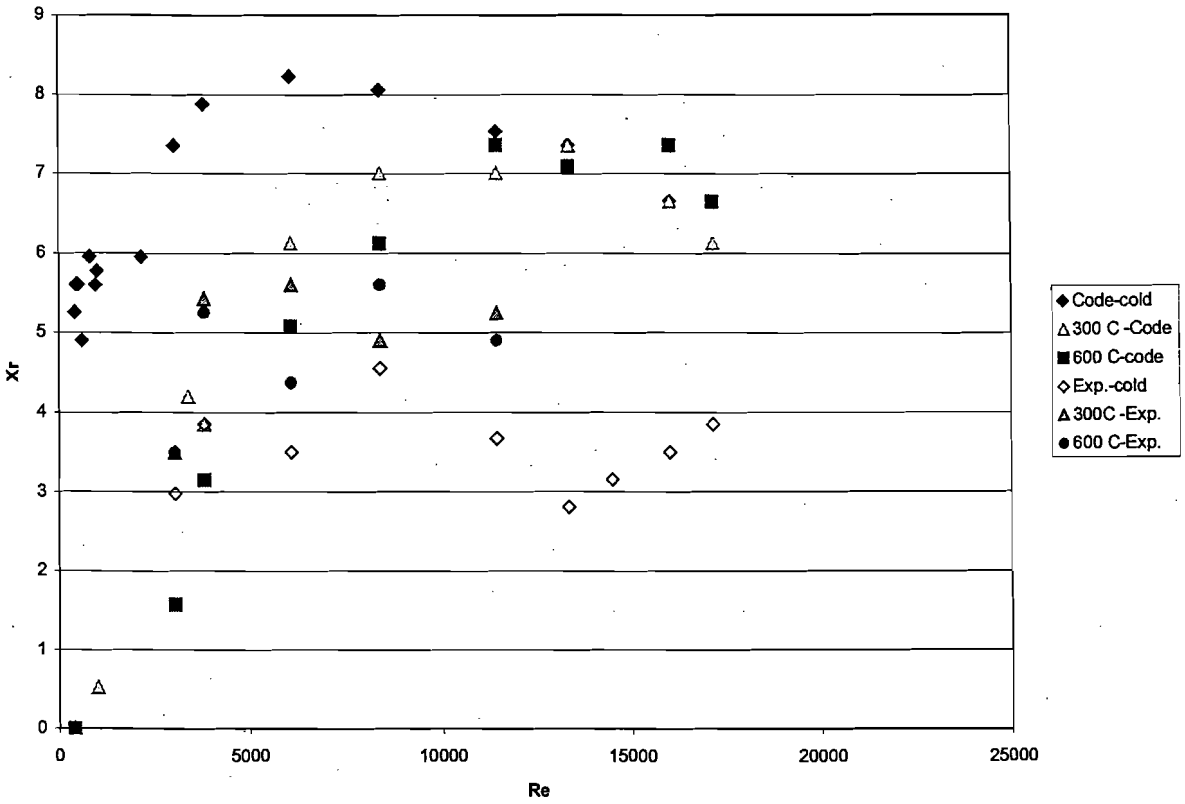

Figure 7: Recirculation zone length vs. Reynolds number for 300 C and 600 C flows

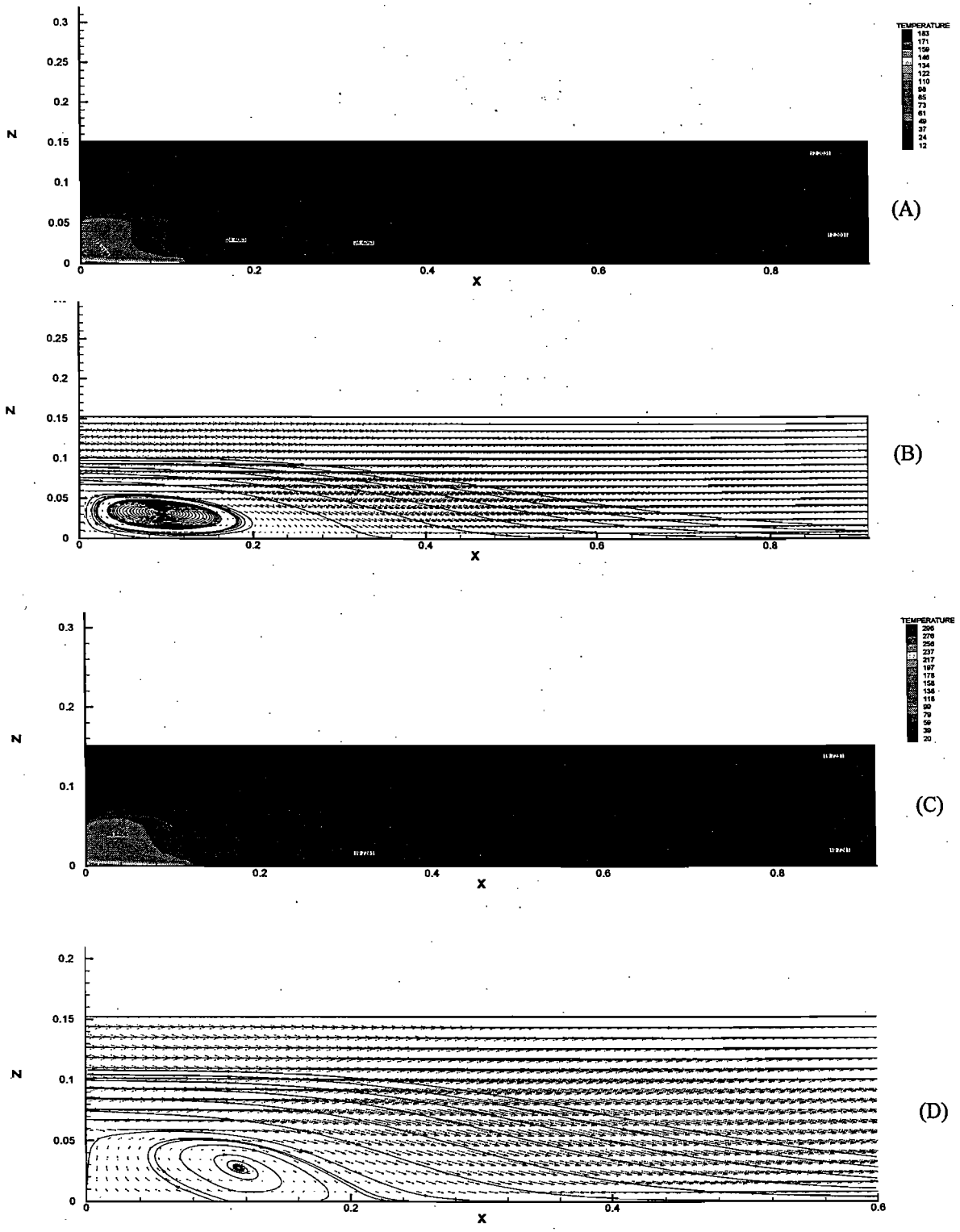

Figure 8: Average recirculation zone streamlines and thermal contour plots for 300 C and 600 C flows. A) Thermal contour behind step with 300 C hot plate setting, B) Velocity field with streamlines for 300 C hot plate simulation, C) Thermal contour behind step with 600 C hot plate setting, D), Velocity field with stream lines for 600 C hot plate simulation.

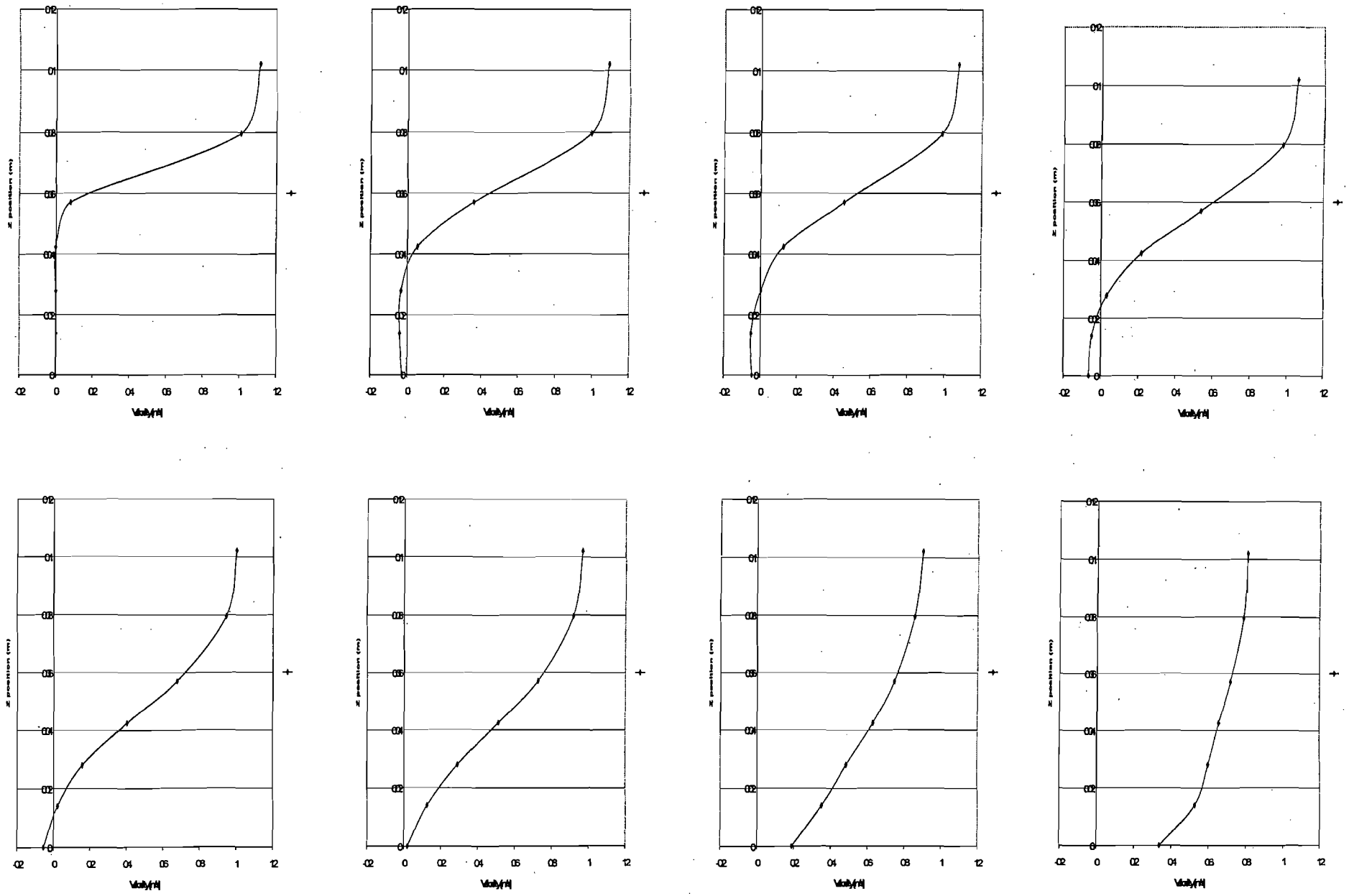

Figure 9: Velocity profiles for 0.89 m/s flow. Downstream locations featured A) x = 0 m, B) x = 0.152 m, C) x = 0.229 m, D) x = 0.305 m, E) x =0.457 m, F) x = 0.533 m, G) x = 0.686 m, H) x = 0.833 m

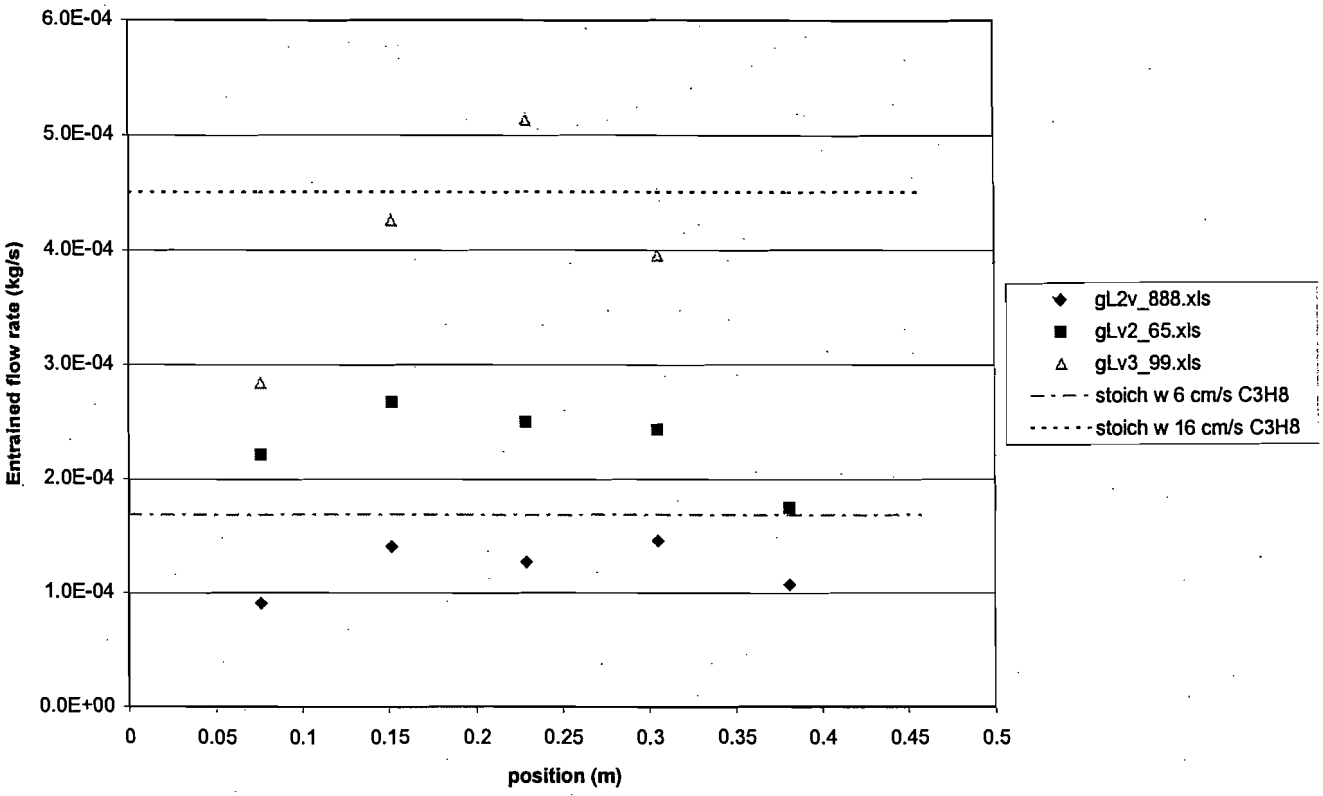

Figure 10: Rate of air entrainment vs. position downstream of the step at three flow speeds

Guide to Legend: Air flow velocities supplied ◆= 0.89 m/s, ■=2.65 m/s, Δ=3.99 m/s
Stoichiometric air flow rates for 6 cm3/s influx of Propane —-—
Stoichiometric air flow rate required for 16 cm3/s influx of Propane -----

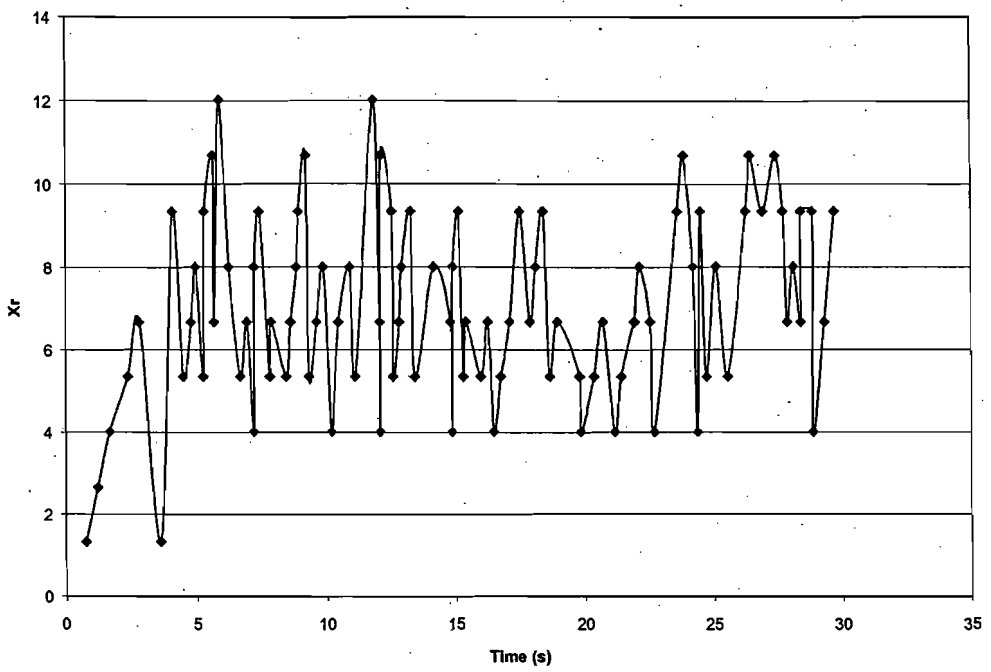

Figure 11: Trace of the incidence of positive to negative velocity transitions along the floor of the wind tunnel when supplied velocity is 0.89 m/s

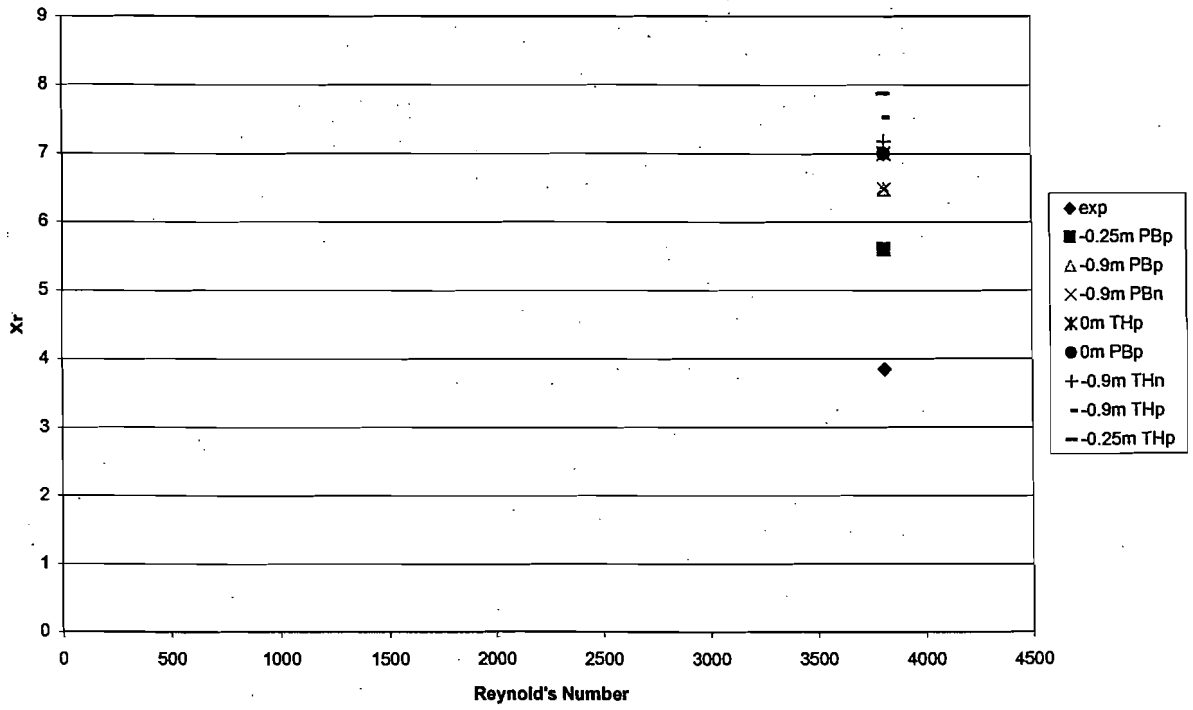

Figure 12: Variations in nondimensional recirculation length as a function of inlet and flow conditions for the 1 m/s equivalent flow conditions

Legend descriptor for 1 m/s flows:

	Exp	Experimental value measured for recirculation zone
0m	PB p	0m inlet length, parabolic flow profile, partial slip step boundary conditions
-0.25m	PB p	-0.25m inlet, Parabolic flow, partial slip
-0.9m	PB p	-0.9 m inlet, Parabolic flow, partial slip
-0.9m	PB n	-0.9m inlet, Parabolic flow, nonslip step
0m	TH p	0m inlet, Top Hat, partial slip
-0.25m	TH p	-0.25m inlet, Top Hat, partial slip
-0.9m	TH p	-0.9m inlet, Top Hat, partial slip
-0.9m	TH n	-0.9m inlet, Top Hat, nonslip step

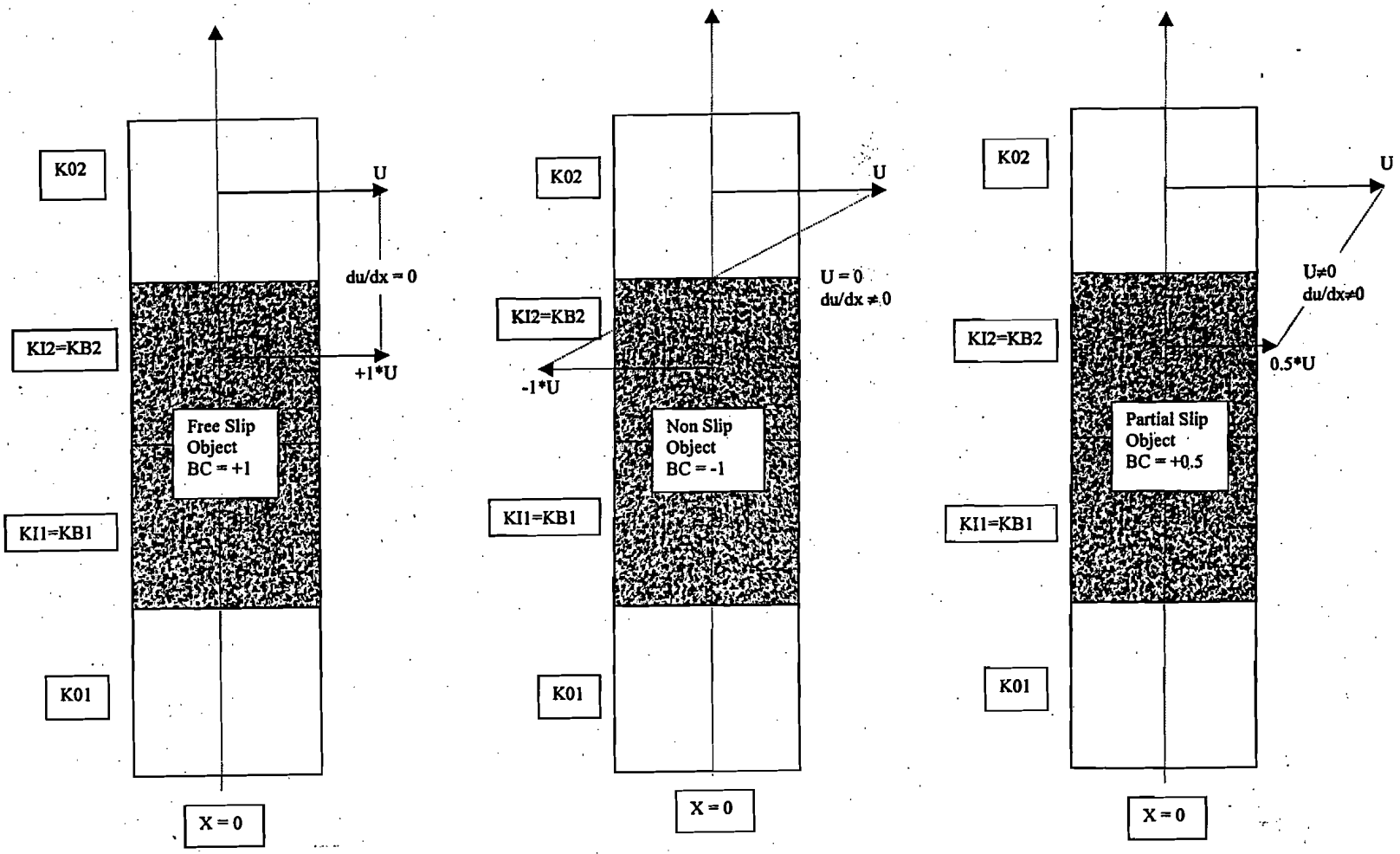

Figure 13: Illustration of the application of surface slip boundary conditions to the computational domain

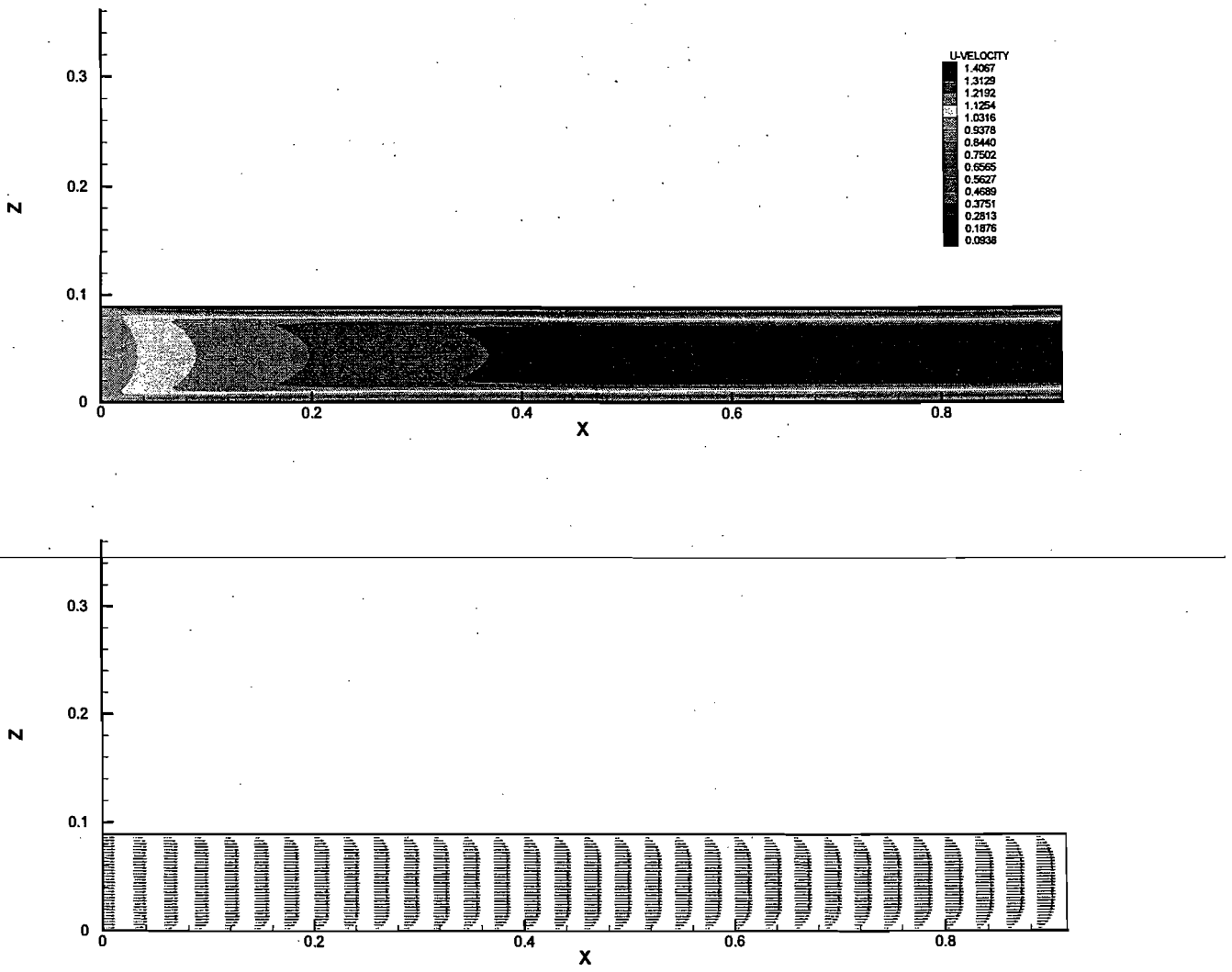

Figure 14: Average velocity contour and vector plots for flow through a duct with nonslip surfaces – Top hat profile specified

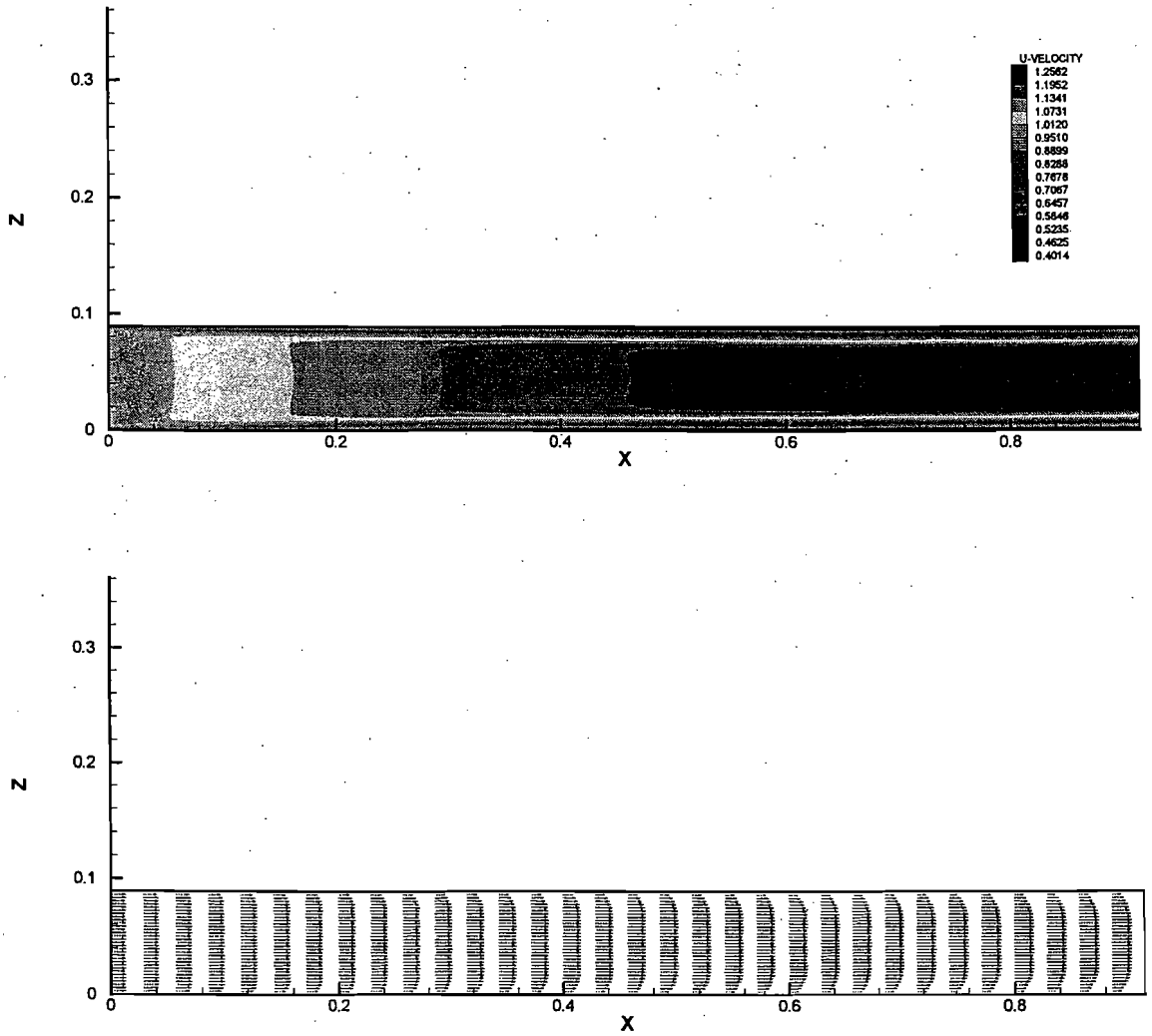

Figure 15: Average velocity contour and vector plots for flow through a duct with partial slip surfaces – Top hat profile specified

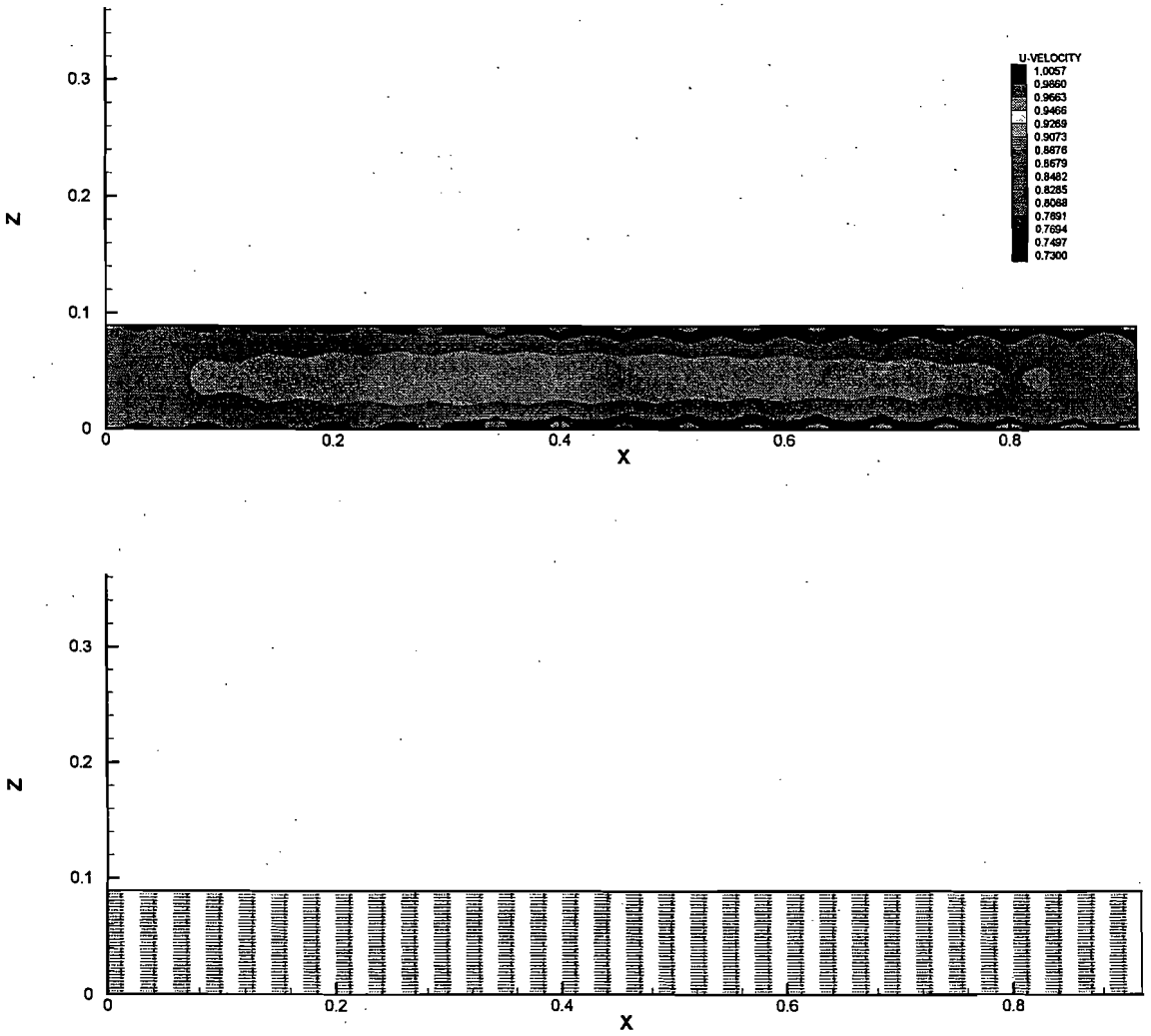

Figure 16: Average contour and vector velocity plots for flow through a duct with free slip surfaces – Top hat profile specified

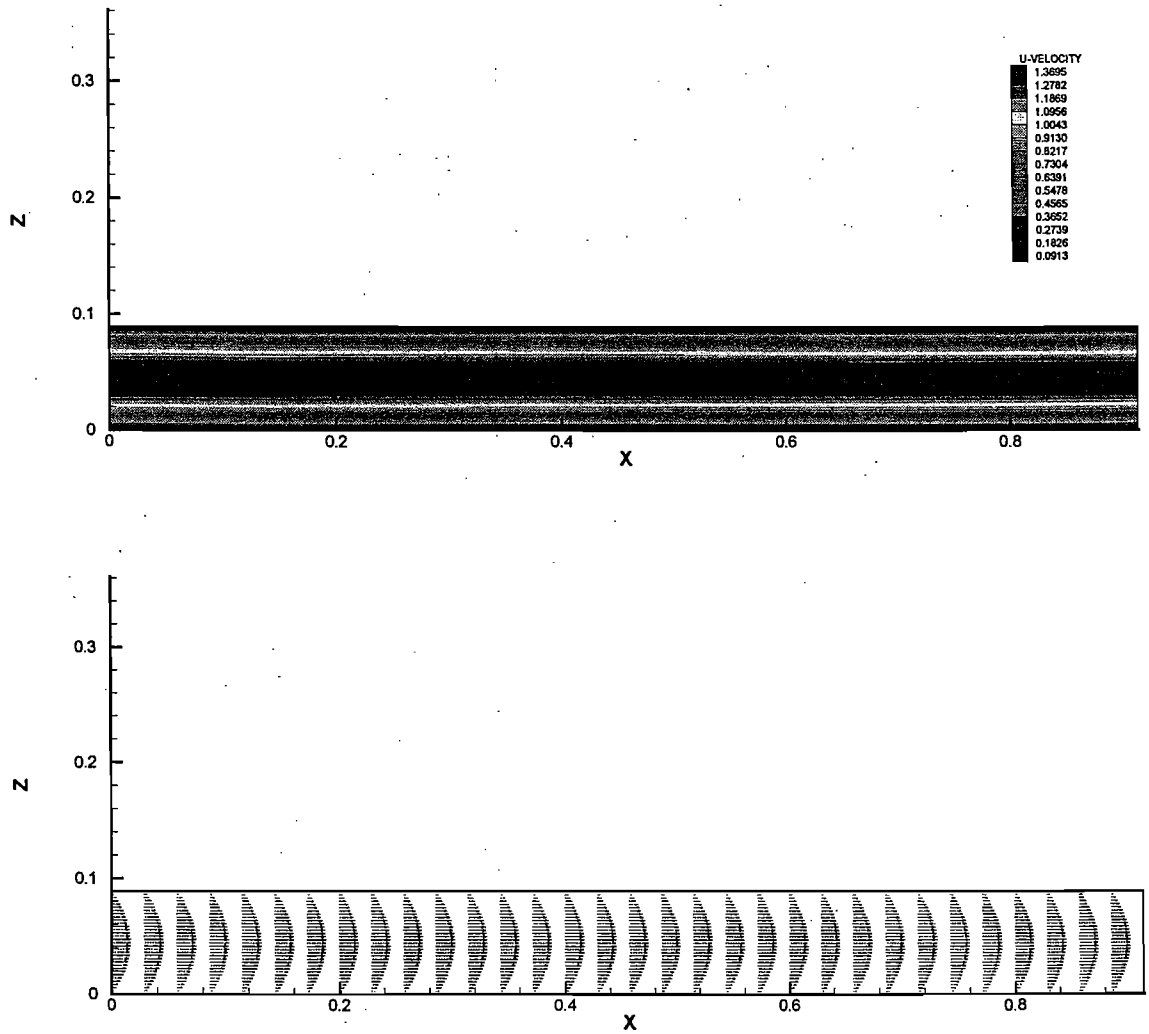

Figure 18: Average contour and vector velocity plots for flow through a duct with non-slip surfaces – Parabolic profile specified.

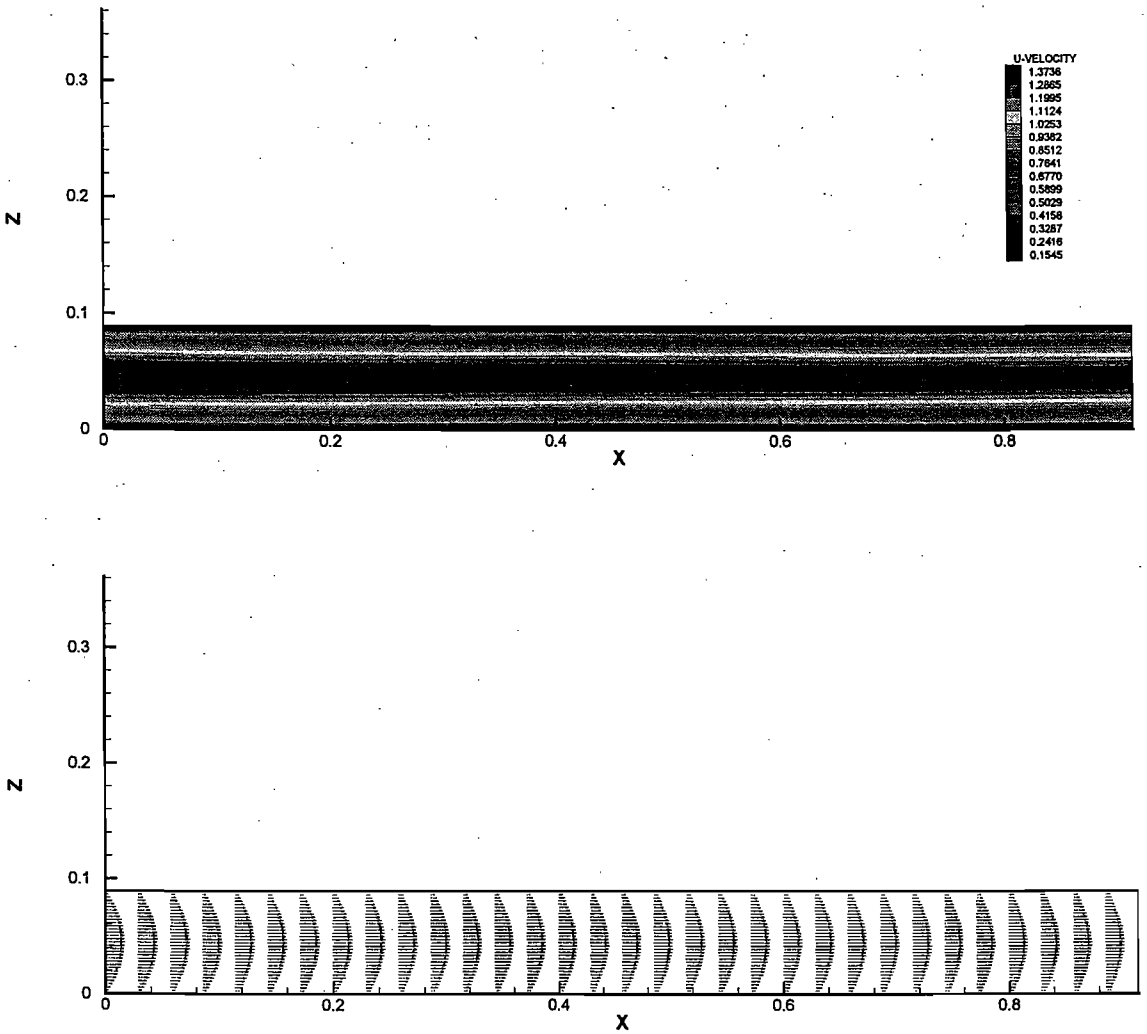

Figure 19: Average contour and vector velocity plots for flow through a duct with partial slip surfaces – Parabolic profile specified.

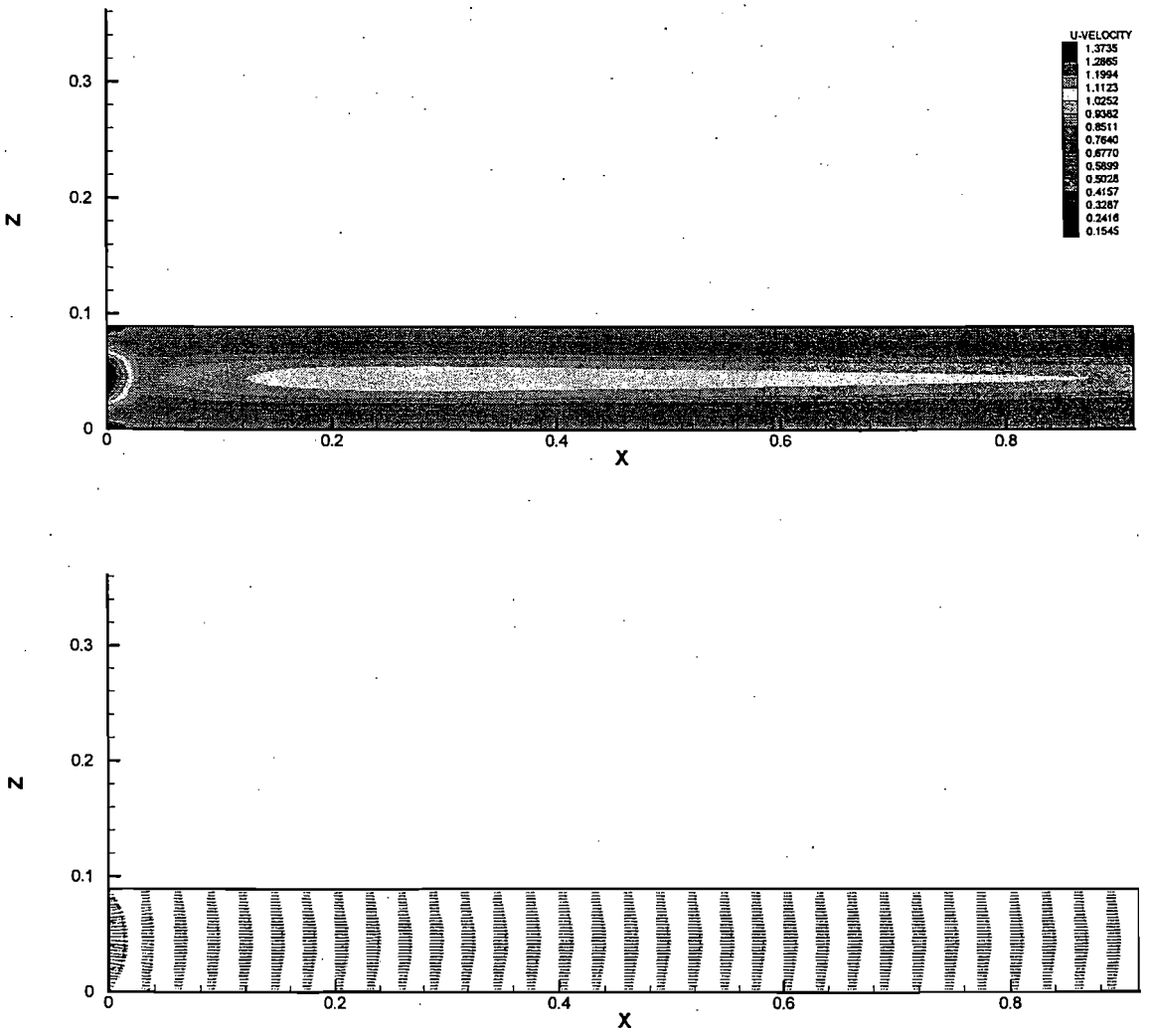

Figure 20: Average contour and vector velocity plots for flow through a duct with free slip surfaces – Parabolic profile specified

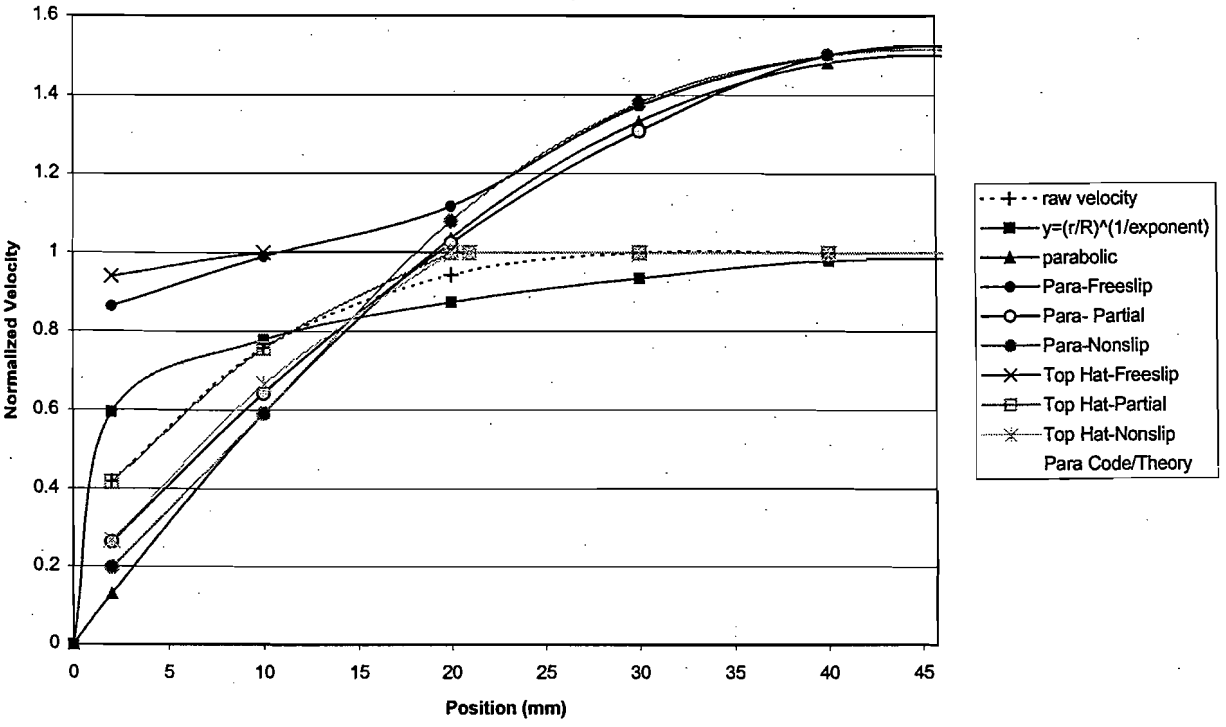

Figure 21: Duct exit velocity profiles for simulated, theoretical, and experimental flows

Guide to Legend: Experimental data is represented by "raw velocity". The theoretical turbulent profile is denoted by "y = (r/R)^(1/exponent)"; the theoretical parabolic profile by "parabolic". Simulated free-, partial-, and nonslip flows are represented with the prefix "Para". Simulated free-, partial-, and nonslip flows are represented with the prefix "Top Hat"

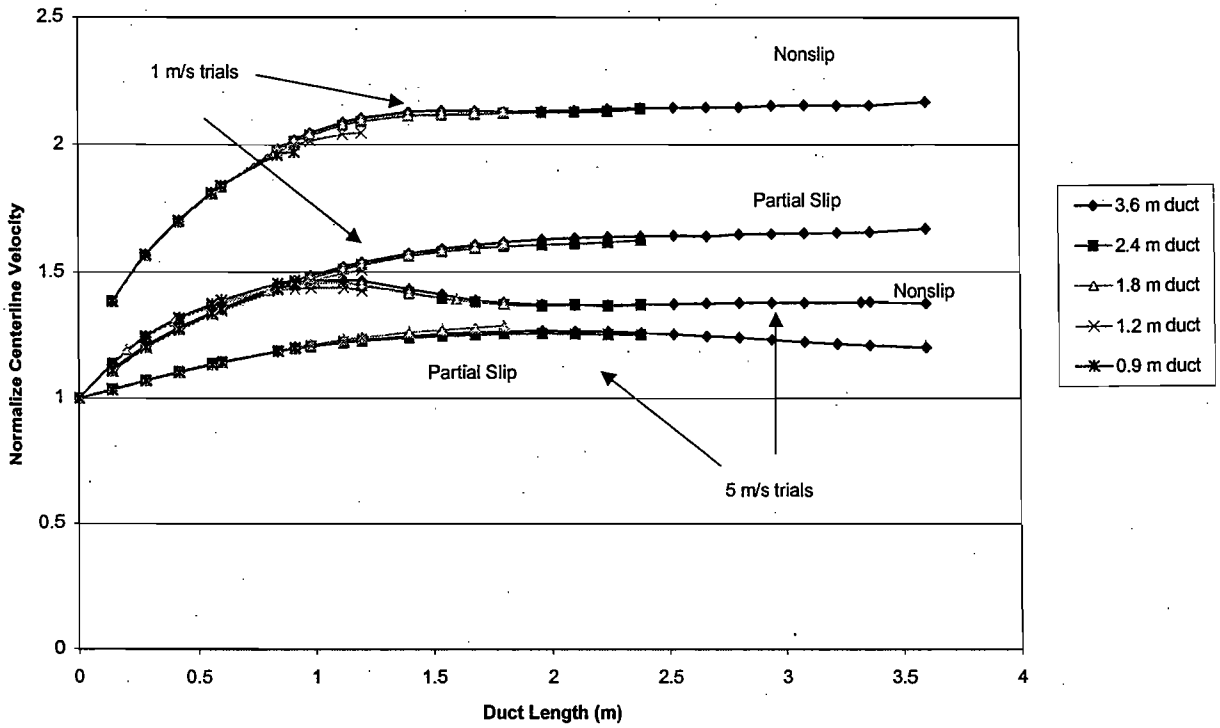

Figure 22: Outcome of duct length experiments expressed in terms of the normalized centerline velocity vs. duct length.

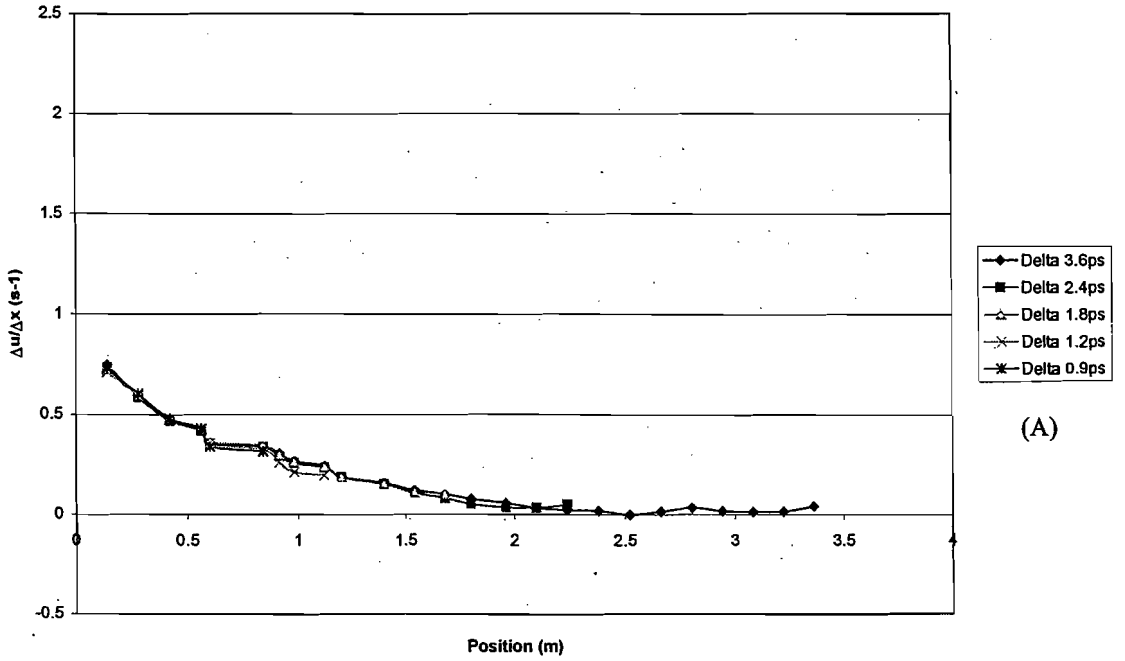

(A)

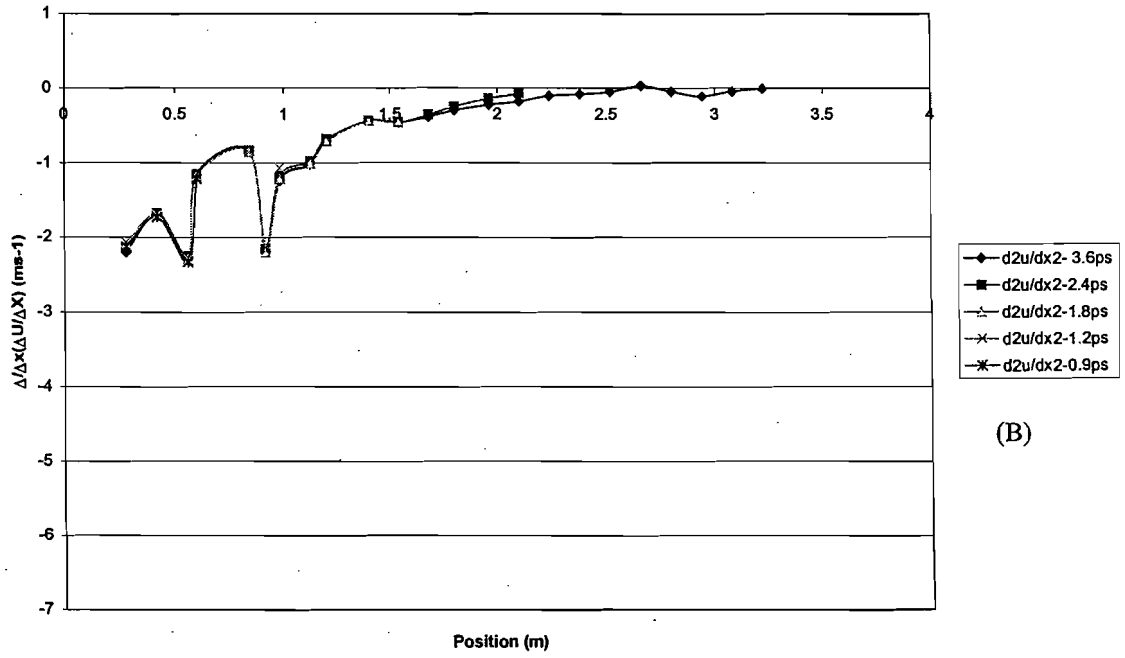

(B)

Figure 24: Streamwise velocity gradients for 1 m/s flow through straight ducts with partial slip surfaces. A) First derivative – changes in velocity, B) Second derivative – variation in du/dz

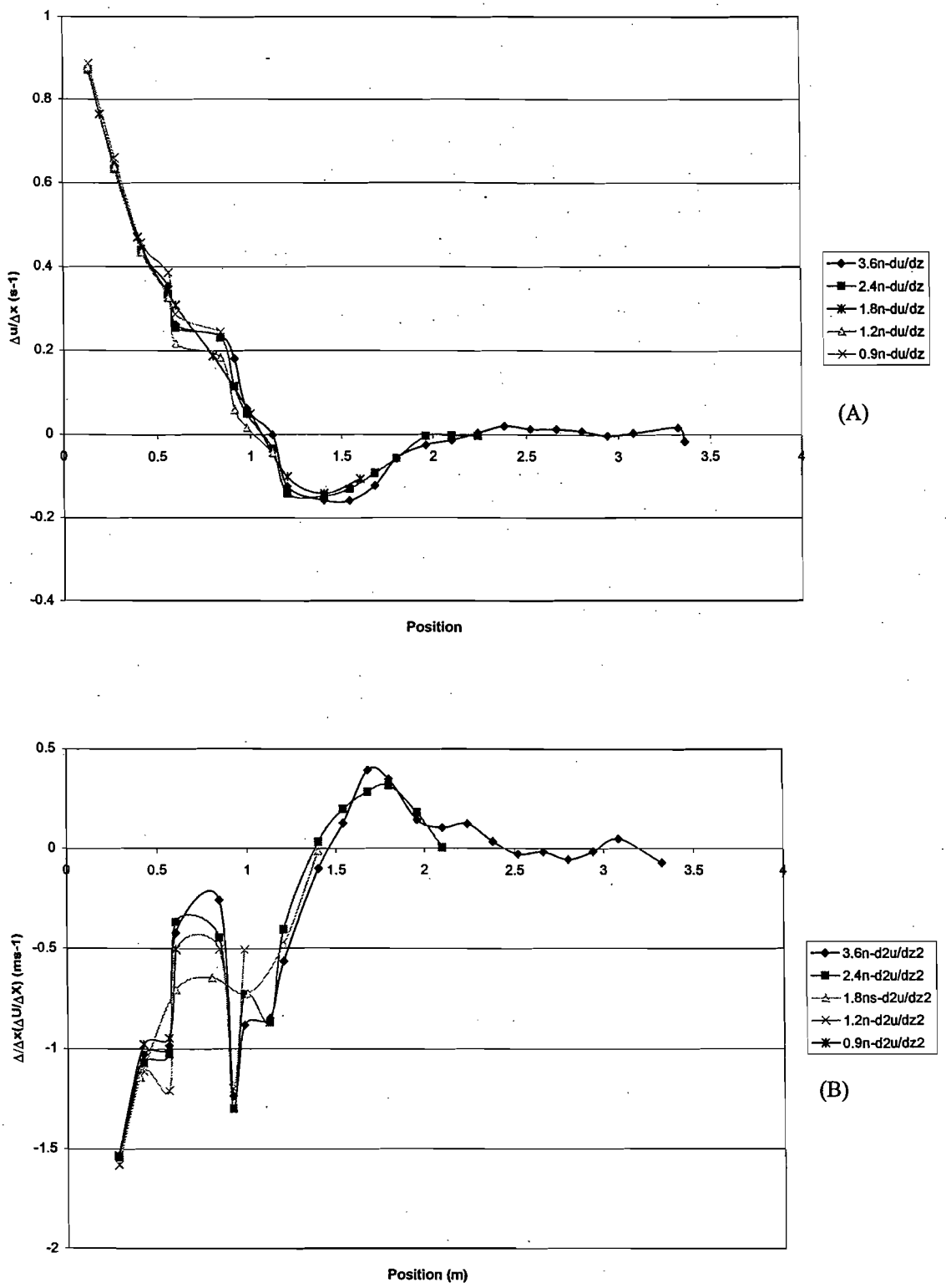

Figure 25: Streamwise velocity gradients for 5 m/s flow through straight ducts with nonslip surfaces. A) First derivative – change in velocity, B) Second derivative – variations in du/dz

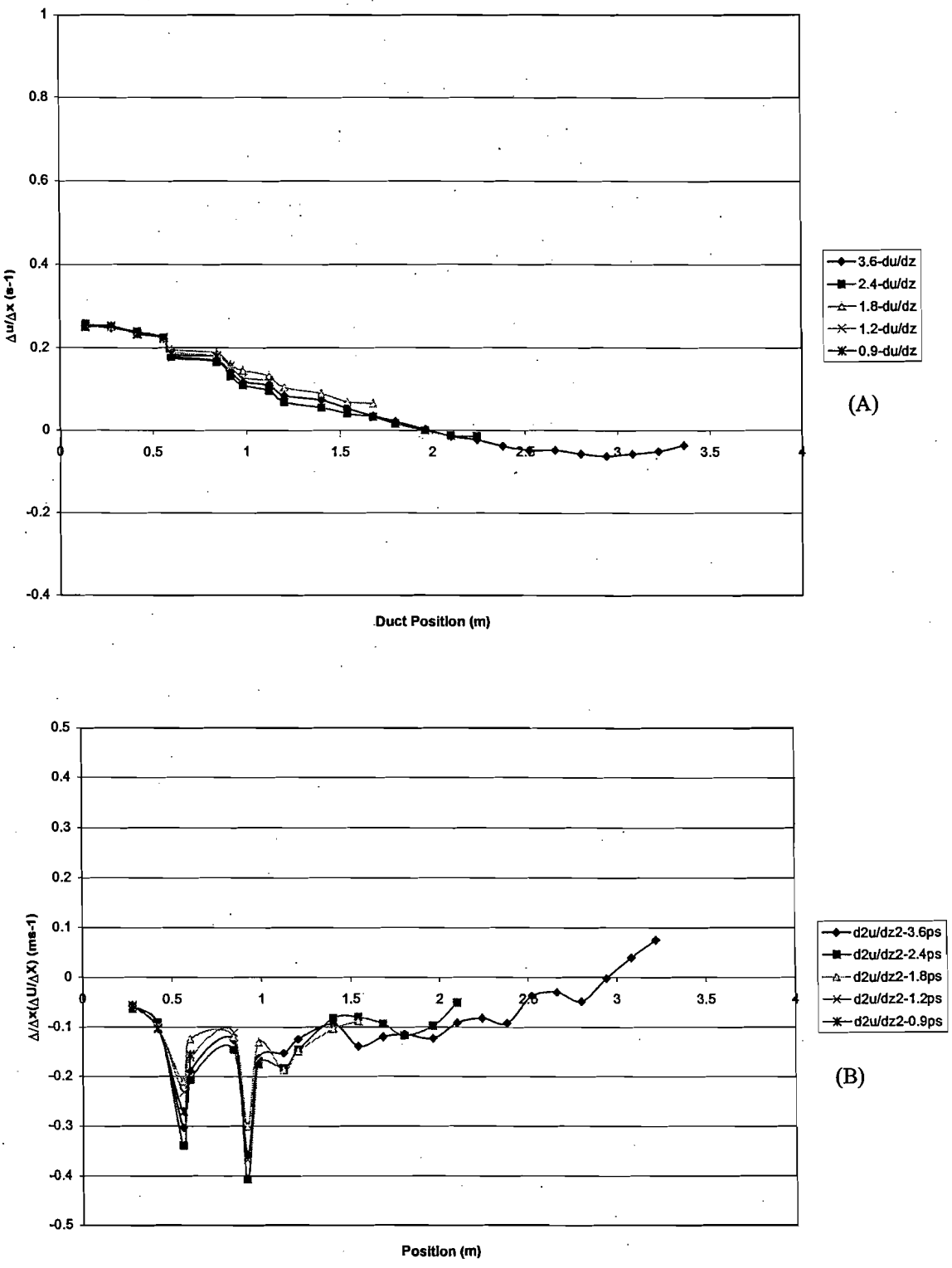

Figure 26: Streamwise velocity gradients for 5 m/s flow through straight ducts with partial slip surfaces. A) First derivative – changes in velocity, B) Second derivative – variations in du/dz

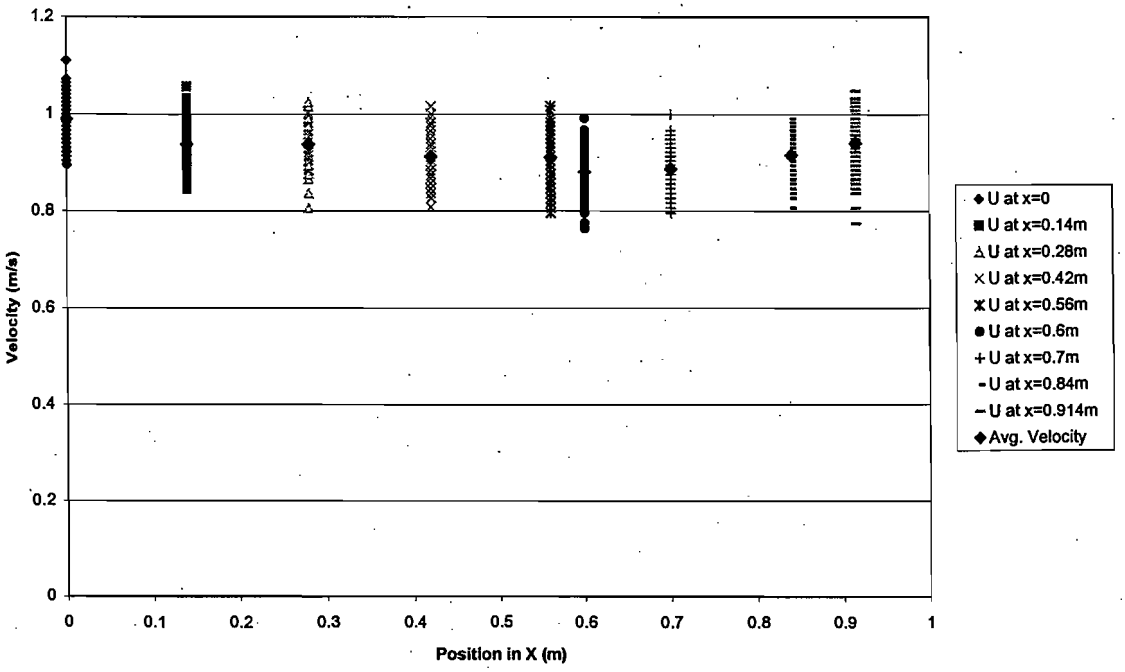

Figure 27: Centerline velocity as a function of position along duct for 1 m/s experimental flow (Step height = 0 mm)

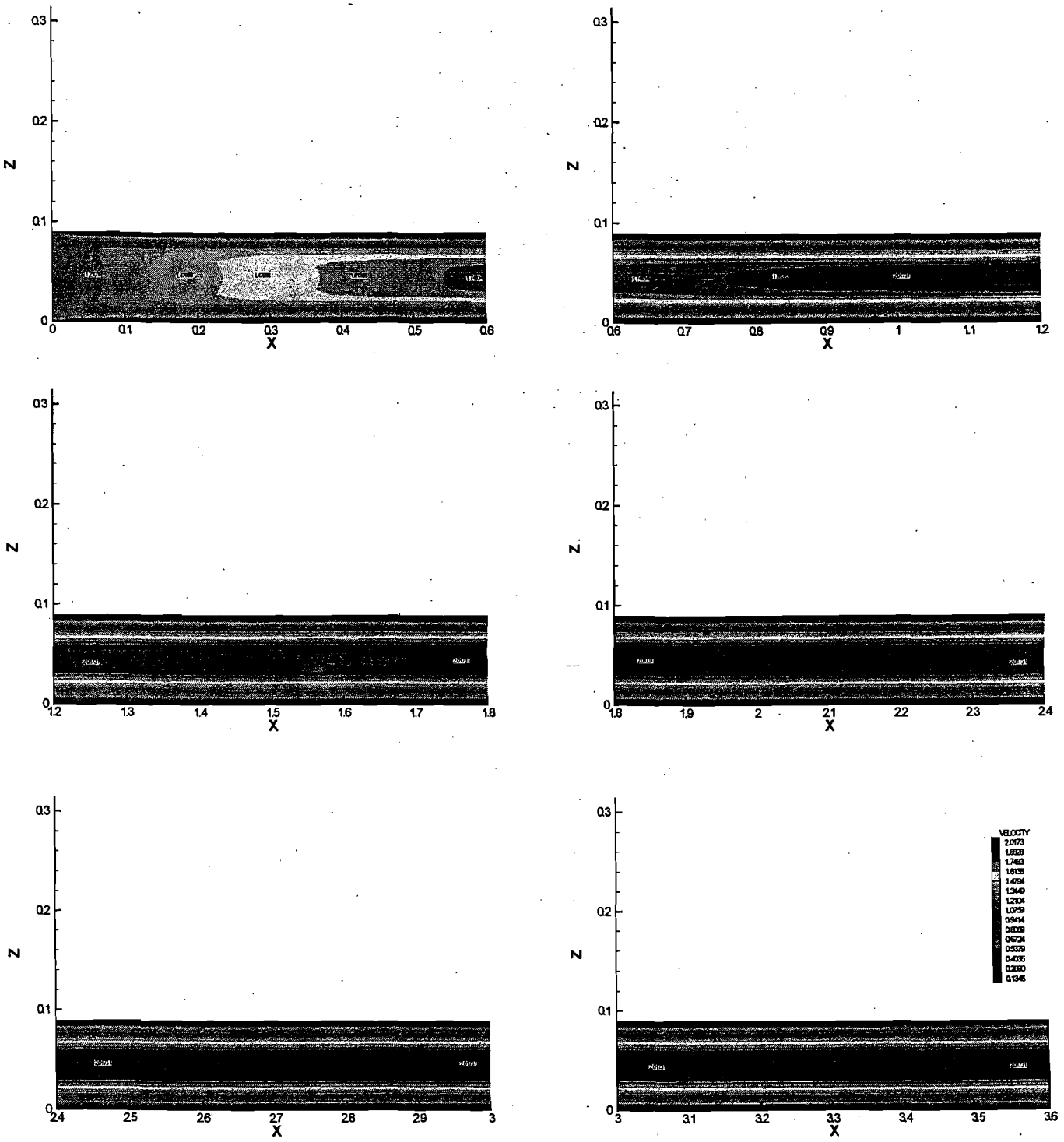

Figure 28A: Evolution of velocity through a 3.6 m straight duct with nonslip surfaces – Contour plot

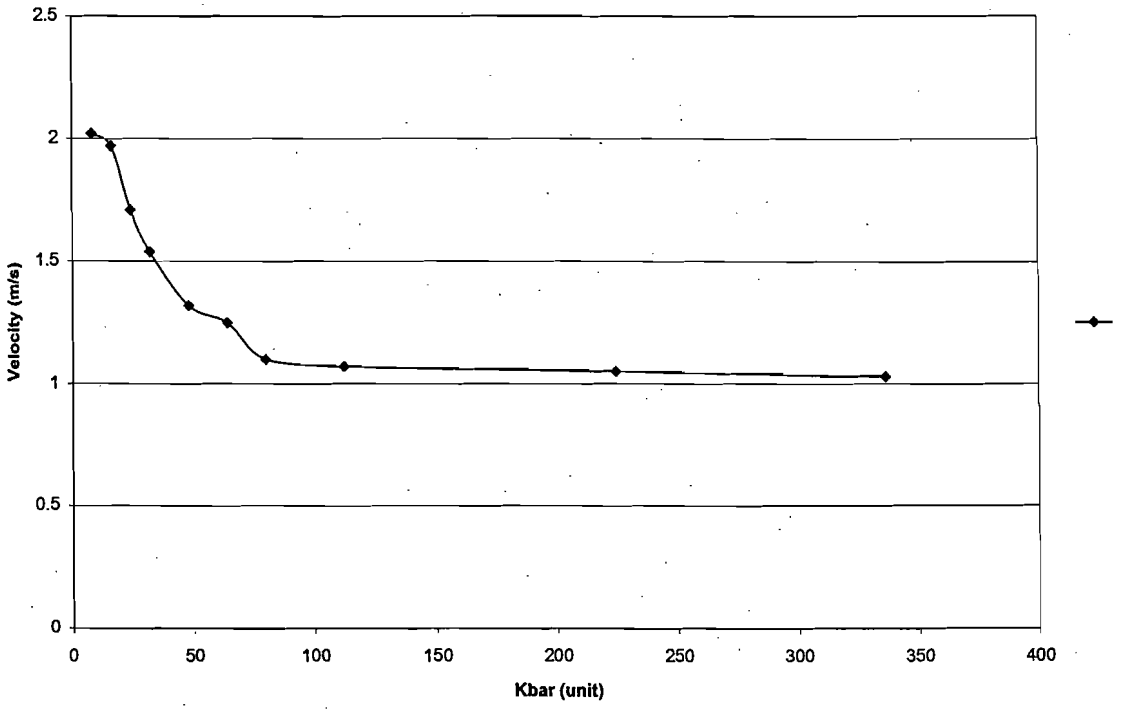

Figure 30: Variation in centerline end velocity with number of grid cells – LES simulation

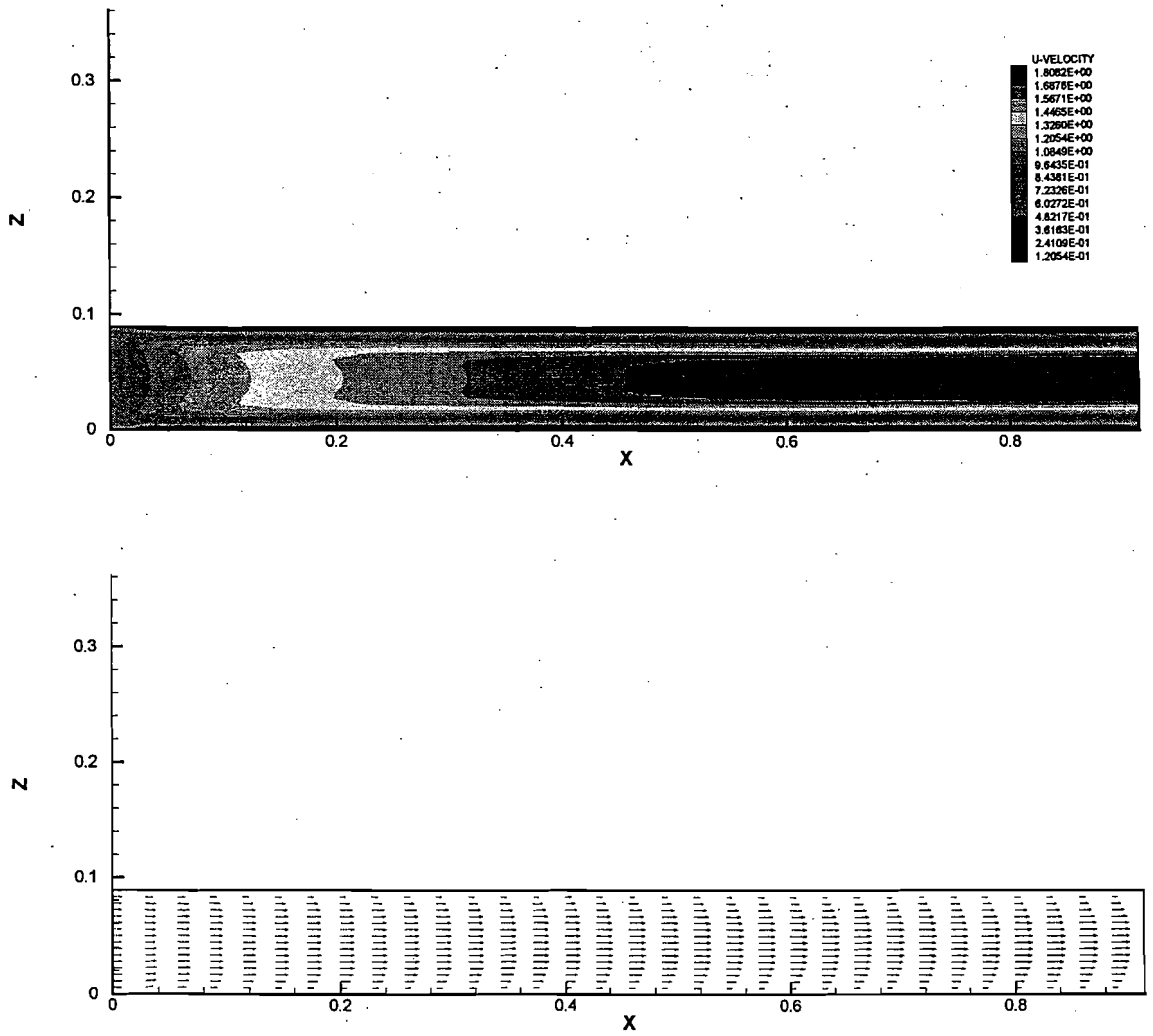

Figure 31: LES simulation of 0.9 m duct with nonslip surfaces. Average velocity contour and vector plots for 1 m/s flow. Grid spacing (32,16,16)

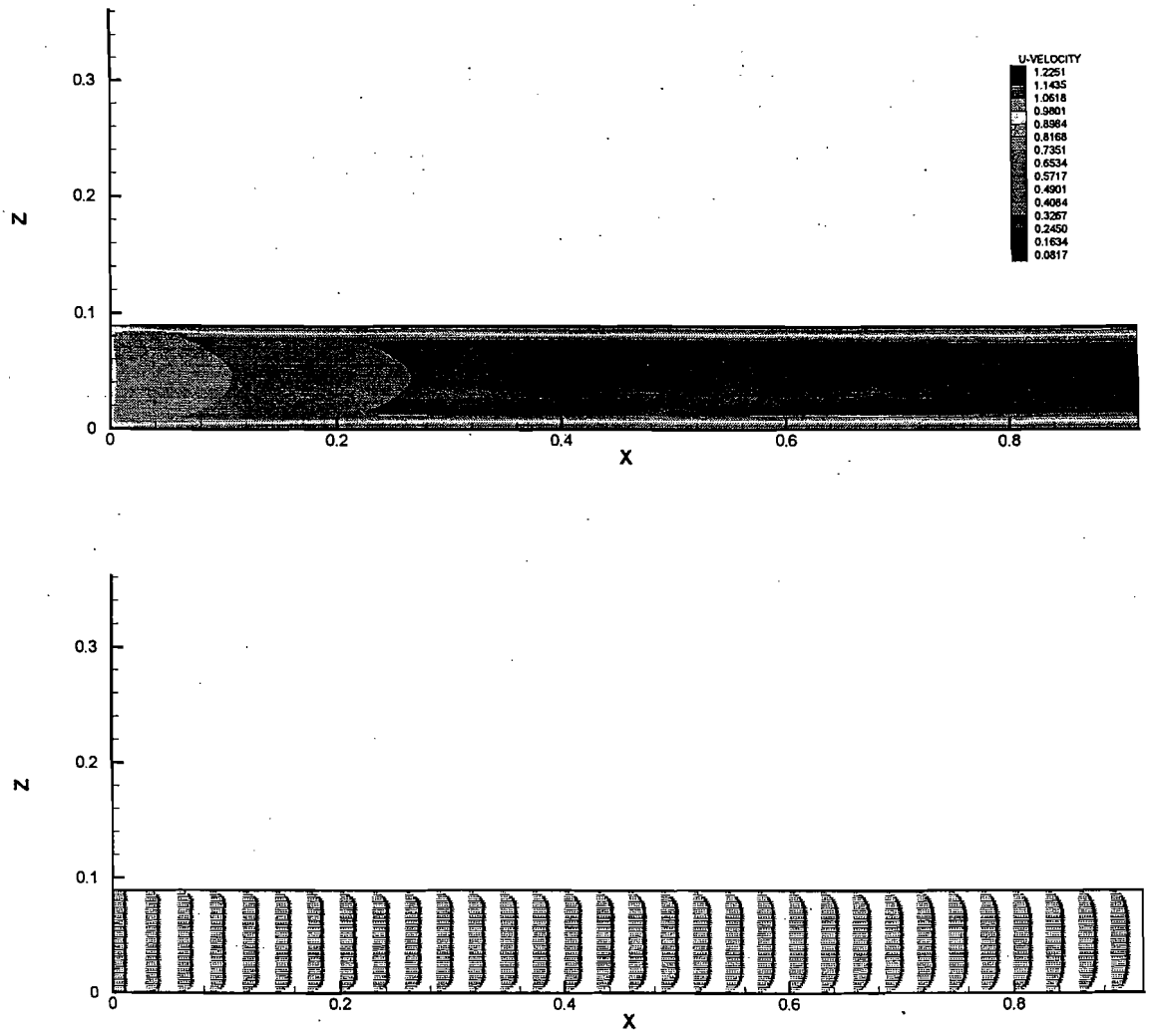

Figure 32: LES simulation of 0.9 m duct with nonslip surfaces. Velocity contour and vector plots for 1 m/s flow. Grid spacing (32,16,48)

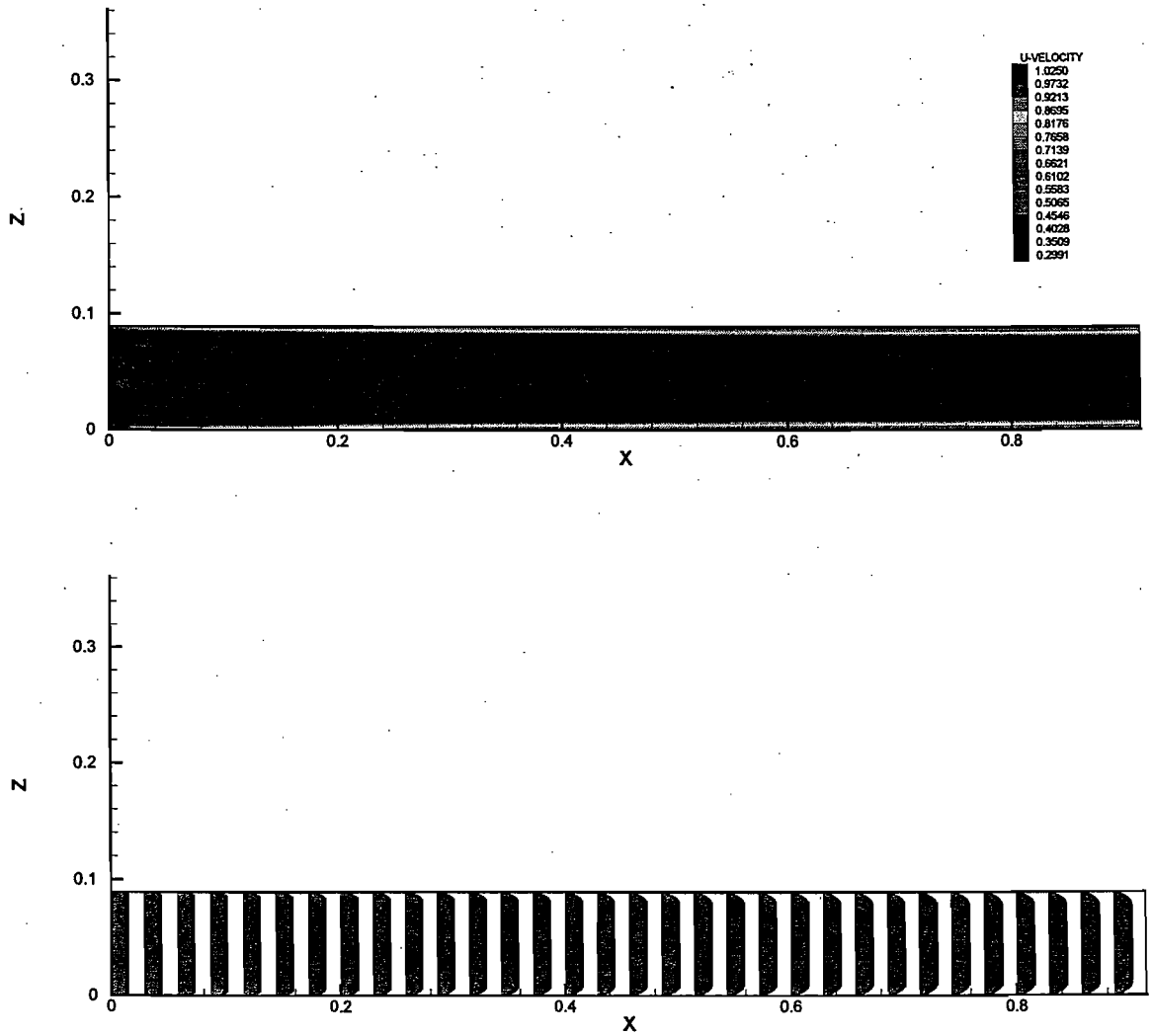

Figure 33: LES simulation of 0.9m duct with nonslip surfaces. Velocity contour and vector plots for 1 m/s flow. Grid spacing (32,16,80)

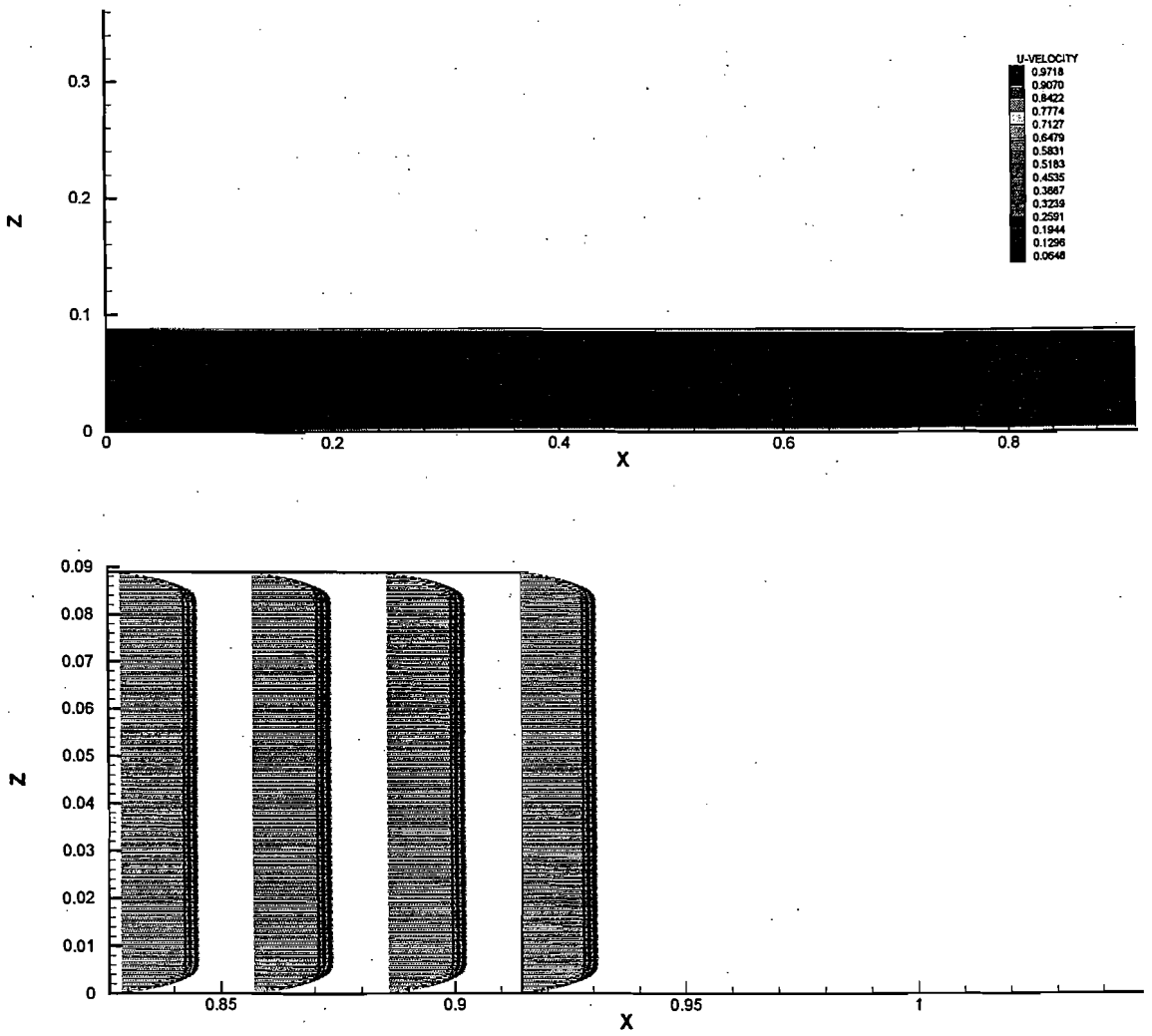

Figure 34: LES simulation of 0.9m duct with nonslip surfaces. Full velocity contour and duct exit vector plot for 1m/s flow. Grid spacing (32,16,225)

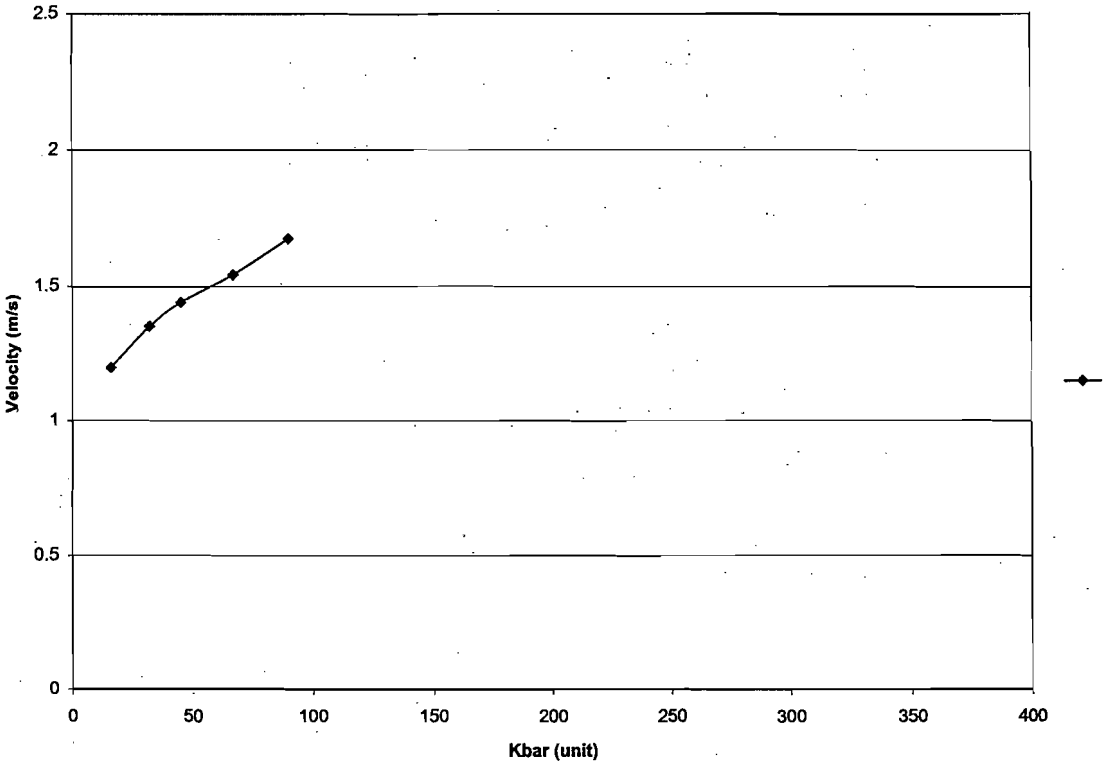

Figure 35: Variation in centerline end velocity with number of grid cells –DNS simulation

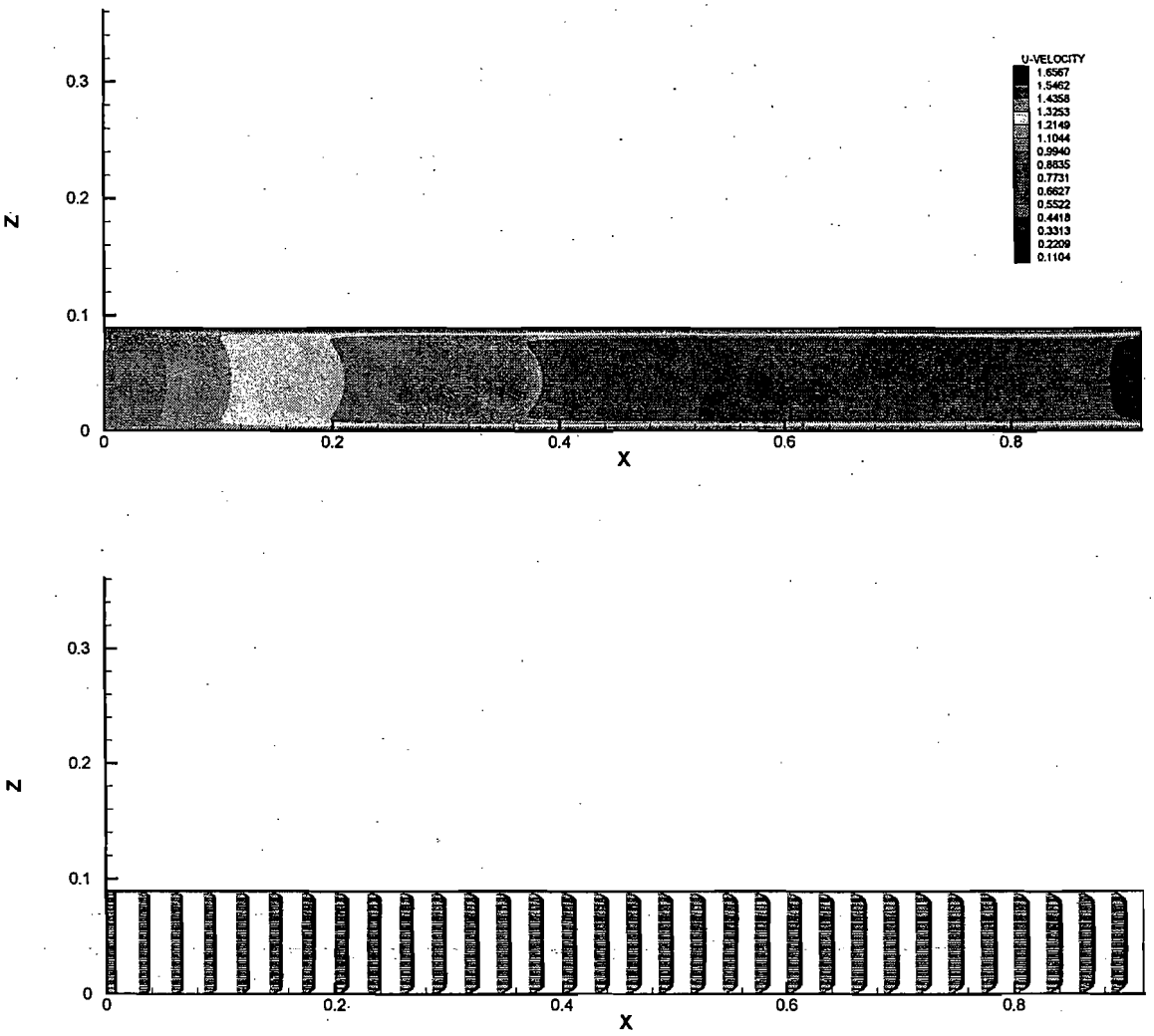

Figure 36: DNS simulation of 0.9 m duct with nonslip surfaces. Velocity contour and vector plots for 1 m/s flow. Grid spacing (32,16,90)

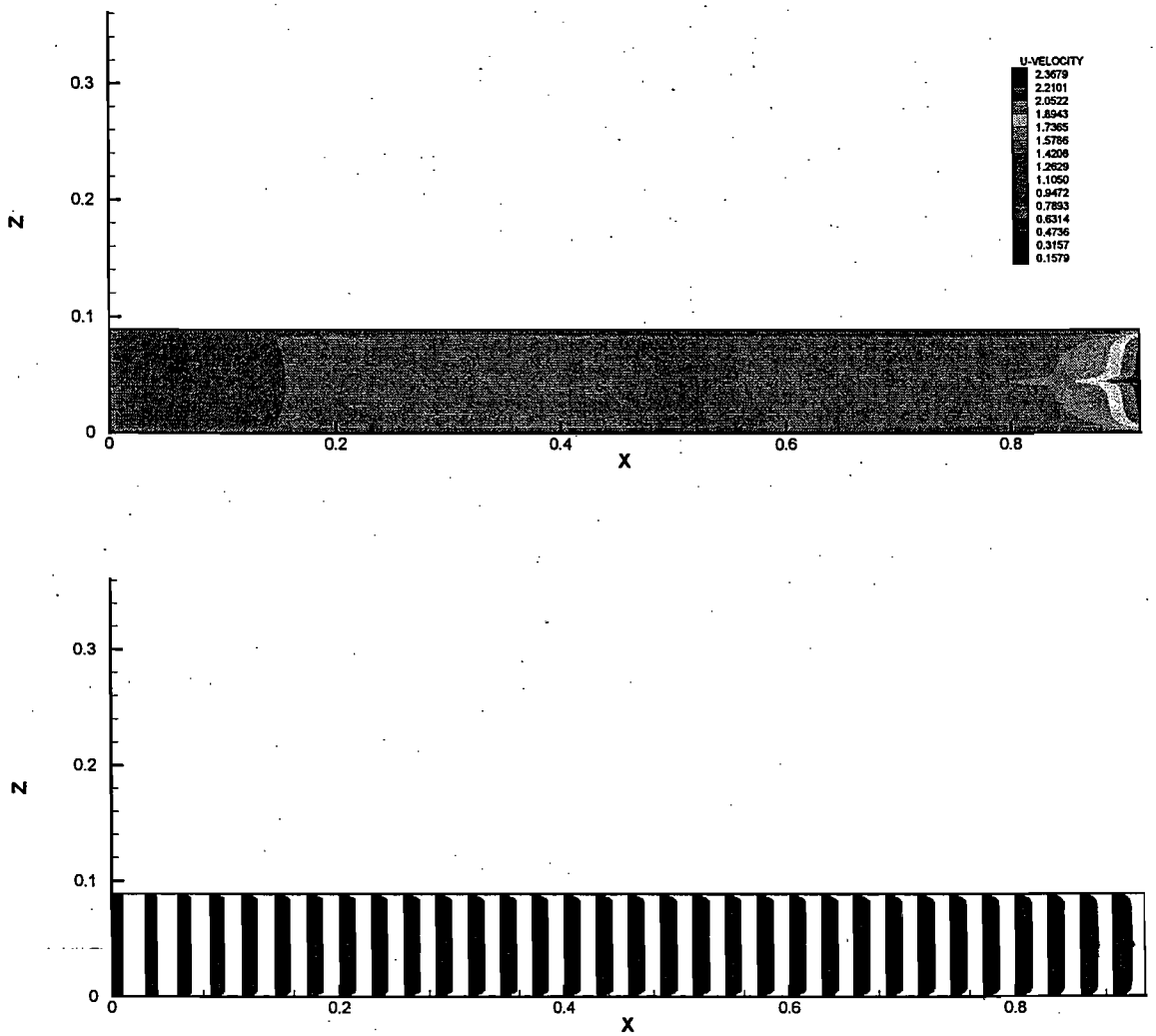

Figure 37: DNS simulation of 0.9m duct with nonslip surfaces. Velocity contour and vector plots for 1 m/s flow. Grid spacing (32,16,224)

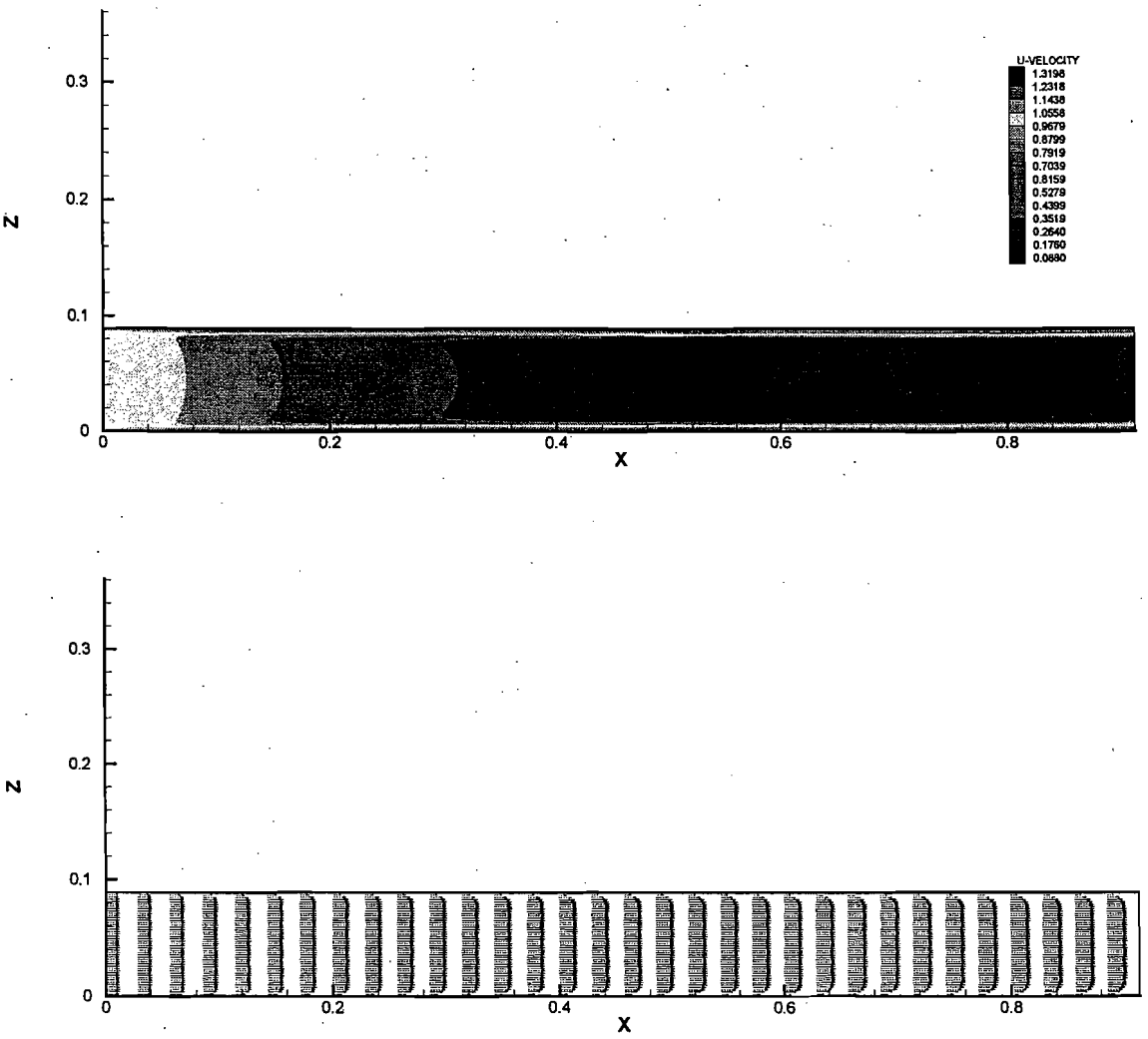

Figure 38: DNS simulation of 0.9m duct with nonslip surfaces. Velocity contour and vector plots for 1 m/s flow. Grid spacing (32,16,45)

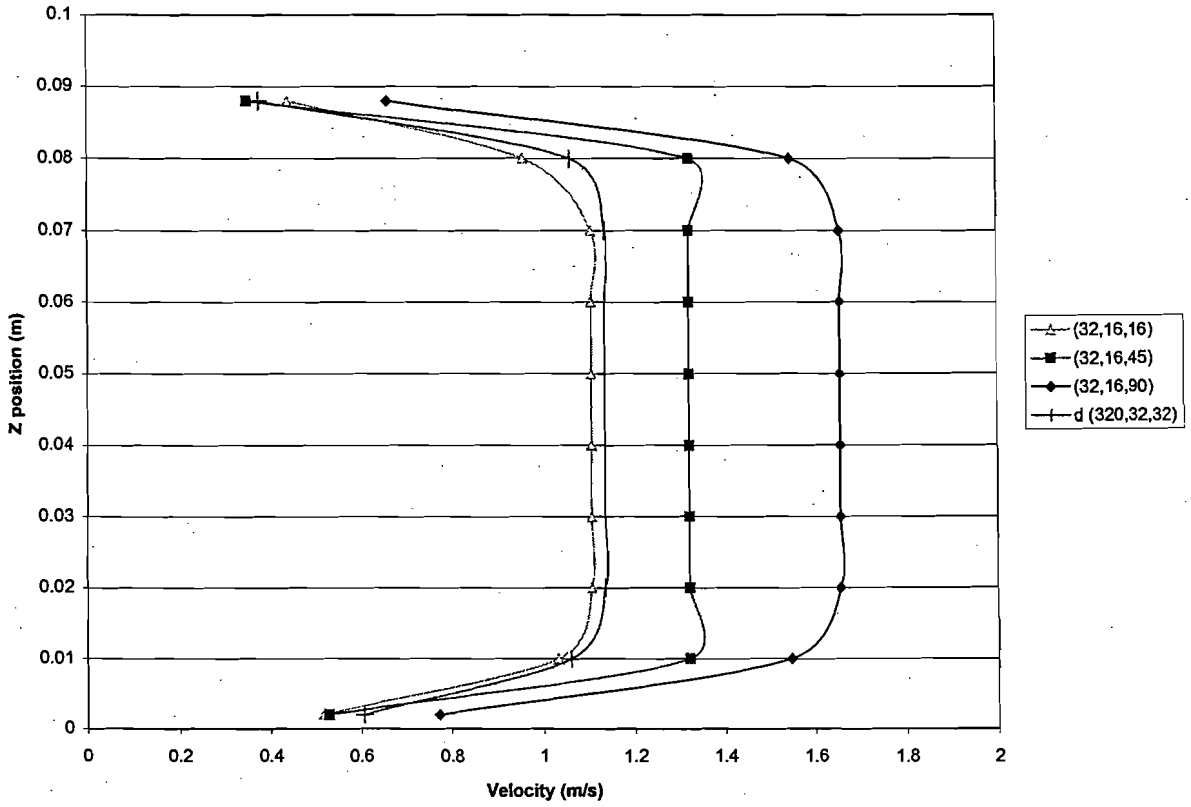

Figure 40: Velocity profile dependence on increasing grid cell count for DNS simulations

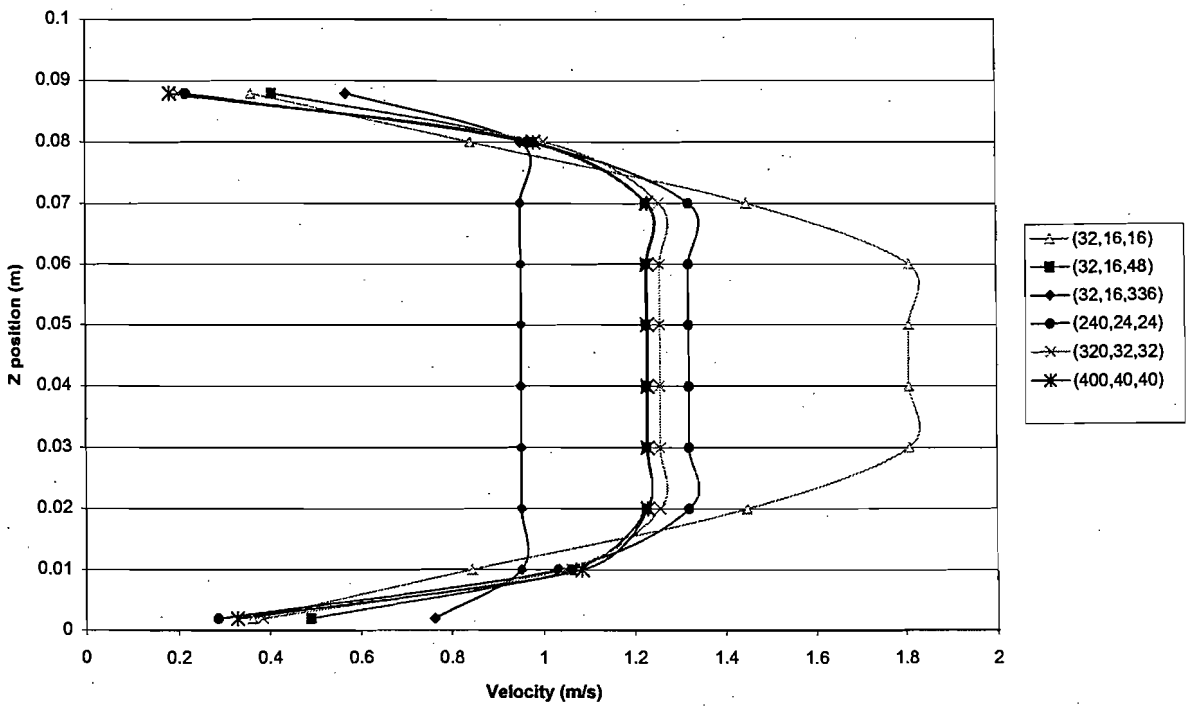

Figure 42: Velocity profile dependence on increasing grid cell count for LES simulations

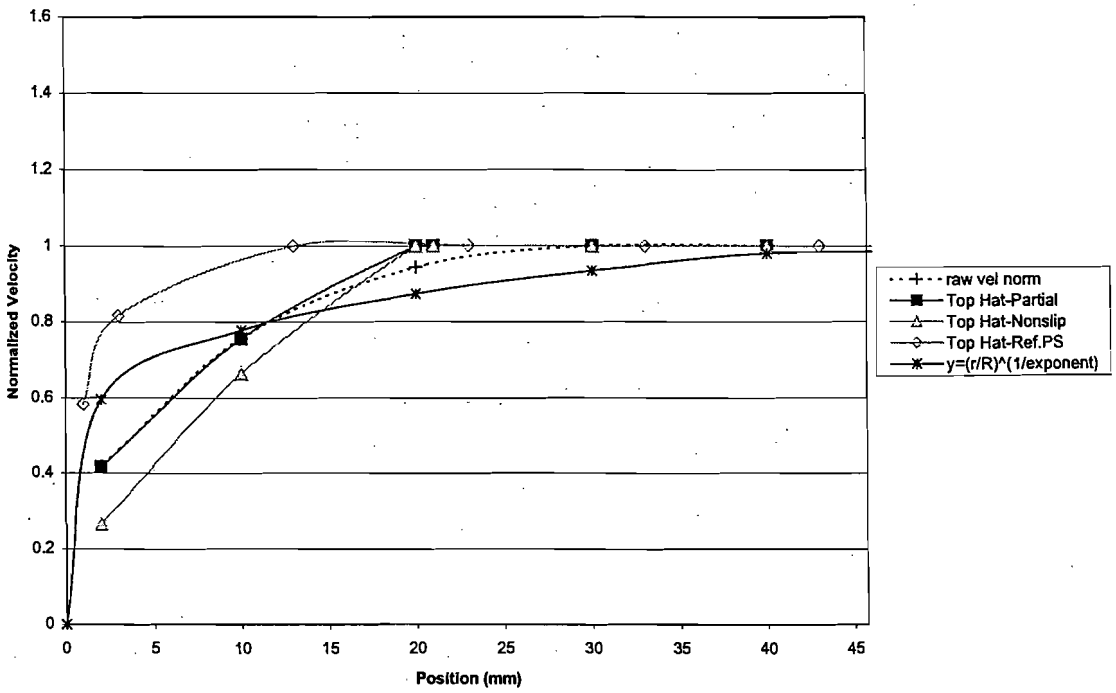

Figure 45: Velocity profiles for simulated, theoretical, and experimental flows

Guide to Legend: "Raw velocity" refers to the experimental data. The theoretical turbulent profile is denoted by "y=(r/R)^(1/exponent)". The simulation with the refined grid is denoted by "Top Hat- Ref. PS".

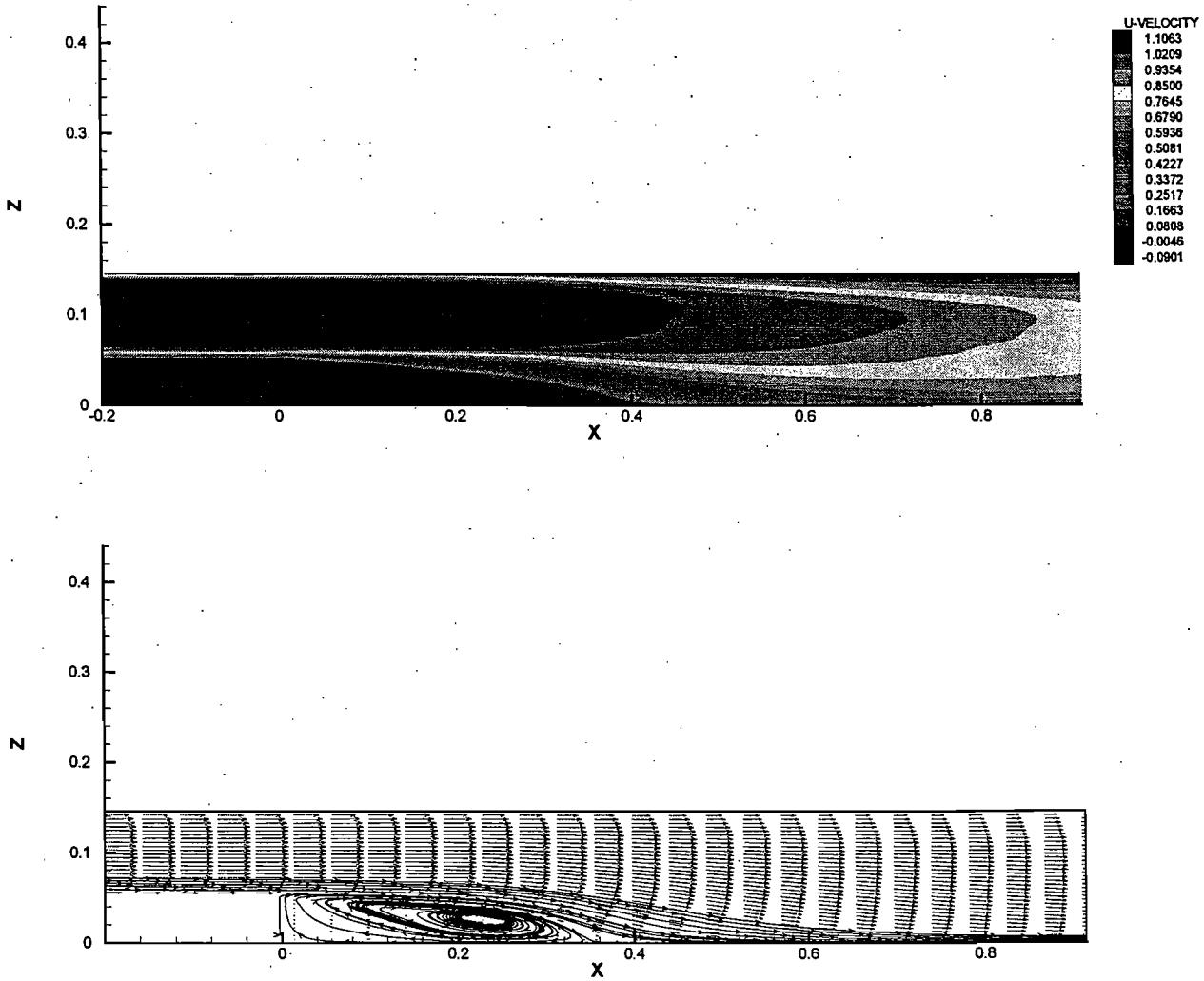

Figure 46: Average velocity contour, recirculation streamlines, and vector plots of the test section for the refined LES simulation where the inlet velocity is 1 m/s

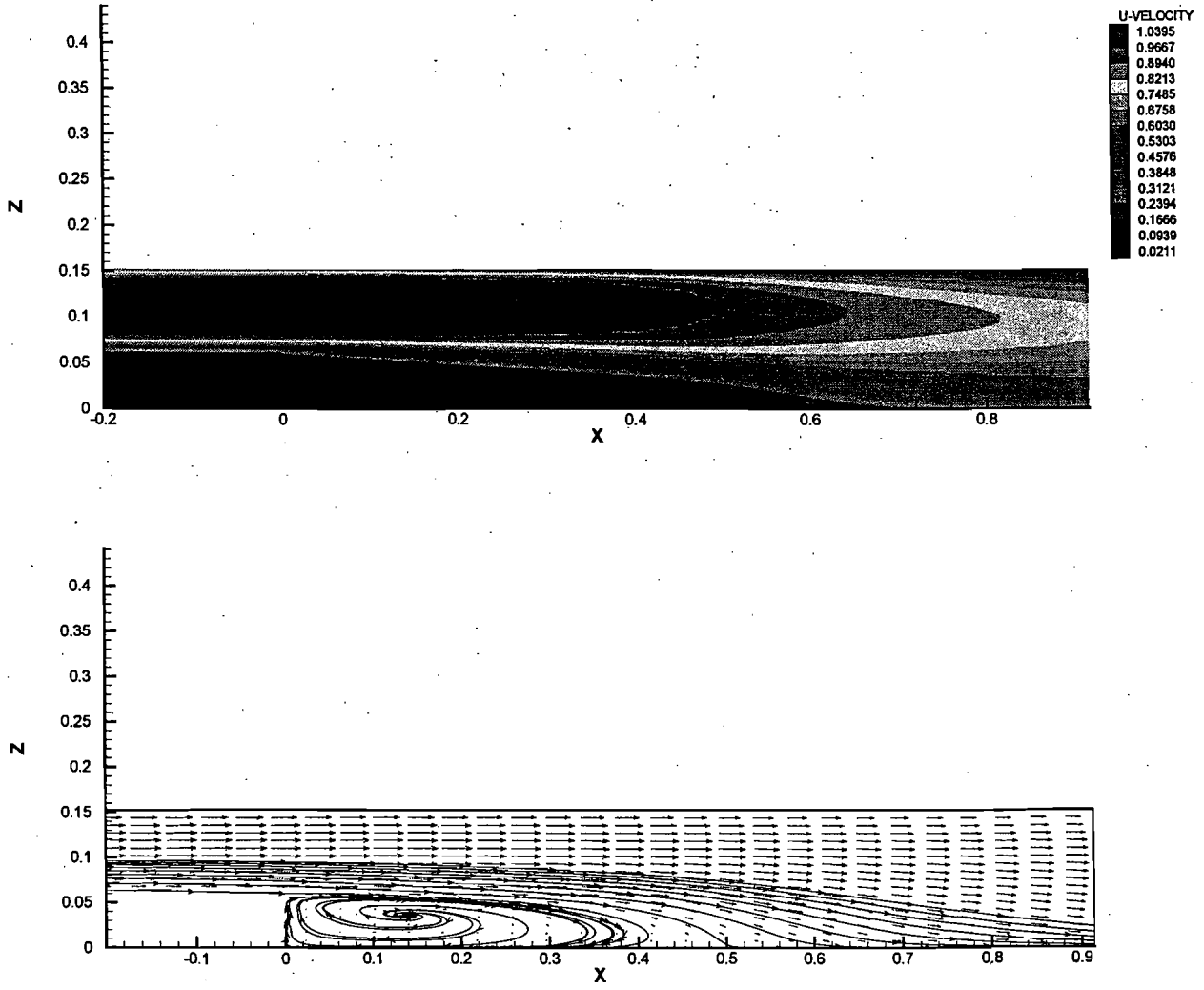

Figure 47: Average velocity contour, recirculation streamlines, and vector plot for the preliminary LES simulation where the inlet velocity is 0.89 m/s

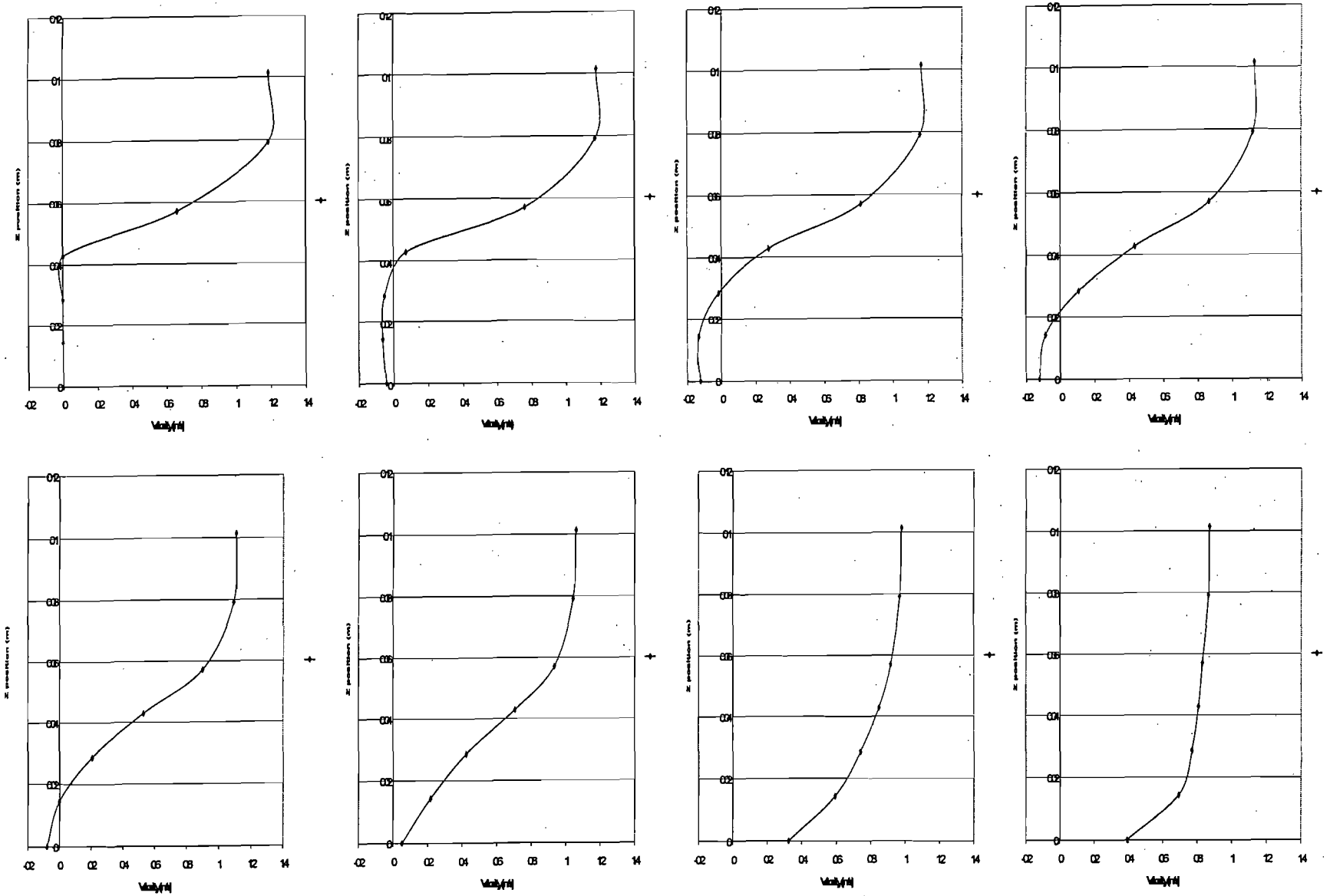

Figure 48: Velocity profiles for 1 m/s flow. Downstream locations featured a) x=0m, B) x=0.114m, C) x=0.191m, D) x=0.267m, E) x=0.305 m, F) x=0.381m, G) x=0.610m, H) x=0.830 m

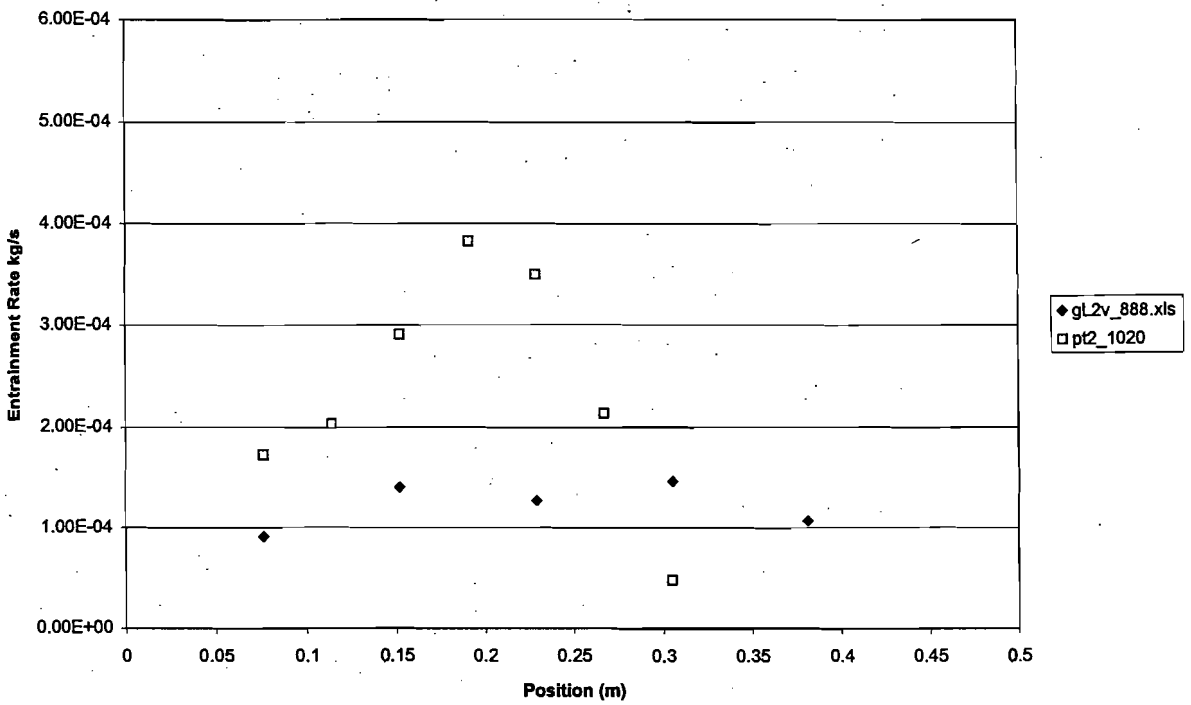

Figure 49: Rate of air entrainment vs. position downstream of the step for the preliminary and refined LES simulations

Guide to Legend: ♦ preliminary LES simulation of 0.89 m/s flow -- Grid spacing (234,9,18), □ refined LES simulation of 1 m/s flow -- Grid spacing (800,24,34)

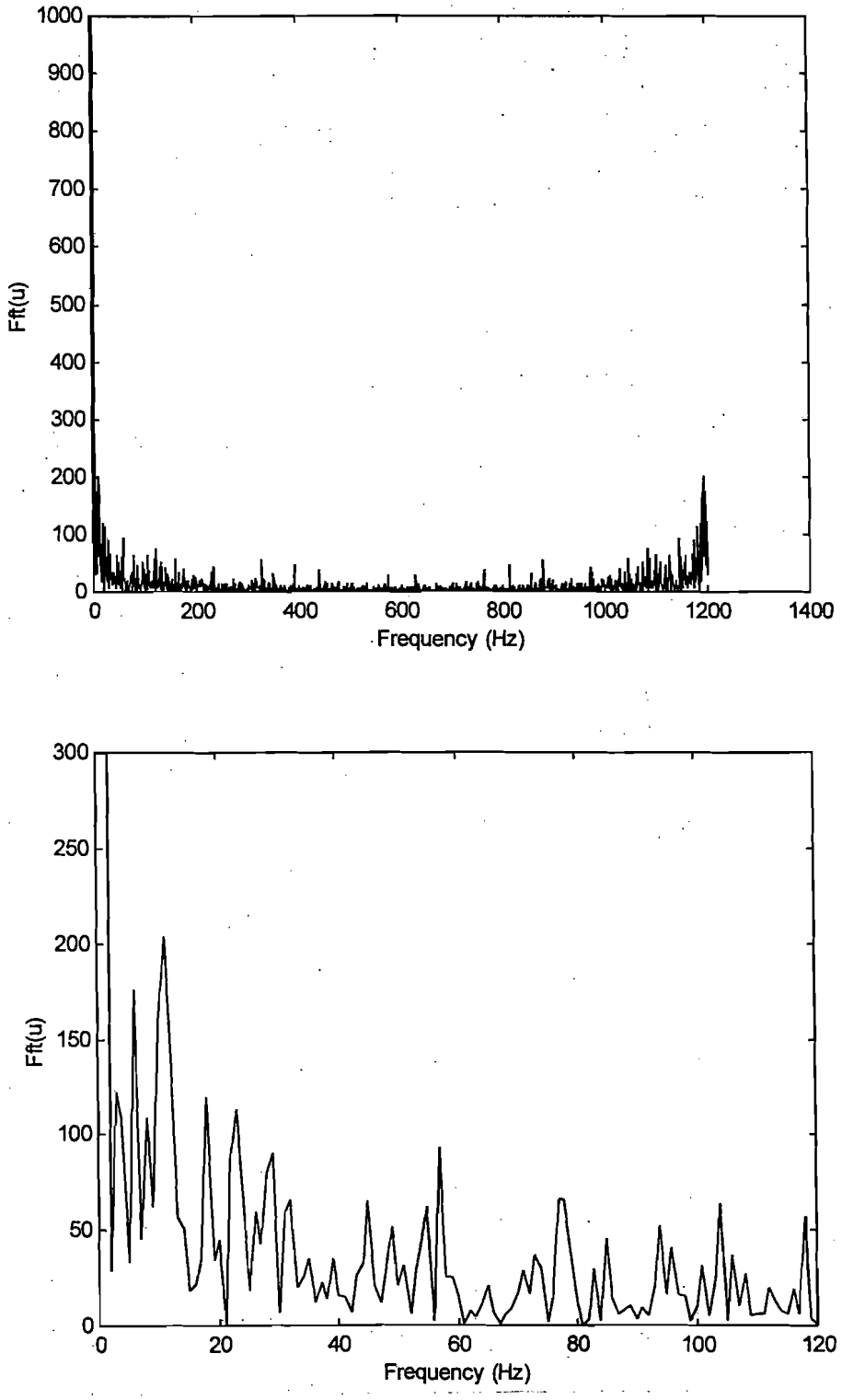

Figure 51: Fourier transform of the centerline test section exit velocity for the high resolution simulation.

REFERENCES

[1] United States Environmental Protection Agency Stratospheric Protection Division, (1997), "*Title VI of the Clean Air Act*", http://earth1.epa.gov/docs/ozone/title6/sec608.html. Visited 1999.

[2] Osaka Prefectural Government, "*Approaches to Global Environmental Problems: Measures of Protection for the Ozone Layer*", http://www.epcc.pref.osaka.jp/apec/eng/earth/ozone_layer_depletion/torikumi.htm. Visited 1999.

[3] Weber and Danberg, "Correlation of mean velocity measurements downstream of a swept backward-facing step," AIAA Journal, **30**, pp. 2701-2706, Nov 92.

[4] Honji,H, "The starting flow down a step," J. Fluid Mechanics, **69**, Part 2, pp 229-240, 1975.

[5] Bradshaw, P. and Wong, F.Y.F, " The reattachment and realization of a turbulent shear layer," J. Fluid Mech., **52**, Part 1, pp. 113-135, 1972.

[6] Shih, C. and Ho, C. -M., "Three-Dimensional Recirculation Flow in a Backward Facing Step," Transactions of the ASME, **116**, pp. 228-232, 1994.

[7] Browand, F.K., "An experimental investigation of the instability of an incompressible, separated shear layer," J. Fluid Mechanics, **26,** Part 2, pp.281-307, 1966.

[8] Rohmat, T. A., Yoshihasi, T., Obara, T., and Ohyagi, S, "An Experimental Study of Turbulent Diffusion Flames Established On a Porous Plate behind a Backward-Facing Step," Proceedings of the 5th ASME/JSME Joint Thermal Engineering Conference, San Diego, CA, 15-19 March 1999.

[9] Tsou, F. K., Chen, S. –J., and Aung, W., "Starting Flow and Heat Transfer Downstream of a Backward Facing Step," Journal of Heat Transfer, **113**, pp. 583-589, 1991.

[10] Westphal, R. V. and Johnston, J. P., "Effect of Initial Conditions on Turbulent Reattachment Downstream of a Backward-Facing Step," AIAA Journal, **22,** pp. 1727-1732,1984.

[11] Armaly, B. F., Durst, F., Pereira, J. C. F., and Schonung, B, "Experimental and theoretical investigation of backward-facing step flow," J. Fluid Mech., **127**, pp. 473-496, 1983.

[12] Ghoniem, A. F. and Sethian, J. A., "Effect of Reynold's Number on the Structure of Recirculating Flow," AIAA Journal, **25**, pp. 168-171, 1987.

[20] Thangam, S. and Hur, N., "A Highly Resolved Numerical Study of Turbulent Separated Flow Past a Backward-Facing Step," International Journal of Engineering Science, **29,** no. 5, pp. 607-615, 1991.

[21] Hallback, M., Henningson, D. S., Johansson, A. V., and Alfredsson, P. H., Eds., "Turbulence and Transition Modelling," Kluwer Academic Publishers, 1996.

[22] Le, H., Moin, P., and Kim, J., "Direct numerical simulation of turbulent flow over a backward-facing step," J. Fluid Mech., **330**, pp. 349-374, 1997.

[23] Neto, A. S., Grand, D., Olivier, M., and Lesieur, M., "A numerical investigation of the coherent vortices in turbulence behind a backward-facing step," J. Fluid Mech., **256**, pp. 1-25,1997.

[24] Ducros, F. , Comte P., and Lesieur, M, "Large Eddy Simulation of transition to turbulence in a boundary layer developing spatially over a flat plate," J. Fluid Mechanics, **326**, pp. 1-36, 1996.

[25] Fureby, C. and Moller, S.-I. "Large Eddy Simulation of Reacting Flows Applied to Bluff Body Stabilized Flames," AIAA Journal, **33**, pp. 2339-2347, 1996.

[26] Mornish, Y. and Kobayashi, T., "Large Eddy Simulation of Backward Facing Step Flow," Engineering Turbulence Modelling and Experiments, Elsevier,1990.

[27] Kobayashi, T. and Togashi, S., "Comparison of Turbulence Models Applied to Backward-Facing Step Flow," JSME International Journal, **39**, Series B, no. 3, pp. 453-460, 1996.

[28] Hamins, A., Presser, C., and Melton, L., "Suppression of a Baffle-Stabilized Spray Flame by Halogenated Agents," Twenty-Sixth Symposium (International) on Combustion, The Combustion Institute, pp. 1413-1420, 1996.

[29] Lemon, L. H., Tarpley, W. B., Jr., Freeman, M. K., and Tuno, A. L. "Persistent Fire Suppression for Aircraft Engines," Technical Report AFAPL-TR-79-2130, Energy and Minerals Research Co. , March 1980.

[30] Joulain, P and Torero, J. L.. "Gas Generator Induced Flow and its Effect on Fire Flame Extinction," **NIST-GCR-98-745**, National Institute of Standards and Technology, Building and Fire Research Laboratory, Gaithersburg, MD, February 1998.

[31] Yang, C. Y. and Grosshandler, W. L., Eds., "Solid Propellant Gas Generators: Proceedings of the 1995 Workshop," **NISTIR 5766,** National Institute of Standards and Technology, Gaithersburg, MD, 1995.

[32] Roberts, B. T., "Aerodynamic Evaluation of a Screening Method for Alternative Fire Suppression Agents," Master's Thesis, University of Maryland, 1999.

[33] Roberts, B. T., Du Bois, J. L., and Torero, J.L., "A Study of the Mechanisms Leading to Re-Ignition in a 'Worst Case' Fire Scenario," Yearly Report to the National Institute of Standards and Technology, University of Maryland, 1999.

[34] Mc Grattan, K., "Computational Fluid Dynamics and Fire Modeling," Course Notes, University of Maryland/National Institute of Standards and Technology, 1998.

[35] Mc Grattan, K., Baum, H.R., and Rehm, R. G., "Large Eddy Simulation of Fire Phenomenon," National Institute of Standards and Technology, Gaithersburg, MD, January 1999.

[36] Mc Grattan, K., Baum, H. R., Rehm, R. G., Hamins, A., Forney, G. P., and Mell, W., "Industrial Fire Simulation," National Institute of Standards and Technology, Gaithersburg, September 1999.

[37] Smagorinsky, J., "General Circulation Experiments with the Primitive Equations," Monthly Weather Review, **91**, no. 3, pp. 99-165, 1963.

[38] Mc Grattan, K, Letter from the author, 18 October 1999.

[39] Mc Grattan, K., "LES-3d" Computer software, ftp/nist.gov/pub/bfrl/mcgratta/Les3d/source, Visited January 1999. All further references to variables, subroutines, and subprograms refer to this computer software.

[40] Holman, J. P., "Heat Transfer," McGraw-Hill, Inc., 7th Edition, 1990.

[41] Munson, B. R., Young, D. F., and Okiishi, T. H., "Fundamentals of Fluid Mechanics," John Wiley & Sons, Inc., 2nd Edition, 1994.

[42] Fox, R. W. and McDonald, A. T., "Introduction to Fluid Mechanics," John Wiley & Sons, Inc., 1990.

[43] Mc Grattan, K, Letter from the author, 27 July 1999.